Dissertation

Buoyant-thermocapillary driven flow instabilities in cylindrical and annular liquid pools

ausgeführt zum Zwecke der Erlangung des akademischen Grades eines Doktors der technischen Wissenschaften unter Leitung von

Univ.Prof. Dipl.-Phys. Dr.rer.nat. H. C. Kuhlmann

Institutsnummer E322

Institut für Strömungsmechanik und Wärmeübertragung

eingereicht an der Technischen Universität Wien

Fakultät für Maschinenwesen und Betriebswissenschaften

von

Mag.rer.nat. Ulrich Schoisswohl

Matrikelnummer 9909539

A-1080 Wien, Bennogasse 30/2/3

Wien, im Oktober 2008

Kurzfassung

Der Fokus der vorliegenden Arbeit liegt auf dem Studium von durch Auftriebs- und Thermokapillarkräfte getriebenen Strömungen in zylindrischen Becken und Ringkanälen, sowie ihrer Abhängigkeit von thermischen und geometrischen Randbedingungen. Besonderes Interesse gilt dabei (i) der Instabilität des Strömungsmusters die von einem stationären axialsymmetrischen in einen dreidimensionalen Strömungszustand führt, sowie (ii) dem Verständnis der grundlegenden physikalischen Prozesse. Die dazu notwendige Berechnung der Hyperflächen kritischer Stabilität, sowie der zugehörigen Störströmung erfolgt mittels linearer Stabilitätsanalyse. Eine Energieanalyse und die damit verbundene Berechnung der Reynolds-Orr Gleichung und ihres thermischen Äquivalents ermöglicht ein tieferes Verständnis der Instabilitätsmechanismen.

Untersucht werden die folgenden beiden Konfigurationen:

- Ein mit einem Boussinesq-Fluid gefülltes zylindrisches Becken mit nicht deformierbarer freier Oberfläche, geheizt durch einen auf der freien Oberfläche aufgeprägten parabolischen Wärmestrom. Um die wichtigsten auftretenden Phänomene zu studieren, werden folgende Bereiche im Parameterraum numerisch berechnet:
  - Prandtlzahlen $10^{-10} \leq \mathrm{Pr} \leq 10$ bei Aspektverhältnis $\Gamma = 1$,
  - Aspektverhältnis $0.5 \leq \Gamma \leq 6.1$ bei Prandtlzahlen $\mathrm{Pr} = 10^{-10}$, 0.03 und 4,
  - Bondzahlen $0.01 \leq \mathrm{Bd} \leq 100$ bei Aspektverhältnis $\Gamma = 1$ und Prandtlzahlen $\mathrm{Pr} = 10^{-10}$ bzw. 10.

  Für die zugehörigen Kurven kritischer Stabilität wurden die physikalischen Instabilitätsmechanismen identifiziert, und spezifische repräsentative Spezialfälle im Detail studiert und diskutiert.

- Ein mit Silikonöl gefüllter Zylinder mit nicht deformierbarer freier Oberfläche geheizt mittels eines zylindrischen Heizdrahtes entlang der Zylinderachse (geometrisch entsprechend einem Ringkanal). Numerische Rechnungen für Prandtlzahl $\mathrm{Pr} = 27$ bei Erdbeschleunigung ($1g$) in den Parameterbereichen
  - Aspektverhältnisse $0.513 \leq \Gamma \leq 1.613$ bei Heizdraht-Aspektverhältnis $\eta = 0.079$,
  - Heizdraht-Aspektverhältnisse $0.0588 \leq \eta \leq 0.234$ bei Aspektverhältnis $\Gamma = 0.513$,

  werden mit früheren experimentellen und numerischen Ergebnissen verglichen. Für einen repräsentativen Fall gegeben durch die Parameter $\Gamma = 1$, $\eta = 0.1$ und $\mathrm{Pr} = 27$ wird der physikalische Instabilitätsmechanismus im Detail diskutiert.

Abstract

The present work studies the buoyant-thermocapillary driven flow in annular and cylindrical liquid pools and its dependence on thermal conditions and geometrical constraints. Of particular interest are (i) the transition from steady axisymmetric to three-dimensional flow and (ii) the underlying physical process driving this transition. The critical stability curves and perturbation flow states are computed numerically by means of a linear-stability analysis. In order to gain a deeper insight into the pattern formation and the respective physical mechanisms an energy analysis by means of the Reynolds-Orr equation and its thermal equivalent is conducted.
The following two setups investigated are

- A cylindrical pool filled with a Boussinesq fluid with a non-deformable free surface on top heated by a non-uniform parabolic heat flux at the free surface is investigated in the following parameter ranges
  - Prandtl numbers $10^{-10} \leq \mathrm{Pr} \leq 10$ at aspect ratio $\Gamma = 1$,
  - aspect ratios $0.5 \leq \Gamma \leq 6.1$ at Prandtl numbers $\mathrm{Pr} = 10^{-10}$, 0.03 and 4,
  - Bond numbers $0.01 \leq \mathrm{Bd} \leq 100$ at aspect ratio $\Gamma = 1$ and Prandtl numbers $\mathrm{Pr} = 10^{-10}$ respectively 10.

  For the above ranges the critical stability curves are computed and the underlying physical mechanisms identified. In order to give a complete picture of the physical instability mechanisms specific representative cases are selected, discussed and explained in detail.

- An pool filled with silicone oil with a non-deformable free surface on top heated by a submerged cylindrical heater along the axis (geometrically corresponding to an annular pool). The configuration is studied for Prandtl number $\mathrm{Pr} = 27$ and standard gravity conditions of $1g$ in the following ranges
  - aspect ratios $0.513 \leq \Gamma \leq 1.613$ at heater aspect ratio $\eta = 0.079$,
  - heater aspect ratios $0.0588 \leq \eta \leq 0.234$ at aspect ratio $\Gamma = 0.513$.

  The results are compared to prior experimental and numerical results, and the physical mechanism driving the instability is explained in detail for a representative micro-gravity case with parameters $\Gamma = 1$, $\eta = 0.1$ and $\mathrm{Pr} = 27$.

Wenn nicht mehr Zahlen und Figuren sind Schlüssel aller Kreaturen,
wenn die, so singen oder küssen, mehr als die Tiefgelehrten wissen,
wenn sich die Welt ins freie Leben und in die Welt wird zurückbegeben,
wenn dann sich wieder Licht und Schatten zu echter Klarheit werden gatten
und man in Märchen und Gedichten erkennt die wahren Weltgeschichten,
dann fliegt vor einem geheimen Wort das ganze verkehrte Wesen fort.

Novalis (aus Heinrich von Ofterdingen)

Minotaurus zu Ariadne: Ich erforsche das Labyrinth, ich suche die Wahrheit über dieses Wunder von Schönheit und Ordnung, von voraussagbarer Harmonie.

aus
Erwin Chargaff: Stimmen im Labyrinth.
Über die Natur und ihre Erforschung. Seite 111.
Klett-Cotta, 1. Auflage (2003).

Acknowledgements/Danksagungen

Herrn Univ.Prof. Dr. H. C. Kuhlmann gilt mein besonderer Dank für die Betreuung meiner Arbeit, die vielen Ideen und Anregungen, und für den tiefen Einblick in die Seele des wissenschaftlichen Betriebs.

Sehr herzlich bedanke ich mich bei O.Univ.Prof. Dr. A. Kluwick für die Übernahme des Koreferats, und das was ich in seinen Vorlesungen lernen durfte.

O.Univ.Prof. DDr. W. Schneider meinen aufrichtigen Dank für den vielen Kaffee, den ich als Gast in seiner Arbeitsgruppe geschlürft habe. Selbiger bildet für mich das Fundament akademischen Denkens.

Meinen besten Dank auch an Ao.Prof. Dr. H. Steinrück für die Beantwortung der vielen kleinen Fragen zwischendurch, und die vielen kleinen Gespräche über Gott und die Welt.

S. Albensoeder, F. Schimmel und S. Helma bin ich zu tiefem Dank verpflichtet, ihren hilfreichen Ratschlägen in der Anfangsphase der Dissertation ist vieles zu verdanken.

Herrn H. Neth meinen besten Dank dafür, dass er immer Zeit fand wenn etwas brannte, und Frau K. Cernohorsky für die vielen kleinen Erledigungen.

I'm very garteful to S. Shiratori, its always been a pleasure ... a pity though that no-one helped us find the crocodiles... and a piece of luck we weren't found by them...

Dear Ahmed Manzoor: many thanks for being such a good sport, you are a credit to your people.

Euch all meinen Kollegen meinen aufrichtigen Dank! Die vielen Gespräche, das gemeinsame Mittagessen und das angenehme Arbeitsklima haben mein Leben bereichert. Die Badminton-Spiele, Sauna- und Bier-Abend werden mir in lebendiger Erinnerung bleiben. Schade, dass nicht für mehr davon Zeit war.

Richard, wann besuchen wir Roland in Zürich?

Meiner Freundin Dani, meinen Freunden und Eltern, euch kann ich nicht genug danken, ihr habt mich durch so manches Tief der vergangenen Jahre getragen.

Marie-France Hirigoyen für ihre Klarheit, die sie gerne mit *jenen* teilt, die sie suchen.

Computing time provided by the Zentraler Informatik Dienst (ZID) of the Vienna University of Technology is gratefully acknowledged.

Contents

1 Introduction

Instability and patternformation in Marangoni flows have been in the focus of scientific inquiry and applied technological research for many years. They are of relevance in a whole range of scientific fields such as chemo-hydrodynamic pattern formation, the movement of chemical fronts, interfacial flows, thin liquid films, deformation and break of thin liquid films in microgravity, precursor films, and the transport of water and ions across the conjunctival membrane in the eye, to name but a few. Technological applications range from the formation of micro-droplets in the fields of chemistry, life science and bioscience to crystal growth and fusion welding.

Now what do we mean by a Marangoni flow? How can it be described and what types do we know? Since Marangoni flows are also known as surface tension driven flows we will start with the concept of surface tension. A good grasp on this concept will ease our understanding of the general concept of Marangoni flows.

1.1 Surface tension

Surface tension σ is an energy per unit area or force F per unit length L, which is due to the attractive intermolecular forces in a liquid, called cohesiveness. While the effect of these forces cancels for a molecule in the interior of the liquid, it creates a force towards the interior of the liquid for molecules at and in the immediate ambience of its interface to another liquid or gas. A liquid–liquid or liquid–gas interface has a specific shape which is defined by the minimum of interface energy. Surface tension as a material property of a liquid strongly depends on temperature and is very sensitive to minor changes in the chemical composition. For most liquid–gas interfaces surface tension decreases with temperature. A more detailed picture of surface tension as such is given in Tipler (1994) and Kuhlmann (1999).

1.2 Marangoni convection

Flows driven by variations in surface tension are called Marangoni flows. The process itself can be explained in terms of the local distribution of surface tension σ at the interface, which varies due to gradients in temperature (thermocapillary flows) or chemical composition (solutocapillary flows). The fluid is pulled along the gradients of surface tension from regions of low to regions of high surface tension, the flows driven by this effect are called *surface-tension-driven flows*.

Surface tension driven convection phenomena have most likely been known for a long time. Yet the first scientific account on surface tension driven flows was given by Thomson (1855) in his article *On certain curious Motions observable at the Surfaces of Wine and other Alcoholic Liquors* where he observed the movement of wine droplets at the glass–air interface in the interior of a wine glass. The effect itself has been named after the Italian physicist Carlo Marangoni (1840-1925) who studied the propagation of oil droplets at a water–air interface in a water basin with a diameter of ≈ 70m in Paris. In order to explain the fast propagation velocity of the oil droplets (> 2m/s) and the different regimes observable he was the first to claim that it is due to the weak surface tension of oil compared to water, Marangoni (1871). Similar experiments were performed by Lüdtge (1869) who noticed that capillary convection starts if two thin layers at different temperatures yet of the same fluid are brought into contact. A good historical review of the work done in the context of Marangoni flow is provided by Scriven & Sternling (1960). Note the clear distinction between to major types of flows: (i) thermocapillary and (ii) solutocapillary flows. The first type (i) being due to a non-uniform temperature distribution at the interface causing a non-uniform distribution of surface tension, this type of flow was found by Lüdtge (1869). Thomson (1855) and Marangoni (1871) observed the second type (ii) of flow where the non-unifom distribution of surface tension at the interface is due to gradients in the chemical concentration. - A thorough discussion of the thermocapillary effect is given by Kuhlmann (1999) and Nienhüser (2002).

1.3 Marangoni flows in the focus of scientific inquiry

Marangoni flows are of interest in various fields of scientific research. Of particular interest are those flows which are important to material processing in space. Hence, in literature we find a large body of experimental and numerical work on surface-tension-driven flows. Very well known among them is the floating zone problem, relevant for crystal-growth processes, which has been studied to great extent by Kuhlmann et al. and many other authors. In the context of the present work we are mostly interested in the investigations of the Marangoni flow in (i) weld pools during fusion welding and (ii) in annular liquid pools heated from the in- or the outside.

1.3.1 A brief review of previous work in fusion welding

In recent years fusion welding has become an accepted and widespread practice. Many industrial applications have been developed that make production faster and easier. A vast number of people have contributed to a better scientific understanding of the various physical processes one encounters in fusion welding. A good review article on the overall flow in weld pools has been written by DebRoy & David (1995). They consider a wide range of effects such as material composition, surface-active agents, vaporization, gas–metal reactions, heat transfer, etc.

An illustrative article on *Marangoni effects in welding* has been published by Mills *et al.* (1998). It is built around the Heiple–Roper theory which suggests that weld pool penetration is controlled by the flow in the weld pool which in turn is controlled by the direction and the magnitude of the thermocapillary forces at the liquid–gas interface. They consider electromagnetic/Lorentz, buoyancy and aerodynamic drag forces, material composition, etc.

Two and three dimensional numerical simulations for a cylindrical liquid pool with flat and curved surfaces at high Prandtl numbers have been performed by Sim & Zebib (2002). Their results show good agreement with experimental results published by Kamotani *et al.* (2000). Furthermore, they found that: *"... only azimuthal waves can generate oscillations in thermocapillary convection"*. Sim & Zebib (2004) developed a model to calculate the shape and position of the free surface during fusion welding. Their computations performed for intermediate Prandtl number ($\mathrm{Pr} = 0.292$) and low Reynolds numbers ($\mathrm{Re} = [65.6; 6560]$) revealed two distinct types of surface shapes which look similar to either (i) a bowl bump or a (ii) Sombrero.

Experimental and numerical studies on the influence of the beam diameter and the beam power on the flow field in a cylindrical pool filled with silicone oil have been performed by Kamotani & Ostrach (1994).

Limmaneevichitr & Kou (2000*a*) experimentally studied a pool of pure liquid $NaNO_3$ heated by a defocused CO_2 laser beam in order to simulate Marangoni convection. Their objective was a qualitative study of the dependence of the flow field on the heating mode. They found that an increase in beam power at constant beam diameter strengthens the Marangoni flow, yet reduces the penetration depth of the flow, if the beam diameter is decreased at constant beam power the Marangoni convection becomes stronger and the penetration depth of the flow increases.

In a succeeding paper Limmaneevichitr & Kou (2000*b*) experimentally confirmed the theoretical assumption that surface active agents can cause a flow reversal in a liquid $NaNO_3$ pool heated by a defocused CO_2 laser beam. Furthermore they found that the addition of C_2H_5COOK leads to a decrease in the strength of the outward flow, for a sufficiently high amount of C_2H_5COOK a flow reversal can be observed. They concluded that for pure $NaNO_3$ the pool tends to be shallow and the flow is directed outward. If sufficient C_2H_5COOK is added the flow reverses to an inward directed flow and the pool gets deeper.

Wagner *et al.* (1994) did three dimensional time-dependent numerical calculations of the full nonlinear Boussinesq approximation for a cylindrical volume of fluid at high Prandtl numbers in order to simulate Rayleigh and Marangoni convection. Their results on Rayleigh convection show good agreement with prior work by Neumann (1990), and the critical flow patterns and Marangoni numbers obtained for Marangoni convection compare favorably to earlier results from linearized stability. Their model for Marangoni convection is similar to the model considered in the present work.

Do-Quang (2004) investigated the time-dependent three-dimensional thermocapillary flow in fusion welding considering most physical mechanisms involved in tungsten arc welding, among them plasma effects and the movement of the workpiece. Their computations show a time-dependent chaotic melt flow influencing the width and depth of pool.

H. Du & X.Hu (2004) have devised a model for the welding process of a Titanium alloy which takes into account plasma effects, and keyhole absorption. It shows good agreement with experimental results.

In a very recent publication Abderrazak *et al.* (2008) experimentally and numerically investigate the thermal phenomena appearing during continuous laser keyhole welding. In particular they tried to shed some light on the formation of the pool and the keyhole as well as the dependence of the pool dimensions on the welding parameters.

1.3.2 A brief review of previous work on the annular pool

A setup that received quite some attention recently is the annular pool. An annular pool is an annular volume of fluid bounded by a solid bottom, solid lateral walls and an upper free surface. Two types of annular pools can be distinguished, those heated from the outside and cooled from the inside and those heated from the inside and cooled from the outside.

For the first type a series of unsteady three-dimensional numerical simulations for thermocapillary annular pools of moderate Prandtl number and variable depth was conducted by Li & Kwok (2003). Li *et al.* (2004*a*, 2005) extended the investigation to buoyant-thermocapillary flows in shallow annular pools. A two-dimensional study and a delineation of the critical stability curves under microgravity conditions has been performed by Li *et al.* (2004*b*). Shi & Imaishi (2006) performed two and three-dimensional simulations on high resolving grids for microgravity and earthbound gravity conditions in order to calculate the critical stability limit for the incipience of hydrothermal waves in terms of the critical Marangoni number, and performed an analysis of the motion of the individual fluid elements. The above work is summarized in a review article by Li *et al.* (2006). Very recently the influence of pool rotation on the transition of the flow pattern has been investigated by Li *et al.* (2008*b*).

The second type of annular pool heated from the inside and cooled from the outside will be considered in the present work. In the years from 1992 to 2000 Kamotani et al. published a series of papers on the onset of flow instabilities in cylindrical test sections with a free surface on top and filled with silicone oil. They used two different heating modes in order to introduce free surface deformations: a CO_2 laser beam and a cylindrical heater positioned along the axis of the test section. Their work can be split in three mayor parts: the test experiments performed under standard earthbound conditions published in Kamotani *et al.* (1992) and a theoretical analysis Kamotani *et al.* (1996), the results of the STDCE-1 aboard of USML-1 Spacelab in 1992, cf. Kamotani & Ostrach (1994), and finally their publications about the STDCE-2 aboard of USML-2 spacelab during its mission in October/November 1995, cf. Kamotani & Ostrach (1998); Kamotani *et al.* (1999, 2000). Though they have done some numerical work on the unperturbed axisymmetric flow field, almost all their work on the non-axisymmetric flow is experimental in nature. They have measured the critical temperature difference between the outer wall and the heater as a measure for the onset of the instability for various test sections and heaters under earthbound 1g conditions, compare Kamotani *et al.* (1992). In Kamotani & Ostrach (1994) they study the velocity fields of the STDCE-1 experimentally and numerically for CO_2 laser heating and heating by a cylindrical heater positioned at the axis of the test section. The corresponding temperature fields are published in Kamotani & Ostrach (1998). In Kamotani *et al.* (1999) they given an extensive study of the heating by a CO_2 laser beam and in Kamotani *et al.* (2000) they present the corresponding results for the experiments with a cylindrical heater.

In 2002 Sim & Zebib (2002) performed a numerical simulation in order to verify the space experiments of Kamotani et al., and in addition study the influence of free surface heat loss and Coriolis force on the transition process. Their results show a good agreement with the experiments of Kamotani et al.

1.4 Scope of the present work

The scope of the present work is to clarify the hydrodynamic instability and the underlying physical mechanisms in (i) weld pools during fusion welding and (ii) in the annular pool heated from the inside. To that end a physical model is presented in sec. 2. The numerical solutions strategy is provided in sec. 3 and the validation of its results is presented in sec. 4. The computed results are shown, interpreted and discussed in sec. 5. A discussion and some concluding remarks close the thesis in sec. 6.

1.4.1 Scope in the context of fusion welding

Sofar relatively little is known about the pattern formation in weld pools during the welding process and on its dependence on the heating mode, under conditions with and without gravity. A major reason being the difficulties in the experimental observation of the flow properties at high values of opacity and temperature.

In the present work we investigate the melt flow for zero-gravity conditions, relevant to space applications of this technology, and various gravity conditions, in order to make a step towards those terrestrial applications in which thermocapillary effects dominate buoyancy. To be more precise, we search for sufficient conditions for an axisymmetric basic steady flow to become unstable to a non-axisymmetric perturbation flow, and analyze the underlying physical mechanism driving the instability. First results for zero-gravity conditions have been published in Schoisswohl & Kuhlmann (2006), an extension of these results and a first discussion of the underlying physical mechanisms can be found in Schoisswohl & Kuhlmann (2007). In the present work we will discuss the most important results of prior publications and considerably extend them, for zero-gravity as well as gravity conditions, and a wide range of geometrical constraints.

Note that the model used for this purpose has previously been studied by Wagner *et al.* (1994) and others. Yet, no accurate prediction or systematic study of the stability boundaries of the basic axisymmetric state, and the physical mechanism driving the instability has been performed to date.

1.4.2 Scope in the context of the annular pool

Though some results of the experiments published by Kamotani et al. have been validated by Sim & Zebib (2002), up to date no systematic verification on the critical temperature difference for the onset of non-axisymmetric motion has been performed, nor have the physical mechanisms for the transition process been sufficiently understood. The present work closes this gap: (i) the critical temperature differences for the onset of linear instability in zero and standard gravity conditions are computed, (ii) a sound explanation of the physical mechanism driving the instability is given, (iii) some information on the influence of buoyancy on the onset of non-axisymmetric motion is presented, and (iv) finally the computed results are compared with previous experimental and numerical work.

2 Theoretical Approach

2.1 Mathematical Formulation

The aim of the present work is to study the linear stability in a liquid pool. To that end we consider a cylindrical volume of fluid with height d and radius R defining an aspect ratio $\Gamma = R/d$, compare fig.(2.1). The problem is formulated in cylindrical coordinates (r, z, φ). The volume of fluid is bounded by a non-deformable free surface on top and solid non-deformable walls at the sides and bottom. This non-deformability of the free surface is justified, because we study the configuration in the limit of asymtotically large mean surface tension σ_0[1].

2.1.1 Oberbeck–Boussinesq approximation

For the fluid we assume that its behaviour can be described by the Oberbeck-Boussinesq approximation for a Newtonian fluid, cf. Drazin & Reid (1981) or Landau & Lifschitz (1991), an approximation derived independently by Oberbeck (1879) and Boussinesq (1903).
The idea is to expand the material parameters appearing in the basic equations with respect to their values at an average temperature T_0. An estimate of the linear expansion coefficients and of the terms in which they appear shows that the material parameters can be approximated by their value at temperature T_0.

For this approximation the temperature variations $\Delta\mathsf{T}_0$ in the flow have to be small with respect to the average temperature T_0 ($\Delta\mathsf{T}_0 \ll \mathsf{T}_0$). Respectively variations in density $\Delta\rho$ will be very small ($\Delta\rho \ll \rho_0$) and can hence be neglected, except for the contribution of the buoyancy term to the overall flow. The conservation law of mass simplifies to

$$\nabla \cdot \mathbf{U} = 0 \quad . \tag{2.1}$$

Performing a Taylor expansion for density we get

$$\rho = \rho_0[1 - \beta(\mathsf{T} - \mathsf{T}_0)] \quad , \tag{2.2}$$

with

$$\beta = -\frac{1}{\rho_0}\left(\frac{\partial \rho}{\partial \mathsf{T}}\right)_{\mathsf{P};\mathsf{T}_0} \quad . \tag{2.3}$$

[1]For details on the mathematical derivation compare Shiratori (2007).

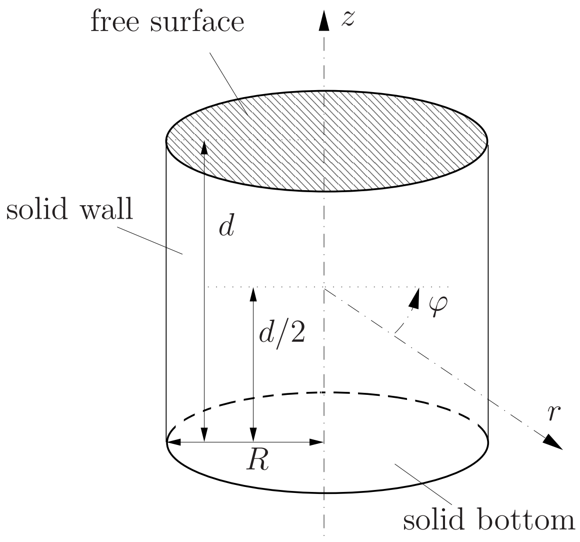

Figure 2.1: Geometry and coordinate system.

being the thermal expansion coefficient at constant pressure and average temperature. This yields a volume force density of buoyancy which can be calculated by

$$\boldsymbol{b} = -\rho g \boldsymbol{e}_z = -\rho_0[1 - \beta(\mathsf{T} - \mathsf{T}_0)]g\boldsymbol{e}_z \quad . \tag{2.4}$$

Here gravitational acceleration is given by $\boldsymbol{g} = -g\boldsymbol{e}_z$. (2.4) shows that buoyancy forces due to thermal expension are of order $O(\Delta\mathsf{T})$. With buoyancy being of the same order of magnitude as the inertial and the dissipative forces they have to be taken into account in the momentum equation. Note that the constant part $-\rho_0 g\boldsymbol{e}_z$ in (2.4) can be included in the hydrostatic pressure.

In the temperature equation the contributions of compression temperature and heat production by dissipation drop out.

The Oberbeck-Boussinesq approximation can be summarized as follows:

- Variations in density are neglected except for their contribution to buoyancy.
- The flow is divergence free ($\nabla \cdot \mathbf{U} = 0$).
- In the temperature equation we consider only the convective and the diffusive term.

A more rigorous derivation of the Oberbeck-Boussinesq approximation can be found in Mihaljan (1962).

The above approximations lead to the following system of equations:

$$\frac{\partial \mathbf{U}}{\partial t} + (\mathbf{U} \cdot \nabla)\mathbf{U} = -\frac{1}{\rho_0}\nabla\mathsf{P} + \nu\nabla^2\mathbf{U} - g\beta\mathsf{T}\boldsymbol{e}_z \tag{2.5a}$$

$$\frac{\partial \mathsf{T}}{\partial t} + (\mathbf{U} \cdot \nabla)\mathsf{T} = \kappa\nabla^2\mathsf{T} \tag{2.5b}$$

$$\nabla \cdot \mathbf{U} = 0 \quad . \tag{2.5c}$$

(2.5a) is the equation for the conservation of momentum, (2.5b) is the temperature equation and (2.5c) the equation for the conservation of mass. $\mathbf{U}^T = (\mathsf{U}, \mathsf{V}, \mathsf{W})$, P, T and ρ are the variables for the velocity field, pressure, temperature and density. κ, μ and g are the thermal diffusivity, the dynamic viscosity and the acceleration due to gravity.

Note that the vorticity if needed is calculated by

$$\boldsymbol{\Omega} = \nabla \times \mathbf{U} \quad . \tag{2.6}$$

2.1.2 Boundary Conditions

In order to close the system (2.5a)-(2.5c) we have to introduce boundary conditions for velocity $\mathbf{U}$ and temperature T.

Velocity Boundary Conditions

At the solid walls we impose no-slip velocity boundary conditions, i.e. the tangential and the normal flow velocities must vanish at these boundaries

$$\mathbf{U} = 0 \quad . \tag{2.7}$$

With the free surface being an interface between the two immiscible fluids (1) (liquid) and (2) (gas) the effective stresses can be balanced by

$$\mathbf{S}^{(1)} \cdot \boldsymbol{n} = \mathbf{S}^{(2)} \cdot \boldsymbol{n} \quad . \tag{2.8}$$

Here $\mathbf{S}$ is the stress tensor at the interface given by the pressure and viscous forces per unit surface. $\mathbf{S}$ is defined as

$$\mathbf{S} = -\mathsf{P}\boldsymbol{I} + \mu \left[\nabla\mathbf{U} + (\nabla\mathbf{U})^T\right] \quad . \tag{2.9}$$

According to Kuhlmann (1999) the stress balance for a flat interface can be expressed by

$$\mathbf{S}^{(1)} \cdot \boldsymbol{n} - (I - \boldsymbol{n}\boldsymbol{n}) \cdot \nabla\sigma = \mathbf{S}^{(2)} \cdot \boldsymbol{n} \quad . \tag{2.10}$$

Expanding surface tension σ at average temperature T_0

$$\sigma(\mathsf{T}) = \sigma(\mathsf{T}_0) - \gamma(\mathsf{T} - \mathsf{T}_0) + \frac{1}{2}\frac{\partial^2\sigma}{\partial \mathsf{T}^2}(\mathsf{T} - \mathsf{T}_0)^2 + O\left((\mathsf{T} - \mathsf{T}_0)^3\right) \quad , \tag{2.11}$$

and truncating the expansion at the linear term, the gradient of surface tension can be approximated by

$$\nabla\sigma \cong -\gamma\nabla\mathsf{T} \quad . \tag{2.12}$$

Neglecting higher order terms equation (2.10) can be cast into

$$\mathbf{S}^{(1)} \cdot \boldsymbol{n} + \gamma(I - \boldsymbol{n}\boldsymbol{n})\nabla\mathsf{T} = \mathbf{S}^{(2)} \cdot \boldsymbol{n} \quad . \tag{2.13}$$

Assuming that due to the low dynamic viscosity of gases the gas phase (2) exerts no significant shear stress on the interface equation (2.13) can be rewritten as

$$\mu \left[\nabla\mathbf{U} + (\nabla\mathbf{U})^T\right] \cdot \boldsymbol{n} + \gamma(I - \boldsymbol{n}\boldsymbol{n})\nabla\mathsf{T} = 0 \quad . \tag{2.14}$$

This is the velocity boundary condition at the free surface, compare Kuhlmann (1999) for a more rigorous derivation.

Thermal Boundary Conditions

At the solid walls we assume constant temperature

$$\mathsf{T} = \mathsf{T}_m = \mathsf{T}_0 \quad . \tag{2.15}$$

With T_m being the melt temperature of the liquid (1).

Considering Newtons law of cooling, radiation transport and an external heatflux the thermal boundary condition at the free surface takes the form

$$-k\boldsymbol{e}_z \cdot \nabla \mathsf{T} = \underbrace{-Q(r)}_{\text{laser heating}} + \underbrace{h(\mathsf{T} - \mathsf{T}_a)}_{\text{Newtons law of cooling}} + \underbrace{\epsilon s_0(\mathsf{T}^4 - \mathsf{T}_a^4)}_{\text{radiation transport}} \quad . \tag{2.16}$$

Here $Q = Q(r)$ is an axisymmetric heat flux due to laser heating, which is according to Kamotani *et al.* (1999) absorbed within a thin layer of fluid below the free surface. k is the thermal conductivity of the liquid, h the heat-transfer coefficient, ϵ the emissivity, s_0 the Stefan-Boltzmann constant and T_a the temperature of the ambient medium the free surface is in contact with. Assuming that the heat transfer can be modeled to a sufficient degree of accuracy by neglecting all terms but the heat flux $Q = Q(r)$ we end up with

$$-k\boldsymbol{e}_z \cdot \nabla \mathsf{T} = -Q(r) \quad . \tag{2.17}$$

The heat flux due to laser heating is modeled by an axisymmetric parabolic profile $Q = Q(r)$ imposed at the free surface

$$Q(r) = Q_{max}\left(1 - \frac{r}{R}\right)^2 \quad . \tag{2.18}$$

With Q_{max} being the maximum heat flux $Q_{max} = Q(r = 0)$ temperature is scaled by $\Delta\mathsf{T} = Q_{max}d/k$.

2.1.3 Oberbeck-Boussinesq approximation in dimensionless Form

In order to reduce the number of parameters we cast the Oberbeck-Boussinesq approximation into a dimensionless form. To that end we introduce the typical scales: d, ν/d, d^2/ν, $\Delta\mathsf{T}$ and $\rho\nu^2/d^2$ for length, velocity, time, temperature and pressure. We start with the governing equations given by (2.5a)-(2.5c) and introduce the typical scales. We get

$$\frac{\rho\nu^2}{d^3}\frac{\partial \boldsymbol{U}}{\partial t} + \frac{\rho\nu^2}{d^3}(\boldsymbol{U}\cdot\nabla)\boldsymbol{U} = -\frac{\rho\nu^2}{d^3}\nabla P + \frac{\rho\nu^2}{d^3}\nabla^2\boldsymbol{U} - g\Delta\mathsf{T}\beta\rho\Theta\boldsymbol{e}_z \tag{2.19a}$$

$$\frac{\nu\Delta\mathsf{T}}{d^2}\frac{\partial\Theta}{\partial t} + \frac{\nu\Delta\mathsf{T}}{d^2}(\boldsymbol{U}\cdot\nabla)\Theta = \frac{\kappa\Delta\mathsf{T}}{d^2}\nabla^2\Theta \tag{2.19b}$$

$$\frac{\nu}{d^2}\nabla\cdot\boldsymbol{U} = 0 \quad , \tag{2.19c}$$

with the dimensionless variables $\boldsymbol{U} = (U, V, W)^{\mathrm{T}} = (\mathbf{U}d)/\nu$ for the vector of the radial, azimuthal and axial velocity components, $P = (\mathsf{P}d^2)/(\rho\nu^2)$ for pressure, and $\Theta = (\mathsf{T} - \mathsf{T}_0)/\Delta\mathsf{T}$ denoting the temperature field.

Dividing the momentum equations (2.19a) by $\rho\nu^2/d^3$, the temperature equation (2.19b) by $\nu\Delta\mathsf{T}/d^2$ and the continuity equation (2.19c) by ν/d^2 yields

$$\frac{\partial \boldsymbol{U}}{\partial t} + (\boldsymbol{U}\cdot\nabla)\boldsymbol{U} = -\nabla P + \nabla^2\boldsymbol{U} - \frac{\beta\Delta\mathsf{T} g d^3}{\nu^2}\Theta\boldsymbol{e}_z \tag{2.20a}$$

$$\frac{\partial\Theta}{\partial t} + (\boldsymbol{U}\cdot\nabla)\Theta = \frac{\kappa}{\nu}\nabla^2\Theta \tag{2.20b}$$

$$\nabla\cdot\boldsymbol{U} = 0 \quad . \tag{2.20c}$$

Introducing the Prandtl and the Grashof number given by

$$\mathrm{Pr} = \frac{\nu}{\kappa} \quad \text{and} \quad \mathrm{Gr} = \frac{\beta\Delta\mathsf{T} g d^3}{\nu^2} \quad , \tag{2.21}$$

and substituting them into (2.20a)-(2.20c) the final system of equations takes the form

$$\frac{\partial \boldsymbol{U}}{\partial t} + (\boldsymbol{U}\cdot\nabla)\boldsymbol{U} = -\nabla P + \nabla^2\boldsymbol{U} - \mathrm{Gr}\Theta\boldsymbol{e}_z \tag{2.22a}$$

$$\frac{\partial\Theta}{\partial t} + (\boldsymbol{U}\cdot\nabla)\Theta = \frac{1}{\mathrm{Pr}}\nabla^2\Theta \tag{2.22b}$$

$$\nabla\cdot\boldsymbol{U} = 0 \quad . \tag{2.22c}$$

Velocity Boundary Conditions in dimensionless Form

Introducing the scalings used to get equations (2.22a)-(2.22c) the velocity boundary condition at the solid walls (no-slip) (2.7) takes the dimensionless form

$$\boldsymbol{U} = 0 \quad , \tag{2.23}$$

and the boundary condition at the free surface becomes

$$\left[\nabla\boldsymbol{U} + (\nabla\boldsymbol{U})^T\right]\cdot\boldsymbol{n} + \mathrm{Re}(I - \boldsymbol{n}\boldsymbol{n})\nabla\Theta = 0 \quad . \tag{2.24}$$

Here we have introduced the new dimensionless parameter Re the thermocapillary Reynolds number

$$\mathrm{Re} = \frac{\gamma\Delta\mathsf{T}}{\rho\nu}\frac{d}{\nu} \quad . \tag{2.25}$$

Note that the term $(\gamma\Delta\mathsf{T})/(\rho\nu) = U_{th}$ has the dimension of a velocity. With this definition of the Reynolds number we can define the dynamic Bond number

$$\mathrm{Bd} = \frac{\mathrm{Gr}}{\mathrm{Re}} \quad . \tag{2.26}$$

A dimensionless number that measures the relative importance of buoyancy with respect to thermocapillary forces.

Thermal Boundary Conditions in dimensionless Form

Using the scales d, $\Delta\mathsf{T}$ and $Q_{max} = k\Delta\mathsf{T}/d$ for length, temperature and heatflux the dimensionless form of the thermal boundary conditions at the solid walls becomes

$$\Theta = 0 \quad . \tag{2.27}$$

At the free surface equation (2.17) yields

$$\frac{\partial\Theta}{\partial z} = -\left(1 - \frac{r}{\Gamma}\right)^2 \quad . \tag{2.28}$$

Note that the direction of the heat flux has been considered.

2.1.4 Remarks on the definition of the Reynolds number

Above the thermocapillary Reynolds number Re has been defined as

$$\mathrm{Re} = \frac{\gamma\Delta\mathsf{T}d}{\rho\nu^2} \quad . \tag{2.29}$$

In the floating zone problem, which uses the same definition for the thermocapillary Reynolds number (cp. Kuhlmann (1999)), $\Delta\mathsf{T}$ is given by the temperature difference of the hot (h) and the cold (c) corner ($\Delta\mathsf{T} = \mathsf{T}_h - \mathsf{T}_c$). In the present problem formulation the temperature difference at the free surface between the solid wall and the center of the pool is not know apriori, rather it is part of the result. Therefore $\Delta\mathsf{T}$ in (2.29) is formulated as a function of the maximum heat flux Q_{max} to

$$\Delta\mathsf{T} = Q_{max}d/k \quad . \tag{2.30}$$

The thermocapillary Reynolds number can hence be written as

$$\mathrm{Re} = \frac{\gamma Q_{max}d^2}{\rho\nu^2 k} \quad . \tag{2.31}$$

This difference in definition is important because it clarifies that the $\Delta\mathsf{T}$ used in the present nondimensionalization is not equal to the temperature difference $\Delta\mathsf{T} = \mathsf{T}_{ce} - \mathsf{T}_0$. Here T_{ce} is the temperature at the center of the pool and T_0 the temperature of the solid walls of the pool, which can only be computed aposteriori.

2.2 Solution Strategy

Reviewing the velocity boundary condition at the free surface (2.24)

$$\left[\nabla\boldsymbol{U} + (\nabla\boldsymbol{U})^T\right]\cdot\boldsymbol{n} + \mathrm{Re}(I - \boldsymbol{nn})\nabla\Theta = 0 \quad , \tag{2.32}$$

it becomes obvious that the thermocapillary Reynolds number describes the coupling of the local shear stresses and the local temperature gradient at the free surface. Rewriting (2.32) in cylindrical coordinates for the present problem we get

$$\frac{\partial U}{\partial z} + \mathrm{Re}\frac{\partial \Theta}{\partial r} = 0 \quad \leftrightarrow \quad \text{radial shear stress} \tag{2.33a}$$

$$\frac{\partial V}{\partial z} + \frac{\mathrm{Re}}{r}\frac{\partial \Theta}{\partial \varphi} = 0 \quad \leftrightarrow \quad \text{azimuthal shear stress} \tag{2.33b}$$

$$W = 0 \quad \leftrightarrow \quad \text{no penetration} \quad . \tag{2.33c}$$

From equation (2.31) we find

$$\mathrm{Re} = \mathrm{Re}(Q_{max}, \rho, \nu, d, k, \gamma) \quad . \tag{2.34}$$

For a given setup we assume the parameters ρ, ν, d, k and γ constant, hence

$$\mathrm{Re} \propto Q_{max} \quad . \tag{2.35}$$

If the magnitude of heat flux stays below the limit value Q^c_{max} the flow in the pool is steady axisymmetric. By increasing Q_{max} above this threshold the flow becomes unstable non-axisymmetric either steady or unsteady.

In the remainder of the present work it is exactly this threshold we are looking for, and since the peak heat flux is directly proportional to the thermocapillary Reynolds number, we will express this threshold in terms of the critical Reynolds number Re_c.

In order to find the critical Reynolds number we perform a linear stability analysis. A method successfully employed in prior work by Albensoeder (2004); Kuhlmann (1999); Wanschura (1996) for the lid-driven cavity problem and the half-zone problem of thermocapillary flow respectively.

To perform a linear stability analysis the variables of state

$$\boldsymbol{X}^T = (\boldsymbol{U}, P, \Theta) \quad , \tag{2.36}$$

are decomposed into a basic axisymmetric state $\boldsymbol{x}_0$ and a perturbation $\boldsymbol{x}$

$$\underbrace{\begin{pmatrix} \boldsymbol{U} \\ P \\ \Theta \end{pmatrix}}_{\boldsymbol{X}} = \underbrace{\begin{pmatrix} \boldsymbol{u}_0 \\ p_0 \\ \theta_0 \end{pmatrix}}_{\boldsymbol{x}_0} + \underbrace{\begin{pmatrix} \boldsymbol{u} \\ p \\ \theta \end{pmatrix}}_{\boldsymbol{x}} \quad . \tag{2.37}$$

Inserting this decomposition and linearizing the governing equations (2.22a)-(2.22c) for small perturbations $\boldsymbol{x} \ll \boldsymbol{x}_0$ we get

$$\frac{\partial \boldsymbol{u}}{\partial t} + (\boldsymbol{u}\cdot\nabla)\boldsymbol{u}_0 + (\boldsymbol{u}_0\cdot\nabla)\boldsymbol{u} = -\nabla p + \nabla^2\boldsymbol{u} - \mathrm{Gr}\theta\boldsymbol{e}_z \tag{2.38a}$$

$$\frac{\partial \theta}{\partial t} + (\boldsymbol{u}\cdot\nabla)\theta_0 + (\boldsymbol{u}_0\cdot\nabla)\theta = \frac{1}{\mathrm{Pr}}\nabla^2\theta \tag{2.38b}$$

$$\nabla\cdot\boldsymbol{u} = 0 \quad . \tag{2.38c}$$

For the perturbation $\boldsymbol{x}$ in the linearized equations an Ansatz of normal modes is chosen

$$\boldsymbol{x} = \hat{\boldsymbol{x}} e^{\mathrm{i}m\varphi + \lambda t} + c.c. \quad . \tag{2.39}$$

Using this Ansatz equations (2.38a)-(2.38c) and the corresponding boundary conditions can be written as a generalized eigenvalue problem

$$(\boldsymbol{A} - \lambda \boldsymbol{B}) \cdot \hat{\boldsymbol{x}} = 0 \quad , \tag{2.40}$$

compare also Albensoeder (2004) for a detailed account. Here $\hat{\boldsymbol{x}}$ is the amplitude vector, m the azimuthal wave number and $\lambda = \sigma + i\omega$. $\Re(\lambda) = \sigma$ corresponds to the growth rate and $\Im(\lambda) = \omega$ to the angular frequency of an eigenmode of the system (2.40). Since this Ansatz is periodic in azimuthal direction φ it takes into account the φ-homogenity of the system. Due to the cylindrical geometry of the weldpool only discrete wave numbers m can be realised ($m \in \mathbf{N}$).

Note that the system (2.40) has an infinite number of degrees of freedom. In order to find a solution they have to be reduced to a finite number ($k = 1, ..., K$) by means of an appropriate discretization.

In accordance with the Ansatz of normal modes (2.39) a normal mode can either grow ($\sigma_k > 0$), decay ($\sigma_k < 0$) or hypothetically remain as it is ($\sigma_k = 0$), in the later case it is called *neutrally stable*. Assuming that all eigenmodes of (2.40) decay the flow in the pool will be steady and axisymmetric. On the other hand is a single growing mode sufficient for the flow to become non-axisymmetric over time, compare equation (2.39) for $t \to \infty$. Hence in order for a flow to be linearly stable all eigenmodes need growth rates ($\sigma_k \leq 0$). In practice we are looking for an eigenmode satisfying the condition

$$\max_k \Re(\lambda_k) = 0 \quad . \tag{2.41}$$

With the eigenvalues λ_k depending on the parameters Re, Gr, Pr, Γ and m

$$\lambda_k = \lambda_k(\mathrm{Re}, \mathrm{Pr}, \mathrm{Gr}, \Gamma, m) \quad . \tag{2.42}$$

If condition (2.41) can not be satisfied by any of the eigenmodes of (2.40) its parameters need to be changed until an eigenmode with $\sigma_k = 0$ is found. An eigenvalue λ_k satisfying condition (2.41) is called a *neutral* eigenvalue λ_n. The curve resulting from the variation of one out of the parameters $\Xi_j = \{\mathrm{Re},\ \mathrm{Gr},\ \mathrm{Pr},\ \Gamma\}$ while assuring $\sigma_k = 0$ and $m = const.$ is called a *neutral curve*. The *critical curve* is computed as the minimum envelope of all neutral curves with respect to wave number m.

Investigating for example the dependence of Re on Pr for constant $\{\mathrm{Gr}, \Gamma\}$ and a series of wave numbers $m = 1, ..., M$, we can find a *neutral* Reynolds number $\mathrm{Re} = \mathrm{Re}_n$ satisfying $\Re(\lambda_k) = \sigma_k = \sigma_n = 0$ for any value of $\{m,\ \mathrm{Pr}\}$. Keeping $m = const.$ and computing Re_n as a function of Pr we get one out of M neutral curves. The minimum envelope of the M neutral curves is equivalent to the critical curve and the corresponding Reynolds numbers are called the *critical Reynolds numbers* Re_c.

2.3 Energy Analysis

In the preceeding section we have shown how to compute the curves of critical stability by means of a linear stability analysis. The analysis yields (a) the critical Reynolds number Re_c, (b) the critical eigenvalue $\lambda_c = \sigma_c + \omega_c$ with $\sigma_c = 0$ and the critical frequency ω_c, and (c) the corresponding perturbation mode $\boldsymbol{x}_c$.

In order to perform an energy analysis we need to start from the Reynolds-Orr equation and its thermal equivalent, their derivation is presented in appendix B. Both equations describe the kinetic respectively thermal energy transport of energy from the basic state to perturbation mode and vice versa. The principle idea is to locate the regions of influence of the specific physical effects and to quantify their relative contribution to the energy transport.

The Reynolds–Orr equation is given by

$$\begin{aligned} \frac{d}{dt}E_{\text{kin}} \quad &+ \underbrace{\langle u^2\partial_r u_0\rangle}_{I_{v1}} + \underbrace{\langle uw\partial_z u_0\rangle}_{I_{v2}} + \underbrace{\left\langle \frac{v^2 u_0}{r} \right\rangle}_{I_{v3}} + \underbrace{\langle uw\partial_r w_0\rangle}_{I_{v4}} + \underbrace{\langle w^2\partial_z w_0\rangle}_{I_{v5}} \\ &- \underbrace{\int_S dS(u\partial_z u)}_{M_r} - \underbrace{\int_S dS(v\partial_z v)}_{M_\varphi} + \underbrace{\langle(\nabla\times\boldsymbol{u})^2\rangle}_{D} - \underbrace{\langle Gr\theta w\rangle}_{I_{Gr}} = 0 \quad . \end{aligned} \tag{2.43}$$

Here $\langle ...\rangle$ is equivalent to $\int ... dV$, the integration by volume. E_{kin} is the total kinetic energy in the integration volume, D is the rate of viscous dissipation, I_{v1} to I_{v5} describe the advection of basic state momentum $\boldsymbol{u}_0$ by the perturbation mode $\boldsymbol{u}$, thus adding to the perturbation flow itself. The quantities M_r and M_φ represent the work done by the Marangoni forces on the free surface in radial and azimuthal direction. Work by buoyancy forces is given by I_{Gr}.
For further analysis we will also need the local rates of change of energy . These are the integrands of the above integrals and will be indicated, henceforth, by lower-case letters, e.g. $m_r = u\partial_z u$ or $i_{v1} = u^2\partial_r u_0$.

The thermal equivalent of the Reynolds–Orr equation is given by

$$\frac{d}{dt}E_{\text{th}} + \underbrace{\langle Tu\partial_r\theta_0\rangle}_{I_{T1}} + \underbrace{\langle\theta w\partial_z\theta_0\rangle}_{I_{T2}} - \underbrace{\frac{1}{Pr}\int_S dS\frac{1}{2}\partial_z(\theta^2)}_{H} + \underbrace{\frac{1}{Pr}\langle(\nabla\theta)^2\rangle}_{D_T} = 0 \quad . \tag{2.44}$$

Here E_{th} is the total thermal energy in the integration volume, D_T is the rate of heat diffusion, I_{T1} and I_{T2} represent the thermal energy produced by the advection of basic state temperature θ_0 by the perturbation flow $\boldsymbol{u}$ thus adding to the perturbation temperature field θ. Finally H is a measure of the supply of thermal energy E_{th} through the free surface. The local rates of change of thermal energy are the integrands of the above integrals. They will again be denoted by lower-case letters, e.g. $i_{T1} = \theta u\partial_r\theta_0$.

A detailed discussion of the individual terms is presented in appendix B.

Note however that the representation in polar coordinates must not necessarily be a good one. Alternatively the local energy transfer terms can also be reformulated for perturbation velocities tangential and normal to the local coordinates of the streamlines, i.e. the perturbation velocity $\boldsymbol{u}$ is split into a tangential

$$\boldsymbol{u}_t = \frac{(\boldsymbol{u} \cdot \boldsymbol{u}_0)\boldsymbol{u}_0}{\boldsymbol{u}_0^2} \tag{2.45}$$

and a normal part

$$\boldsymbol{u}_n = \boldsymbol{u} - \boldsymbol{u}_t \quad . \tag{2.46}$$

Instead of the five production terms I_{v1}-I_{v5} in relation (2.43) we then get only four terms I'_{v1}-I'_{v4}. They are

$$I'_{v1} = \langle \boldsymbol{u}_n \cdot (\boldsymbol{u}_n \cdot \nabla u_0) \rangle \tag{2.47a}$$
$$I'_{v2} = \langle \boldsymbol{u}_t \cdot (\boldsymbol{u}_n \cdot \nabla u_0) \rangle \tag{2.47b}$$
$$I'_{v3} = \langle \boldsymbol{u}_n \cdot (\boldsymbol{u}_t \cdot \nabla u_0) \rangle \tag{2.47c}$$
$$I'_{v4} = \langle \boldsymbol{u}_t \cdot (\boldsymbol{u}_t \cdot \nabla u_0) \rangle \quad . \tag{2.47d}$$

For a detailed account compare Albensoeder (2004) and Nienhüser & Kuhlmann (2002).

3 Numerical Implementation

In this section all methods and information necessary to implement the linear stability analysis of the 2D steady flow are presented.

In the first part all points related to the discretization procedure are addressed, including (a) the discretization in finite volumes, (b) the staggered and (c) the stretched grid, and (d) the interpolation of numerical data at inter-grid points.

The second part is concerned with all issues related to the linear stability analysis and its implementation. To that end (a) the computation of the basic state and (b) the perturbation flow, (c) the tracing of the neutral Reynolds number, and (d) the concept of critical stability will be explained.

3.1 Discretization

The system of partial differential equations given by the governing equations (2.22a)-(2.22a) can be written as

$$\boldsymbol{f}(\boldsymbol{x}) = 0 \quad . \tag{3.1}$$

In order to numerically solve the above system it needs to be transformed into a system of difference equations

$$\boldsymbol{A} \cdot \boldsymbol{x} = \boldsymbol{b} \quad . \tag{3.2}$$

In the present work a finite volume method implemented on a staggered locally stretchable grid is used.

The plane of computation is equivalent with the (r, z) plane. Using the symmetry of the system all computations can be performed on a two-dimensional computational domain composed of $N_r \times N_z$ cells. In order to implement the boundary conditions an additional row respectively column of *visual* or *ghost* cells is needed on either side of the computational domain. The indices i, j, k are used to mark the positions of the variables. Here i marks the position in radial (r) and j in axial (z) direction. For the purpose of data visualization we will need the index k, which is a discrete measure for the azimuthal (φ) direction. The indices running in radial (r), axial (z) and azimuthal (φ) direction are:

$$\begin{aligned}
r: &\quad i = 0, \cdots, N_r + 1 \quad , \\
z: &\quad j = 0, \cdots, N_z + 1 \quad , \\
\varphi: &\quad k = 0, \cdots, N_\varphi + 1 \quad .
\end{aligned} \tag{3.3}$$

Here N_r, N_z, and N_φ are the number of finite volume cells in radial, axial, and azimuthal direction. A coordinate point is given by (r_i, z_j, φ_k).

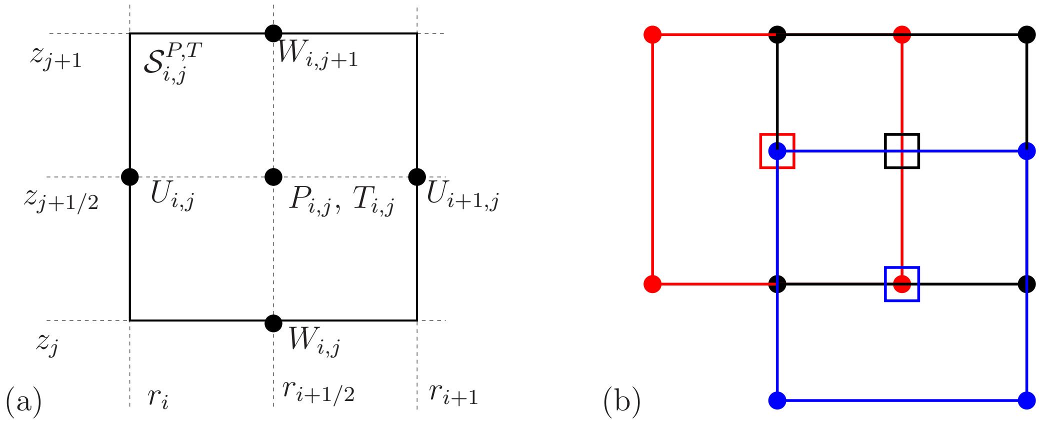

Figure 3.1: (a) A two-dimensional cell of a staggered grid belonging to the grid point (i, j). (b) The three different control volumes used in a staggered grid: the colors stand for the U-control-volume (red) the W-control-volume (blue) and the V-P-T-control-volume (black). The corners of the control volumes are marked by colored dots and the centers by squares.

3.1.1 Uniform Staggered Grid

On colocated numerical grids all variables are located directly at the center of the cell $\mathcal{S}_{i,j}$. A grid cell is defined as a geometrical domain $\mathcal{S}_{i,j} = [r_i, r_{i+1}] \times [z_j, z_{j+1}]$.

On a staggered grid the grid points for the velocity components are located on the surfaces of the finite volumes and the gridpoints for pressure and temperature are located at the center of the volumes, cp. figure 3.1a. The physical quantities pressure $P_{i,j}$, temperature $T_{i,j}$ and in case of a three-dimensional computational domain the azimuthal velocity $V_{i,j}$ are located at positions $(r_{i+1/2}, z_{j+1/2})$ where they form the center for the corresponding pressure/temperature/azimuthal velocity control volumes $\mathcal{S}^{P,T}_{i,j}$ or $\mathcal{S}^{V}_{i,j}$. The other velocity components $U_{i,j}$ and $W_{i,j}$ are located at positions $(r_i, z_{j+1/2})$ for the radial and $(r_{i+1/2}, z_j)$ for the axial velocity, where they again form the centers of the corresponding radial and axial velocity control volumes $\mathcal{S}^{U}_{i,j}$ respectively $\mathcal{S}^{W}_{i,j}$. Compare fig. 3.1b for the positions of the the different control volumes.

The respective control volumes of the variables belonging to the grid point (i, j) are

$$\mathcal{S}^{U}_{i,j} = [r_{i-1/2}, r_{i+1/2}] \times [z_j, z_{j+1}] \tag{3.4a}$$
$$\mathcal{S}^{V}_{i,j} = [r_i, r_{i+1}] \times [z_j, z_{j+1}] \tag{3.4b}$$
$$\mathcal{S}^{W}_{i,j} = [r_i, r_{i+1}] \times [z_{j-1/2}, z_{j+1/2}] \tag{3.4c}$$
$$\mathcal{S}^{P}_{i,j} = [r_i, r_{i+1}] \times [z_j, z_{j+1}] \tag{3.4d}$$
$$\mathcal{S}^{T}_{i,j} = [r_i, r_{i+1}] \times [z_j, z_{j+1}] \quad . \tag{3.4e}$$

Note that the different control volumes and the locations of the physical variables have to be considered in the discretization process of the governing equations (2.22a)-(2.22a).

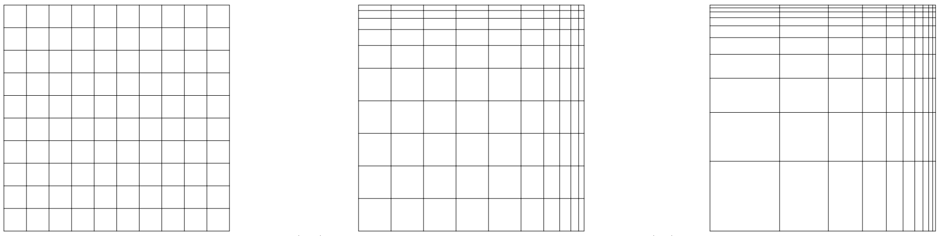

(a) (b) (c)

Figure 3.2: Each of the three computational grids displayed above feature $N_r \cdot N_z = 10 \times 10$ grid cells. (a) shows a uniform grid ($N_{\delta_r}^W = N_{\delta_r}^E = N_{\delta_z}^S = N_{\delta_z}^N = 0$). (b) and (c) show non-uniform grids, with cells compressed towards the upper and the right boundary. The stretching-factors are $\delta_r = \delta_z = 0.7$, and the number of compressed cells is given by (b) $N_{\delta_r}^E = N_{\delta_z}^N = 5$ respectively (c) $N_{\delta_r}^E = N_{\delta_z}^N = 10$.

3.1.2 Non-Uniform Staggered Grid

From theoretical considerations we expect strong variations in the solution structure normal and close to the bounding interfaces, in particular the formation of viscous and thermal boundary layers. Resolving these strong gradients is not an easy task, since it can only be achieved by a massiv increase of the overall number of grid cells. Such an approach is possible, yet is very expensive in terms of CPU-time and other computational resources. An alternative is to provide high grid resolution locally by refining the computational grid only in regions where grid refinement is necessary. Since we expect the formation of boundary layers close to the free surface and the liquid–solid interface of the pool it seems but logical to refine the computational grid here.

In the present approach the grid is stretched (compressed) along the coordinate directions, hence two neighboring grid cells will have slightly different dimensions. Their size ratios respectively stretching factors are given by

$$\delta_r = \frac{\Delta r_{i+1}}{\Delta r_i} \quad \text{and} \quad \delta_z = \frac{\Delta z_{j+1}}{\Delta z_j} \quad . \tag{3.5}$$

The stretching factors should not change the dimensions of two neighboring cells by more than 5% otherwise a loss of spatial accuracy of the second order scheme can be expected.

3.1.3 Definition of the implemented Grid

The coordinates of the grid points of the computational mesh can be expressed by

$$r_i = \begin{cases} -\Delta r_1 & \text{for} \quad i = 0 \\ 0 & \text{for} \quad i = 1 \\ r_{i-1} + \Delta r_{i-1} & \text{for} \quad i = 2, ..., N_r + 1 \\ r_{N_r+1} + \Delta r_{N_r} & \text{for} \quad i = N_r + 2 \end{cases}$$

$$r_{i+1/2} = \begin{cases} \frac{1}{2}(r_{i+1} + r_i) & \text{for} \quad i = 0, ..., N_r + 1 \\ 2r_{N_r+3/2} - r_{N_r+1/2} & \text{for} \quad i = N_r + 2 \end{cases} ,$$

in radial direction, and in axial direction by

$$z_j = \begin{cases} -\Delta z_1 & \text{for} \quad j = 0 \\ 0 & \text{for} \quad j = 1 \\ z_{j-1} + \Delta z_{j-1} & \text{for} \quad j = 2, ..., N_z + 1 \\ z_{N_z+1} + \Delta z_{N_z} & \text{for} \quad j = N_z + 2 \end{cases}$$

$$z_{j+1/2} = \begin{cases} \frac{1}{2}(z_{j+1} + z_j) & \text{for} \quad j = 0, ..., N_z + 1 \\ 2z_{N_z+3/2} - z_{N_z+1/2} & \text{for} \quad j = N_z + 2 \end{cases} .$$

Where

$$\Delta r_i = \begin{cases} dr\delta_r^{N_{\delta r}^W - i} & \text{for} \quad i = 1, ..., N_{\delta r}^W \\ dr & \text{for} \quad i = N_{\delta r}^W + 1, ..., N_r - N_{\delta r}^E \\ dr\delta_r^{i+N_{\delta r}^E - N_r} & \text{for} \quad i = N_r - N_{\delta r}^E + 1, ..., N_r \end{cases}$$

with

$$dr = \frac{\Gamma}{N_r - (N_{\delta r}^W + N_{\delta r}^E) + \sum_{i=1}^{i=N_{\delta r}^W + N_{\delta r}^E} \delta_r^i} , \tag{3.6}$$

is the distance between two neighboring radial grid points r_i and r_{i+1}. In axial direction the distance between the two grid points z_j and z_{j+1} is computed by

$$\Delta z_j = \begin{cases} dz\delta_z^{N_{\delta z}^S - j} & \text{for} \quad j = 1, ..., N_{\delta z}^S \\ dz & \text{for} \quad j = N_{\delta z}^S + 1, ..., N_z - N_{\delta z}^N \\ dz\delta_z^{j+N_{\delta z}^N - N_z} & \text{for} \quad j = N_z - N_{\delta z}^N + 1, ..., N_z \end{cases}$$

with

$$dz = \frac{1}{N_z - (N_{\delta z}^S + N_{\delta z}^N) + \sum_{j=1}^{j=N_{\delta z}^S + N_{\delta z}^N} \delta_z^j} . \tag{3.7}$$

$N_{\delta r}^W$, $N_{\delta r}^E$, $N_{\delta z}^S$, and $N_{\delta r}^N$ give the number of cells compressed towards the left (W), right (E), lower (S) and upper (N) boundary of the computational domain. As an illustration some examples are shown in figure 3.2.

Note that with this approach the solution can be computed either on a uniform or on a non-uniform staggered grid. For computations on a non-uniform staggered grid we can decide along which coordinate direction, to what extent, and on which side we want to stretch the computational cells.

3.1.4 Interpolation of Numerical Data

In course of the discretization process the value of a variable is frequently needed at positions other then its original location. The necessary interpolation is performed by means of *Linear Interpolation* (CDS)[1]. Compare Ferziger & Perić (2002) for details.

A variable X which is originally located at position (j, i) is interpolated to positions $(i+1/2, j)$ and $(i, j+1/2)$ by

$$\bar{X}_{i+1/2,j} = \xi X_{i+1,j} + (1-\xi) X_{i,j} \tag{3.8a}$$

$$\bar{X}_{i,j+1/2} = \eta X_{i,j+1} + (1-\eta) X_{i,j} \quad . \tag{3.8b}$$

Here $\bar{X}$ is the value of the variable at its new position, while X denotes its value at its original position. ξ and η are interpolation coefficients given by

$$\xi_U = \frac{r_{i+1/2} - r_i}{r_{i+1} - r_i} \qquad \eta_U = \frac{z_{j+1} - z_{j+1/2}}{z_{j+3/2} - z_{j+1/2}} \tag{3.9a}$$

$$\xi_W = \frac{r_{i+1} - r_{i+1/2}}{r_{i+3/2} - r_{i+1/2}} \qquad \eta_W = \frac{z_{j+1/2} - z_j}{z_{j+1} - z_j} \tag{3.9b}$$

$$\xi_P = \xi_T = \frac{r_{i+1} - r_{i+1/2}}{r_{i+3/2} - r_{i+1/2}} \qquad \eta_P = \eta_T = \frac{z_{j+1} - z_{j+1/2}}{z_{j+3/2} - z_{j+1/2}} \tag{3.9c}$$

Note that since the interpolation is performed on a staggered grid the interpolation coefficients differ with the variable. The indices in the above definition of the interpolation coefficients show for which variable(s) the coefficients apply.

3.1.5 Finite Volume Method

The discretization of the governing equations (2.22a)-(2.22a) is performed by means of a finite volume method (FVM)[2]. It was chosen for three major reasons: (a) it is widely used and well tested in fluid dynamics, (b) according to R. J. LeVeque & Müller (1998) its advisable to use finite volumes rather than finite differences for conservation laws, and (c) it is easy to implement on non-uniform grids.

In order to implement the FVM the computational domain is decomposed into small finite volumes. For an one-dimensional domain these finite volumes are intervals $\mathcal{C}_i$, for a two-dimensional domain surfaces $\mathcal{S}_{ij}$ and for a three-dimensional domain they are volumes $\mathcal{V}_{ijk}$. After the decomposition the governing equations are evaluated in their integral form for the corresponding finite volumes.

As an example the FVM is implemented for the continuity equation (2.5c)

$$\nabla \cdot \boldsymbol{U} = 0 \quad , \tag{3.10}$$

[1] According to Ferziger & Perić (2002) this is the simplest second-order interpolation scheme. The acronym CDS is used because it corresponds to the central-difference approximation of the first derivative in Finite Differences (FD).

[2] Compare Ferziger & Perić (2002); R. J. LeVeque & Müller (1998) or Versteeg & Malalasekera (1995) for a detailed account on the Finite Volume Method.

on a two-dimensional computational domain.

The discretization procedure consists of the following steps:

1. Integration of the two-dimensional form of the continuity equation

$$\frac{\partial(rU)}{\partial r} + r\frac{\partial(W)}{\partial z} = 0 \tag{3.11}$$

for the finite surface $\mathcal{S}_{ji} = [r_j, r_{j+1}] \times [z_i, z_{i+1}]$, since the computational domain is two-dimensional the finite *volume* is a surface. The integral takes the form

$$\int_{z_i}^{z_i+1} dz \int_{r_j}^{r_j+1} dr \left(\frac{\partial(rU)}{\partial r} + r\frac{\partial(W)}{\partial z} \right) = 0 \quad . \tag{3.12}$$

2. Integration with respect to r respectively z yields

$$\int_{z_i}^{z_i+1} dz\ [rU]_{\Delta r} + \int_{r_j}^{r_j+1} dr\ r[W]_{\Delta z} = 0 \quad . \tag{3.13}$$

Here [...] indicates a difference as a jump in the value of an expression and the subscripts Δr and Δz indicate the coordinate direction of this jump.

3. Approximating the integral by the midpoint-rule approximation[3], we get

$$\Delta z_i\ [rU]_{\Delta r} + \Delta r_j\ r[W]_{\Delta z} = 0 \quad . \tag{3.14}$$

4. Evaluation of the differences by means of a first order difference scheme gives

$$\Delta z_i\ [r_{j+1}U_{j+1,i} - r_j U_{j,i}] + \Delta r_j\ r_{j+1/2}[W_{j,i+1} - W_{j,i}] = 0 \quad . \tag{3.15}$$

This is the finite volume formulation of the continuity equation on a staggered grid. The formulations of the remaining governing equations and boundary conditions can be constructed in a similar way. Note that due to the use of a staggered grid (cp. sec. 3.1.1) every variable has its own finite (control) volume.

3.2 Linear Stability Analysis

The linear stability analysis can be split into four major steps (cp. fig. 3.3)

1. A first guess of the thermocapillary Reynolds number $\mathrm{Re} = \mathrm{Re}^{\mathrm{start}}$ for which we expect neutral stability.

2. Computation of the steady axisymmetric basic flow $\boldsymbol{x}_0$ by means of a Newton-Raphson-Iteration, cp. sec. 3.2.1.

[3]Compare Ferziger & Perić (2002) p.74 for the midpoint rule.

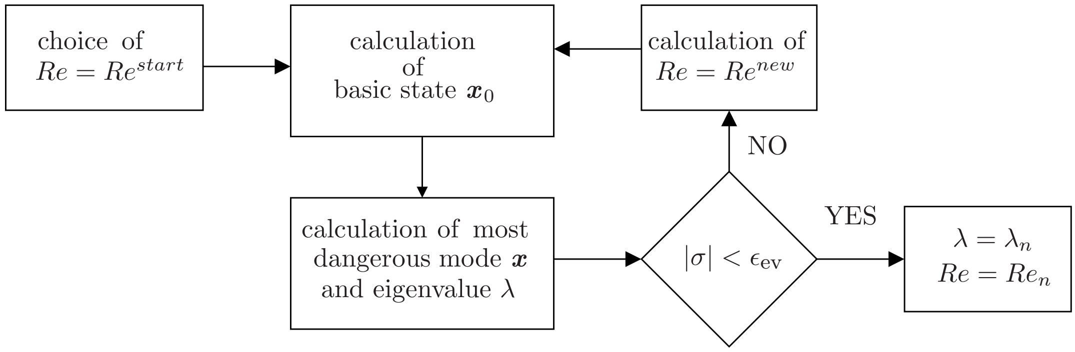

Figure 3.3: Flow chart of the linear stability analysis.

3. Computation of the strongest growing non-axisymmetric perturbation mode $\boldsymbol{x}$ with growth rate $\sigma = \sigma_{max} = \max_i \sigma_i$. The computation for the corresponding eigenvalue $\lambda = \sigma + \mathrm{i}\omega$ is performed by means of an Inverse Iteration, cp. sec. 3.2.2.

4. Evaluation of the termination criterion $|\sigma| = |\Re(\lambda)| < \epsilon_{\text{ev}}$, cp. sec. 3.2.3.

   a) For $|\sigma| < \epsilon_{\text{ev}}$ we have found the point of neutral stability up to the prescribed accuracy ϵ_{ev}. In that case $\lambda = \lambda_n$ is the *neutral* eigenvalue, $\text{Re} = \text{Re}_n$ the neutral Reynolds number, $\boldsymbol{x} = \boldsymbol{x}_n$ the neutral perturbation mode, and $\boldsymbol{x}_0$ the corresponding basic flow state.

   b) For $|\sigma| > \epsilon_{\text{ev}}$ we calculate a new Reynolds number $\text{Re} = \text{Re}^{\text{new}}$ by means of a secant method, and resume the computation at step 2.

In what follows a detailed account of the separate steps is given.

3.2.1 Computation of the Basic State Flow

For a steady and axisymmetric basic state flow

$$\partial_t = \partial_\varphi = v_0 \equiv 0 \tag{3.16}$$

the governing equations (2.22a)-(2.22c) in cylindrical coordinates are

$$u_0 \frac{\partial u_0}{\partial r} + w_0 \frac{\partial u_0}{\partial z} = -\frac{\partial p_0}{\partial r} + \frac{1}{r}\frac{\partial}{\partial r}\left(r \frac{\partial u_0}{\partial r}\right) + \frac{\partial^2 u_0}{\partial z^2} \tag{3.17a}$$

$$u_0 \frac{\partial w_0}{\partial r} + w_0 \frac{\partial w_0}{\partial z} = -\frac{\partial p_0}{\partial z} + \frac{1}{r}\frac{\partial}{\partial r}\left(r \frac{\partial w_0}{\partial r}\right) + \frac{\partial^2 w_0}{\partial z^2} \tag{3.17b}$$

$$u_0 \frac{\partial \theta_0}{\partial r} + w_0 \frac{\partial \theta_0}{\partial z} = \frac{1}{\text{Pr}}\left[\frac{1}{r}\frac{\partial}{\partial r}\left(r \frac{\partial \theta_0}{\partial r}\right) + \frac{\partial^2 \theta}{\partial z^2}\right] \tag{3.17c}$$

$$\frac{1}{r}\frac{\partial (r u_0)}{\partial r} + \frac{\partial w_0}{\partial z} = 0 \quad . \tag{3.17d}$$

In order to implement the finite volume method and the staggered grid the equations (3.17a)-(3.17b) have to be written in their integral form. Integration over the 2-dimensional *volume* $\int d\mathcal{S} = \int r dr dz$ yields

$$\int [ru_0^2]_{\Delta r} dz + \int [w_0 u_0]_{\Delta z} r\, dr = \int [2u_0 + r\partial_r u_0]_{\Delta r} dz + \\ + \int [\partial_z u_0]_{\Delta z}\, r dr + 2\int [w_0]_{\Delta z} dr - \int [rp_0]_{\Delta r} dz + \int p_0 dr dz \tag{3.18a}$$

$$\int [ru_0 w_0]_{\Delta r} dz + \int [w_0^2]_{\Delta z} r\, dr = \int [r\partial_r w_0]_{\Delta r} dz + \\ + \int [\partial_z w_0]_{\Delta z}\, r dr - \int [p_0]_{\Delta z}\, r dr + \mathrm{Gr} \int \theta_0 r dr dz \tag{3.18b}$$

$$\int [ru_0 \theta_0]_{\Delta r} dz + \int [w_0 \theta_0]_{\Delta z} r\, dr = \\ = \frac{1}{\mathrm{Pr}} \left(\int [r\partial_r \theta_0]_{\Delta r} dz + \int [\partial_z \theta_0]_{\Delta z}\, r dr \right) \tag{3.18c}$$

$$0 = \int [u_0 r]_{\Delta r} dz + \int r [w_0]_{\Delta z} dr \quad . \tag{3.18d}$$

The above integrals are approximated by the midpoint-rule and the variables evaluated by means of a first order difference scheme, compare sec. 3.1.5 where the procedure is explained in detail for the continuity equation.

The resulting system of four algebraic difference equations for every grid point (i, j) can be written as

$$\boldsymbol{A}(\boldsymbol{x}) \cdot \boldsymbol{x} = \boldsymbol{b} \quad , \tag{3.19}$$

with $\boldsymbol{x}^T = (u_{0,0}, w_{0,0}, p_{0,0}, \theta_{0,0}, u_{0,1}, v_{0,1}, \cdots \theta_{N_r+1,N_z+1})$. (3.19) is solved by means of the Newton-Raphson-Iteration-Method (cp. J. H. Mathews (2004)). The iteration process is considered converged as soon as the 2-norm $\|...\|_2$ of the *residual*

$$\boldsymbol{r} = \boldsymbol{A}(\boldsymbol{x}) \cdot \boldsymbol{x} - \boldsymbol{b} \quad , \tag{3.20}$$

satisfies

$$\|\boldsymbol{r}\|_2 < \epsilon \quad , \tag{3.21}$$

where ϵ is of the order of $O(10^{-7})$. - As a result of the Newton-Raphson-Iteration-Method we get the basic flow $\boldsymbol{x}_0$. For more details on the iteration procedure check the gray box below.

Newton-Raphson-Method

The Newton-Raphson-Iteration-Method is composed of the following steps:

1. Calculation of the residual

$$\boldsymbol{r}^{(k)} = \boldsymbol{A}(\boldsymbol{x}^{(k)}) \cdot \boldsymbol{x}^{(k)} - \boldsymbol{b} \quad . \tag{3.22}$$

   For the first iteration step ($k = 0$) the vector $\boldsymbol{x}^{(k)} = \boldsymbol{x}^{(0)}$ is chosen at random.

2. Computation of the Jacobi for $\boldsymbol{x}^{(k)}$

$$J^{(k)}_{j,i} = \left. \frac{\partial r_j}{\partial x_i} \right|_{\boldsymbol{x}=\boldsymbol{x}^{(k)}} \quad . \tag{3.23}$$

3. The linear system

$$\boldsymbol{J}^{(k)} \cdot \delta\boldsymbol{x}^{(k)} = -\boldsymbol{r}^{(k)} \quad , \tag{3.24}$$

   is solved by means of a LAPACK[a] routine.

4. Calculation of the new vector $\boldsymbol{x}^{(k+1)}$,

$$\boldsymbol{x}^{(k+1)} = \boldsymbol{x}^{(k)} + \delta\boldsymbol{x}^{(k)} \, . \tag{3.25}$$

5. Calculation of the new residual $\boldsymbol{r}^{(k+1)}$,

$$\boldsymbol{r}^{(k+1)} = \boldsymbol{A}(\boldsymbol{x}^{(k+1)}) \cdot \boldsymbol{x}^{(k+1)} - \boldsymbol{b} \, . \tag{3.26}$$

   a) If the norm of the residual is sufficiently small or the maximum number of iterations K_{max} exceeded, i.e.

$$\|\boldsymbol{r}^{(k+1)}\|_2 < \epsilon \qquad \text{or} \qquad k > K_{max} \, , \tag{3.27}$$

   the iteration is terminated, and $\boldsymbol{x}^{(k+1)}$ is the approximation of the solution vector.

   b) Otherwise the iteration process is resumed at step 2.

[a]LAPACK, the Linear Algebra PACKage, is an open-source software library for numerical computing written in Fortran 77. Available at http://www.netlib.org/lapack/.

3.2.2 Discretization of the Perturbation Flow

The perturbation mode $\boldsymbol{x}$ and the corresponding eigenvalue λ are computed along the lines of the solution strategy discussed in section 2.2. To that end the perturbation equations 2.38a-2.38c are written for cylindrical coordinates

$$\begin{aligned}
\frac{\partial u}{\partial t} =& -\left(u_0\frac{\partial}{\partial r}+\frac{v_0}{r}\frac{\partial}{\partial \varphi}+w_0\frac{\partial}{\partial z}\right)u-\left(u\frac{\partial}{\partial r}+\frac{v}{r}\frac{\partial}{\partial \varphi}w\frac{\partial}{\partial z}\right)u_0\\
&-\frac{\partial p}{\partial r}+\frac{1}{r}\frac{\partial}{\partial r}\left(r\frac{\partial u}{\partial r}\right)+\frac{1}{r^2}\frac{\partial^2 u}{\partial \varphi^2}+\frac{\partial^2 u}{\partial z^2} && (3.28a)\\
\frac{\partial v}{\partial t} =& -\left(u_0\frac{\partial}{\partial r}+\frac{v_0}{r}\frac{\partial}{\partial \varphi}+w_0\frac{\partial}{\partial z}\right)v-\left(u\frac{\partial}{\partial r}+\frac{v}{r}\frac{\partial}{\partial \varphi}+w\frac{\partial}{\partial z}\right)v_0\\
&-\frac{1}{r}\frac{\partial p}{\partial \varphi}+\frac{1}{r}\frac{\partial}{\partial r}\left(r\frac{\partial v}{\partial r}\right)+\frac{1}{r^2}\frac{\partial^2 v}{\partial \varphi^2}+\frac{\partial^2 v}{\partial z^2} && (3.28b)\\
\frac{\partial w}{\partial t} =& -\left(u_0\frac{\partial}{\partial r}+\frac{v_0}{r}\frac{\partial}{\partial \varphi}+w_0\frac{\partial}{\partial z}\right)w-\left(u\frac{\partial}{\partial r}+\frac{v}{r}\frac{\partial}{\partial \varphi}+w\frac{\partial}{\partial z}\right)w_0\\
&-\frac{\partial p}{\partial z}+\frac{1}{r}\frac{\partial}{\partial r}\left(r\frac{\partial w}{\partial r}\right)+\frac{1}{r^2}\frac{\partial^2 w}{\partial \varphi^2}+\frac{\partial^2 w}{\partial z^2} && (3.28c)\\
\frac{\partial \theta}{\partial t} =& -\left(u_0\frac{\partial}{\partial r}+\frac{v_0}{r}\frac{\partial}{\partial \varphi}+w_0\frac{\partial}{\partial z}\right)\theta-\left(u\frac{\partial}{\partial r}+\frac{v}{r}\frac{\partial}{\partial \varphi}+w\frac{\partial}{\partial z}\right)\theta_0\\
&+\frac{1}{r}\frac{\partial}{\partial r}\left(r\frac{\partial \theta}{\partial r}\right)+\frac{1}{r^2}\frac{\partial^2 \theta}{\partial \varphi^2}+\frac{\partial^2 \theta}{\partial z^2} && (3.28d)\\
0 =& \frac{1}{r}\frac{\partial(ru)}{\partial r}+\frac{1}{r}\frac{\partial v}{\partial \varphi}+\frac{\partial w}{\partial z} \quad . && (3.28e)
\end{aligned}$$

Equations (3.28a)-(3.28e) are a system of 5 equations in 5 variables (u, v, w, p, θ) and 4 dimensions - 3 space (r, z, φ) and one time dimension (t). The general solution can be written as a superposition of normal modes

$$(\boldsymbol{u}, p, \theta)^T(r, \varphi, z, t) = (\hat{\boldsymbol{u}}, \hat{p}, \hat{\theta})^T(r, z)\, e^{\mathrm{i}m\varphi}e^{\lambda t} \quad , \tag{3.29}$$

with wave number m and complex growth rate $\lambda = \sigma + \mathrm{i}\omega$. Here λ is composed of a growth rate σ and an angular frequency ω. Using the normal mode Ansatz (3.29) and considering the axisymmetry of the basic flow

$$\partial_\varphi \boldsymbol{x}_0 = v_0 \equiv 0 \tag{3.30}$$

equations (3.28a)-(3.28e) become

$$\begin{aligned}
\lambda\hat{u} =& -\left(u_0\frac{\partial}{\partial r}+w_0\frac{\partial}{\partial z}\right)\hat{u}-\left(\hat{u}\frac{\partial}{\partial r}+\hat{w}\frac{\partial}{\partial z}\right)u_0-\frac{\partial \hat{p}}{\partial r}+\frac{1}{r}\frac{\partial}{\partial r}\left(r\frac{\partial \hat{u}}{\partial r}\right)\\
&-\frac{m^2}{r^2}\hat{u}+\frac{\partial^2 \hat{u}}{\partial z^2} && (3.31a)\\
\lambda\hat{v} =& -\left(u_0\frac{\partial}{\partial r}+w_0\frac{\partial}{\partial z}\right)\hat{v}-\frac{\mathrm{i}m}{r}\hat{p}+\frac{1}{r}\frac{\partial}{\partial r}\left(r\frac{\partial \hat{v}}{\partial r}\right)-\frac{m^2}{r^2}\hat{v}+\frac{\partial^2 \hat{v}}{\partial z^2} && (3.31b)
\end{aligned}$$

$$\lambda\hat{w} = -\left(u_0\frac{\partial}{\partial r} + w_0\frac{\partial}{\partial z}\right)\hat{w} - \left(\hat{u}\frac{\partial}{\partial r} + \hat{w}\frac{\partial}{\partial z}\right)w_0 - \frac{\partial\hat{p}}{\partial z} - \frac{m^2}{r^2}\hat{w}$$
$$+ \frac{1}{r}\frac{\partial}{\partial r}\left(r\frac{\partial\hat{w}}{\partial r}\right) + \frac{\partial^2\hat{w}}{\partial z^2} \tag{3.31c}$$
$$\lambda\hat{\theta} = -\left(u_0\frac{\partial}{\partial r} + w_0\frac{\partial}{\partial z}\right)\hat{\theta} - \left(\hat{u}\frac{\partial}{\partial r} + \hat{w}\frac{\partial}{\partial z}\right)\theta_0 + \frac{1}{r}\frac{\partial}{\partial r}\left(r\frac{\partial\hat{\theta}}{\partial r}\right)$$
$$- \frac{m^2}{r^2}\hat{\theta} + \frac{\partial^2\hat{\theta}}{\partial z^2} \tag{3.31d}$$
$$0 = \frac{1}{r}\frac{\partial(r\hat{u})}{\partial r} + \frac{\mathrm{i}m}{r}\hat{v} + \frac{\partial\hat{w}}{\partial z} \quad . \tag{3.31e}$$

To numerically implement equations (3.31a)-(3.31e) they need to be integrated over the *volume* $d\mathcal{S} = rdrdz$. The integrated equations are

$$\int_r\int_z r\lambda\hat{u}drdz + 2\int_z[r\hat{u}u_0]_{\Delta r}dz + \int_r[r\hat{u}w_0]_{\Delta z}dr + \int_r[r\hat{w}u_0]_{\Delta z}dr +$$
$$+ \int_z[r\hat{p}]_{\Delta r}dz - \int_r\int_z pdrdz - \int_z[r\partial_r\hat{u}]_{\Delta r}dz + \int_r\int_z\frac{\hat{u}}{r}(m^2+1)drdz -$$
$$- \int_r r[\partial_z\hat{u}]_{\Delta z}dr + \mathrm{i}\int_r\int_z\hat{v}\left(\frac{2}{r} + u_0\right)drdz = 0 \tag{3.32a}$$
$$\int_r\int_z r\lambda\hat{v}drdz + \int_z[r\hat{v}u_0]_{\Delta r}dz + \int_r[r\hat{v}w_0]_{\Delta z}dr + \int_r\int_z u_0\hat{v}dzdr +$$
$$+ \mathrm{i}\int_z\int_r m\hat{p}drdz - \int_z[r\partial_r\hat{v}]_{\Delta r}dz - \mathrm{i}\int_z\int_r\frac{2}{r}\hat{u}mdrdz + \int_r\int_z\frac{\hat{v}}{r}m^2drdz -$$
$$- \int_r r[\partial_z\hat{v}]_{\Delta z}dr + \int_r\int_z\frac{\hat{v}}{r}drdz = 0 \tag{3.32b}$$
$$\int_r\int_z r\lambda\hat{w}drdz + \int_z[r\hat{u}w_0]_{\Delta r}dz + 2\int_r[r\hat{w}w_0]_{\Delta z}dr + \int_z[r\hat{w}u_0]_{\Delta r}dz +$$
$$+ \mathrm{i}\int_r\int_z mw_0\hat{v}dzdr + \int_r[\hat{p}]_{\Delta z}dr - Gr\int_r\int_z r\hat{\theta}drdz - \int_z[r\partial_r\hat{w}]_{\Delta r}dz +$$
$$+ \int_r\int_z\frac{\hat{w}}{r}m^2drdz - \int_r r[\partial_z\hat{w}]_{\Delta z}dr = 0 \tag{3.32c}$$
$$\int_r\int_z r\lambda\hat{\theta}drdz + \int_z[r\hat{\theta}u_0]_{\Delta_r}dz + \int_r r[\hat{\theta}w_0]_{\Delta z}dr + \int_z[r\hat{u}\theta_0]_{\Delta_r}dz +$$
$$+ \int_r r[\hat{w}\theta_0]_{\Delta z}dr + \mathrm{i}\int_r\int_z\hat{\theta}m\hat{v}drdz -$$
$$- \frac{1}{Pr}\left(\int_z[r\partial_r\hat{\theta}]_{\Delta r}dz + \int_r\int_z\frac{m^2}{r}\hat{\theta}drdz - \int_r r[\partial_z\hat{\theta}]_{\Delta z}dr\right) = 0 \tag{3.32d}$$
$$\int[r\hat{u}]_{\Delta r}dz + \mathrm{i}\int\int m\hat{v}drdz + \int r[\hat{w}]_{\Delta z}dr = 0 \quad . \tag{3.32e}$$

Equations (3.32a)-(3.32e) then need to be transformed into a system of algebraic difference equations by means of finite volumes. To that end the integrals are approximated by the midpoint-rule and the variables evaluated by means of a first order difference scheme, compare sec. 3.1.5.

The system is completed by the boundary conditions for the perturbation equations. In in sec. 2.1.3 these boundary conditions have been given in terms of the total flow state

$$\boldsymbol{X} = \boldsymbol{x}_0 + \boldsymbol{x}. \tag{3.33}$$

Inserting (3.33) into these boundary conditions and taking into account that they are satisfied for $\boldsymbol{x}_0$, we get their formulation for the perturbation state $\boldsymbol{x}$.

The boundary conditions at the solid walls are

$$u = v = w = \theta = 0 \quad , \tag{3.34}$$

we assume no-slip and constant temperature at undeformable liquid–solid interface.

Inserting (3.33) into (2.33a)-(2.33c) and (2.28) we get the boundary conditions at the free surface

$$\partial_z u + \mathrm{Re}\,\partial_r \theta = 0 \quad \leftrightarrow \quad \text{radial shear stress} \tag{3.35a}$$

$$\partial_z v + \mathrm{Re}\,\frac{m}{r}\theta = 0 \quad \leftrightarrow \quad \text{azimuthal shear stress} \tag{3.35b}$$

$$w = 0 \quad \leftrightarrow \quad \text{no penetration} \tag{3.35c}$$

$$\partial_z \theta = 0 \quad \leftrightarrow \quad \text{insulating} \quad . \tag{3.35d}$$

Here the Ansatz of normal modes (3.29) was used. Conditions (3.35a) and (3.35b) represent the shear stress balance, while condition (3.35c) has to be satisfied to guarantee that the free surface is non-deformable. Note from condition (3.35d) that we assume no perturbation in the heat flux at the free surface, and neglect flow and heat transfer in the ambient gas phase.

The boundary conditions at the axis are given by

$$\partial_r u = v = \partial_r w = \partial_r \theta = 0 \quad \text{for} \quad m = 0 \tag{3.36a}$$

$$\partial_r u = v = w = \theta = 0 \quad \text{for} \quad m = 1 \tag{3.36b}$$

$$u = v = w = \theta = 0 \quad \text{for} \quad m > 1 \quad . \tag{3.36c}$$

Here the radial perturbation flow depends on the wave number m. For the derivation of these boundary conditions compare Kuhlmann & Rath (1993) and Xu & Davis (1984).

The system of algebraic difference equations resulting from the discretization of equations (3.32a)-(3.32e) and the corresponding boundary conditions (3.34)-(3.36) can be restated in the mathematical form of a classical generalized eigenvalue problem

$$(\boldsymbol{A} - \lambda \boldsymbol{B}) \cdot \hat{\boldsymbol{x}} = 0 \quad . \tag{3.37}$$

The eigenvalues of (3.37) are computed by means of an inverse iteration[4], which gives the eigenvalue λ closes to an initial guess $\lambda^{(0)}$. See also the gray box below.

[4]For more information on the inverse iteration compare Golub & van Loan (1989)

Inverse Iteration

(3.37) can be reformulated to give

$$(\boldsymbol{A} - \lambda \boldsymbol{B}) \cdot \hat{\boldsymbol{y}} = \boldsymbol{B}\hat{\boldsymbol{x}} \quad . \tag{3.38}$$

The Inverse Iteration consists of the following steps:

1. In the first step the system

$$(\boldsymbol{A} - \lambda^{(k)} \boldsymbol{B}) \cdot \hat{\boldsymbol{y}}^{(i+1)} = \boldsymbol{B}\hat{\boldsymbol{x}}^{(i)} \tag{3.39}$$

   is solved for $\hat{\boldsymbol{y}}^{(i+1)}$ by means of a LU-decomposition followed by back substitution. In the first iteration step the eigenvalue $\lambda^{(0)}$ and eigenvector $\hat{\boldsymbol{x}}^{(0)}$ are chosen at random.

2. In the next step the new residual $\hat{\boldsymbol{x}}^{(i+1)}$ is calculated by

$$\hat{\boldsymbol{x}}^{(i+1)} = \frac{\hat{\boldsymbol{y}}^{(i)}}{\|\hat{\boldsymbol{y}}^{(i)}\|_2} \quad . \tag{3.40}$$

3. Steps 1 and 2 are repeated until the exit condition

$$\left| \|(\hat{\boldsymbol{x}}^{(i+1)})^* \cdot \hat{\boldsymbol{x}}^{(i)}\|_2 - 1 \right| < \epsilon_{\mathrm{ev}} \tag{3.41}$$

   is satisfied[a].

4. As soon as condition (3.41) is satisfied the new eigenvalue $\lambda^{(k+1)}$ is computed by

$$\lambda^{(k+1)} = \lambda^{(k)} + \frac{1}{(\hat{\boldsymbol{x}}^{(i)})^* \cdot \hat{\boldsymbol{y}}^{(i+1)}} \quad . \tag{3.42}$$

5. Steps 1 through 4 are repeated until

$$\frac{|\lambda^{(k+1)} - \lambda^{(k)}|}{|\lambda^{(k+1)}|} < \epsilon_{\mathrm{ev}} \quad . \tag{3.43}$$

   Once (3.43) is satisfied an eigenvalue λ and the corresponding eigenvector $\hat{\boldsymbol{x}}$ has been found.

[a] Note that the order of magnitude of ϵ_{ev} is $O(10^{-7})$.

3.2.3 Secant Method - Tracing of the neutral Reynolds number

For the purpose of the present work it is not necessary to compute the full spectrum of eigenvalues, the eigenvalue with the largest real part $\Re(\lambda_{max}) = \max_i \Re(\lambda_i)$ suffices. In order to find this eigenvalue λ_{max} and the corresponding eigenvector $\hat{\boldsymbol{x}}$ for a first *estimate* of the neutral Reynolds number a series of eigenvalues is computed by the inverse iteration for a sufficient number of random initial guesses $\lambda_i^{(0)}$. The eigenvalue $\lambda^{(n-1)}$ with $\Re(\lambda^{(n-1)}) = \max_i \Re(\lambda_i^{(0)}) = \Re(\lambda_{max})$ can then be considered the complex growth rate of the estimated Reynolds number $\mathrm{Re}^{(n-1)}$. If $|\Re(\lambda^{(n-1)})| > \epsilon_{\mathrm{ev}}$ we perform a second inverse iteration[5] for a slightly larger Reynolds number $\mathrm{Re}^{(n)} = \mathrm{Re}^{(n-1)} + \epsilon$ and use the computed eigenvalue $\lambda^{(n)}$ to calculate a new estimate $\mathrm{Re}^{(n+1)}$ for the neutral Reynolds number by means of a secant method[6],

$$\mathrm{Re}^{(n+1)} = \mathrm{Re}^{(n)} - \sigma(\mathrm{Re}^{(n)}) \frac{\mathrm{Re}^{(n)} - \mathrm{Re}^{(n-1)}}{\sigma(\mathrm{Re}^{(n)}) - \sigma(\mathrm{Re}^{(n-1)})} \quad . \tag{3.44}$$

The advantage of the secant method is that in contrast to the Newton-Iteration-Method we don't necessarily need an explicit function to perform the root-finding. It is sufficient to know the function values $\sigma^{(n)} = \Re(\lambda^{(n)})$, $\sigma^{(n-1)} = \Re(\lambda^{(n-1)})$ at the two points $\mathrm{Re}^{(n)}$, $\mathrm{Re}^{(n-1)}$ at different iteration steps $(n), (n-1)$ to start the iteration. The iteration is stopped as soon as the variation of Re for two consecutive iteration steps is sufficiently small[7], i.e.

$$|\mathrm{Re}^{(n+1)} - \mathrm{Re}^{(n)}| < \epsilon_{\mathrm{Re}} \quad . \tag{3.45}$$

The secant method can be derived from the classical Newton-Iteration-Method by substituting the tangent by a secant passing through the points $(\mathrm{Re}^{(n)}, \sigma^{(n)})$ and $(\mathrm{Re}^{(n-1)}, \sigma^{(n-1)})$. It converges not as swift as the classical method but it is easier to implement.

Note that the growth rate σ depends on the parameters $\Xi_j = \{\mathrm{Re}, \mathrm{Gr}, \mathrm{Pr}, \Gamma\}$, hence so does the eigenvalue $\lambda = \lambda(\Xi_j)$. The tracing for the zero-growth rate $\sigma = \Re(\lambda) = 0$ described above can be performed for any parameter Ξ_j as long as all other parameters are kept constant. If more than one parameter is variable it is advisable to switch to a multidimensional secant method.

[5] Note that before the inverse iteration can be performed the basic state $\boldsymbol{x}_0$ needs to be updated for the new Reynolds number $\mathrm{Re}^{(n)}$.

[6] A detailed account on the secant method is given in J. H. Mathews (2004).

[7] Note that the order of magnitude of ϵ_{Re} is $O(10^{-7})$.

4 Validation of the Numerical Code

In order to assure that a numerical code gives correct results it must be validated. In case of the present problem formulation we do not have any experimental or numerical data to compare with. However results for a related problem, the half-zone problem are readily available. To that end compare Leypoldt (1999); Nienhüser (2002) and Wanschura (1996). Leypoldt (1999) treated the half-zone problem by means of a time-dependent three-dimensional simulation, a linear stability analysis was performed by Nienhüser (2002) and Wanschura (1996). Note that the linear stability analysis of the half-zone problem differs from the present analysis in terms of the boundary conditions only. To test the present code its boundary conditions are changed to suit the half-zone problem and its results compared to prior work on the half-zone problem.

In addition, the grid convergence of the computed results is evaluated. To that end some of the result expected for an infinite resolution are computed by means of a *Richardson extrapolation*. Its basic idea is the assumption that our numerical solution ϕ_h differs from the exact solution $\mathbf{\Phi}$ by a discretization error ϵ_h^d, mathematically speaking

$$\mathbf{\Phi} = \phi_h + \epsilon_h^d \quad , \tag{4.1}$$

where h is the size of a grid cell. We can approximate the discretization error ϵ_h^d by

$$\epsilon_h^d \approx \frac{\phi_h - \phi_{\alpha h}}{\alpha^p - 1} \quad , \tag{4.2}$$

with p being defined by

$$p = \frac{\log\left(\frac{\phi_{\alpha h} - \phi_{\alpha^2 h}}{\phi_h - \phi_{\alpha h}}\right)}{\log \alpha} \quad , \tag{4.3}$$

and α being the ratio of the two different cell sizes used in the extrapolation; for a detailed account compare Ferziger & Perić (2002).

4.1 Validation of the results for the Half-Zone

The half-zone model was originally devised in the context of crystal growth as a model for the floating-zone process. It has been extensively studied and many authors have contributed to a better understanding of the processes involved, to name but a few Chen & Hu (1997); Hyer *et al.* (1991); Kuhlmann (1996); Lappa *et al.* (2000, 2001*b*,*a*); Lappa & Savino (2002); Lappa (2005); Leypoldt (1999); Li *et al.* (2008*a*); Neitzel *et al.* (1993); Nienhüser (2002); Nienhüser & Kuhlmann (2002); Tang & Hu (1992); Wanschura *et al.* (1995*b*,*a*); Wanschura (1996); Wanschura *et al.* (1996). In the

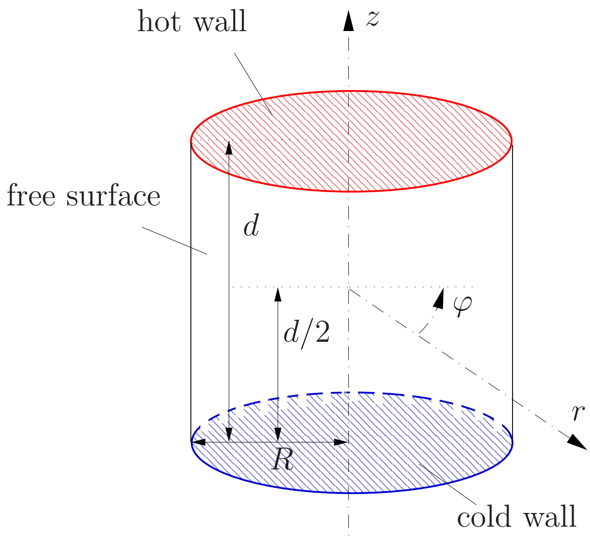

Figure 4.1: Geometry and coordinate system of the half-zone.

half-zone model we consider a cylindrical volume of fluid with height d and radius R defining an aspect ratio $\Gamma = R/d$, compare figure 4.1. The volume of fluid is bounded by a non-deformable free surface at the sides, a heated wall on top and a cooled wall below. The boundary conditions are given by

$$\mathbf{U} = 0 \qquad \leftrightarrow \qquad \text{no-slip} \tag{4.4a}$$

$$\mathsf{T} = \mathsf{T} + \frac{\Delta\mathsf{T}}{2} \qquad \leftrightarrow \qquad \text{heated wall} \tag{4.4b}$$

for the heated wall, and

$$\mathbf{U} = 0 \qquad \leftrightarrow \qquad \text{no-slip} \tag{4.5a}$$

$$\mathsf{T} = \mathsf{T} - \frac{\Delta\mathsf{T}}{2} \qquad \leftrightarrow \qquad \text{cooled wall} \tag{4.5b}$$

for the cooled wall. At the free surface they are

$$-\frac{1}{r}\mathsf{V} + \partial_r\mathsf{V} + \frac{\mathrm{Re}}{r}\partial_\varphi\mathsf{T} = 0 \qquad \leftrightarrow \qquad \text{azimuthal shear stress} \tag{4.6a}$$

$$\partial_r\mathsf{W} + \mathrm{Re}\partial_z\mathsf{T} = 0 \qquad \leftrightarrow \qquad \text{axial shear stress} \tag{4.6b}$$

$$\partial_r\mathsf{T} = 0 \qquad \leftrightarrow \qquad \text{insulating} \quad . \tag{4.6c}$$

The governing equations for the half-zone model (Boussinesq-approximation) are equivalent to equations (2.5a)-(2.5c) respectively (2.22a)-(2.22c) (dimensionless form) derived in sec. 2. For detailed picture of the problem formulation and the choice of boundary conditions compare Kuhlmann (1996) and Wanschura *et al.* (1995*b*).

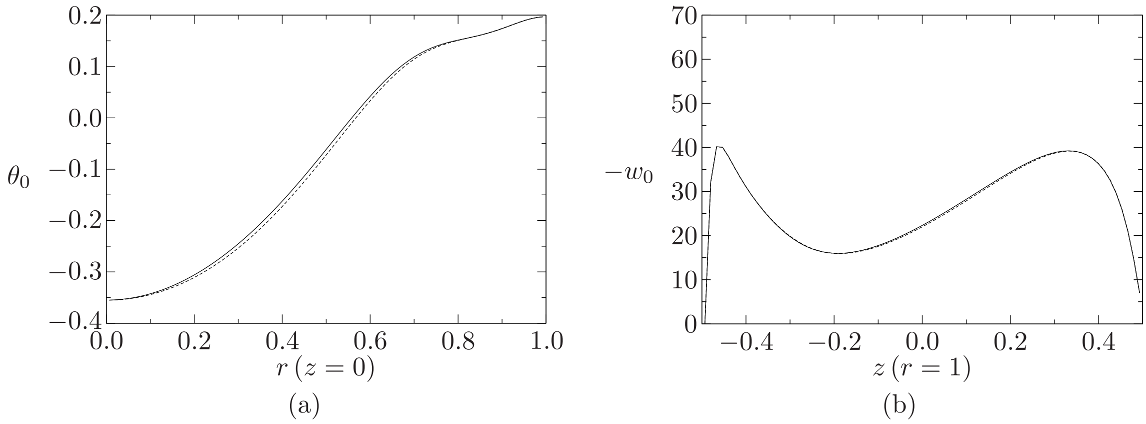

Figure 4.2: (a) Basic state temperature field $\theta_0(r)$ along the midplane ($z = 0$). (b) Basic state axial velocity w_0 at the free surface ($r = 1$). The parameters for (a) and (b) are: Pr $= 4$, $\Gamma = 1$ and Re $= 1047$. - The solid line (—) corresponds to the result of Domesi (2005) the dashed line (---) to the result of the present work. All solutions are computed on a uniform mesh with $N_r \times N_z = 75 \times 75$ cells.

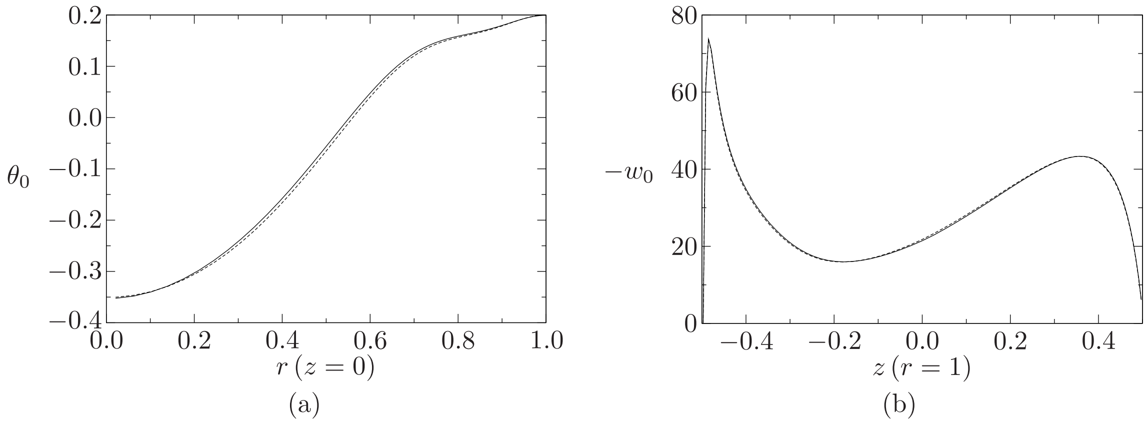

Figure 4.3: (a) Basic state temperature field $\theta_0(r)$ along the midplane ($z = 0$). (b) Basic state axial velocity w_0 at the free surface ($r = 1$). The parameters for (a) and (b) are: Pr $= 4$, $\Gamma = 1$ and Re $= 1047$. The grid stretching factors are $\delta_r = \delta_z = 0.96$. - The solid line (—) corresponds to the result of Domesi (2005) the dashed line (---) to the result of the present work. All solutions are computed on a non-uniform mesh with $N_r \times N_z = 75 \times 75$ cells.

4.1.1 Validation of the basic state

Data for validation of the basic state was provided by Domesi (2005). Available data features the basic state temperature field θ_0 at the midplane ($z = 0$) as a function of the radius, and the axial basic flow velocity component w_0 at the free surface ($r = 1$) as a function of z. These results were computed both on a uniform and a non-uniform

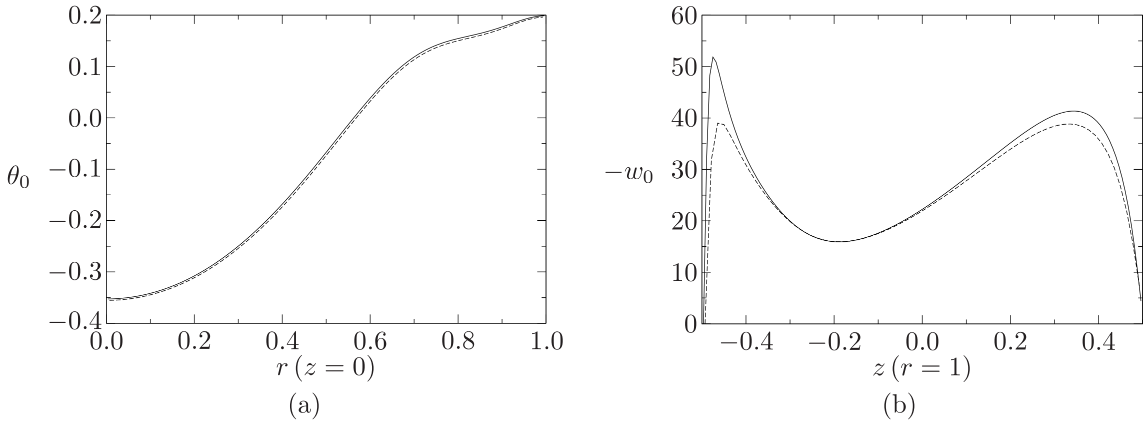

Figure 4.4: (a) Basic state temperature field $\theta_0(r)$ along the midplane, $(z = 0)$. (b) Basic state axial velocity w_0 at the free surface $(r = 1)$. The parameters for (a) and (b) are: $\Pr = 4$, $\Gamma = 1$ and $\mathrm{Re} = 1047$. - The solid line (—) corresponds to a resolution of $N_r \times N_z = 140 \times 140$ cells and the dashed line (- - -) to $N_r \times N_z = 70 \times 70$ respectively.

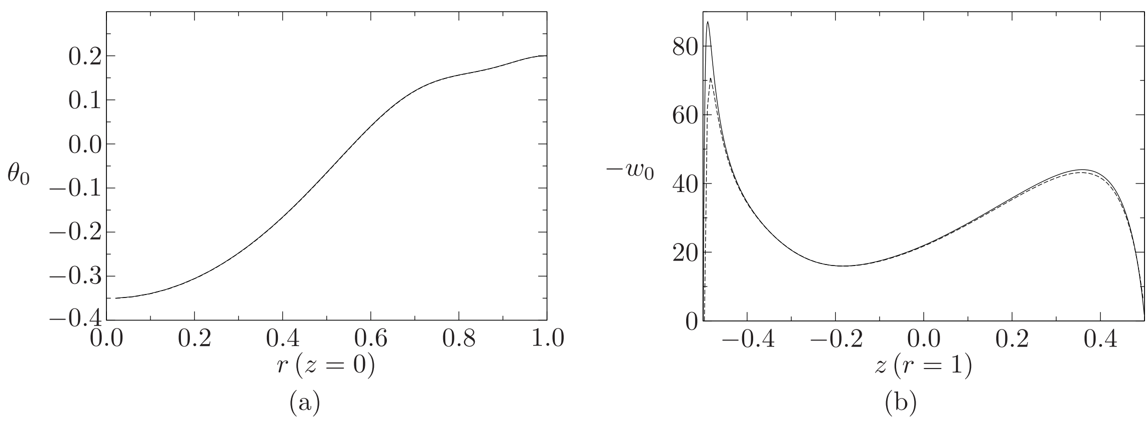

Figure 4.5: (a) Basic state temperature field $\theta_0(r)$ along the midplane $(z = 0)$. (b) Basic state axial velocity w_0 at the free surface $(r = 1)$. The parameters for (a) and (b) are: $\Pr = 4$, $\Gamma = 1$ and $\mathrm{Re} = 1047$. The grid stretching factors are $\delta_r = \delta_z = 0.96$. - The solid line (—) corresponds to a resolution of $N_r \times N_z = 140 \times 140$ cells and the dashed line (- - -) to $N_r \times N_z = 70 \times 70$ respectively.

grid with $N_r \times N_z = 75 \times 75$ computational cells for parameters $Re = 1047$, $\Pr = 4$, $\mathrm{Gr} = \mathrm{Bi} = 0$ and $\Gamma = 1$. Computations performed with the present code display very good agreement, compare in figures 4.2 and 4.3. Stretching factors $\delta_r = \delta_z = 0.96$ were used for the non-uniform grid. In radial direction all cells are compressed towards the free surface. In axial direction half of the cells are compressed towards the bottom and the other half towards the top.

For a test of the influence of the grid resolution on the above profiles computations on

Re	1000	3000	5000	7000	Reference
Pr= 0.02	8.87	7.18	6.31	5.71	Wanschura (1996)
	8.93	7.18	6.31	5.65	Leypoldt (1999)
	8.88	7.15	6.26	5.66	present work
Pr= 4.00	2.33	2.05	1.95	1.88	Wanschura (1996)
	2.35	2.09	1.97	1.86	Leypoldt (1999)
	2.36	2.10	1.97	1.86	present work

Table 4.1: Minimum of the basic state stream function $\psi_0^{min} \times \left(-10^3/\text{Re}\right)$ for parameters $\text{Bi} = \text{Gr} = 0$, $\Gamma = 1$ and $\text{Pr} = 0.02$ respectively $\text{Pr} = 4$. - The results of Leypoldt (1999) and the present work have been computed on a grid with $N_r \times N_z = 30 \times 30$ cells.

both uniform and non-uniform grids were performed for resolutions $N_r \times N_z = 70 \times 70$ and $N_r \times N_z = 140 \times 140$. The results are displayed in figures 4.4 and 4.5. The agreement of the solutions for resolutions $N_r \times N_z = 70 \times 70$ and $N_r \times N_z = 140 \times 140$, with $\parallel \theta_0^{70} - \theta_0^{140} \parallel < 0.05$ and $\parallel w_0^{70} - w_0^{140} \parallel < 0.05$, is very good[1]. On a uniform grid the results are still good yet there are some deviations in the peak values of the free surface axial velocity.
The minimum value of the basic state stream function ψ_0^{min} was computed for Reynolds numbers Re = 1000, 3000, 5000 and 7000 and parameters $\Gamma = 1$, $\text{Bi} = \text{Gr} = 0$ and $\text{Pr} = 0.02$ respectively $\text{Pr} = 4$ on a uniform grid with $N_r \times N_z = 30 \times 30$ computational cells[2]. The results were compared to those computed by Leypoldt (1999); Wanschura (1996). Again we find very good agreement, compare table 4.1.

4.1.2 Validation of the stability analysis

For the validation of the linear stability analysis we compare with available data and check grid convergence.

Table 4.2 shows that the results compare very well to those of Nienhüser (2002) and Wanschura (1996). For both low (Pr=0.02) and high Prandtl numbers (Pr=4) the deviation of the neutral Reynolds numbers Re_n and frequencies ω_n from reference data is less than 5%, in most cases less than 1%.

To check grid convergence, a series of neutral Reynolds numbers and frequencies has been computed for resolutions ranging from $N_r \times N_z = 25 \times 25$ to $N_r \times N_z = 100 \times 100$ cells and Prandtl numbers $\text{Pr} = 0.02$ respectively $\text{Pr} = 4$, compare table 4.3. The dependence of the neutral quantities on the resolution is depicted in figures 4.6 and 4.7a,b.

[1] Note that in general a solution is considered *well converged* if the distance between the two curves y^n and y^{2n} is sufficiently small $\parallel y^n - y^{2n} \parallel < \epsilon_{\text{num}}$. Here n is the grid resolution and $\epsilon_{\text{num}} = 0.05$ the numerical error which is typically considered acceptable.

[2] Though the low resolution of $N_r \times N_z = 30 \times 30$ is not sufficiently fine to consider the computed solution well converged the agreement is very good. No other data is available for comparison of the minimum of the basic state stream function ψ_0^{min}.

Pr	Re_n	deviation	ω_n	deviation	reference
0.02	2067		0.0		present work
	2060	-0.3%	0.0	-0.0%	Nienhüser (2002)
	2062	-0.2%	0.0	-0.0%	Wanschura *et al.* (1995*b*)
4.00	1006		28.8		present work
	1010	+0.4%	28.5	-1.0%	Nienhüser (2002)
	1047	+4.1%	27.9	-3.1%	Wanschura *et al.* (1995*b*)

Table 4.2: Neutral frequencies ω_n and Reynolds numbers Re_n for a neutral mode with wave number $m = 2$, aspect ratio $\Gamma = 1$ and Prandtl numbers $\mathrm{Pr} = 0.02$ respectively $\mathrm{Pr} = 4$. The results of Nienhüser (2002) and the present work have been extrapolated by means of the Richardson extrapolation (4.1). The results of Wanschura *et al.* (1995*b*) are obtained applying a Chebychev collocation method with $M = 25$ points in radial direction and a second-order-difference scheme with $N = 80$ points in axial direction.

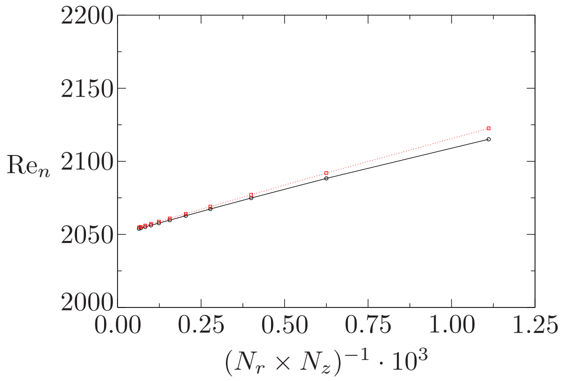

Figure 4.6: Neutral Reynolds number Re_n for Prandtl number $\mathrm{Pr} = 0.02$ ($\omega_c = 0$ for $\mathrm{Pr} = 0.02$) as a function of the grid resolution $(N_r \times N_z)^{-1}$. - The solid black line (—) represents the solution on a uniform grid, and the dotted red line ($\cdots$) on a non-uniform grid with stretching factors $\delta_r = \delta_z = 0.98$.

All solutions were computed on uniform and non-uniform grids in order to make visible the effect of the local grid refinement on the accuracy of the solution.

From the results presented in table 4.3 and figures 4.6 and 4.7a,b we conclude that a non-uniform grid with a resolution of $N_r \times N_z = 70 \times 70$ cells is sufficient for a quantitative stability analysis of the half-zone problem.
Note that the linear dependence on the uniform grid reflects the 2nd order of the numerical scheme. Grid stretching, though formally reducing the order of the scheme, improves the convergence due to the local refinement.

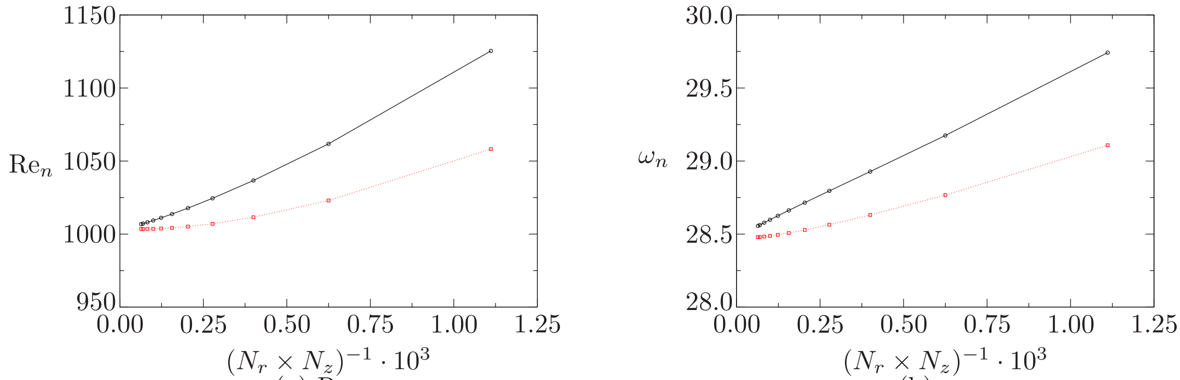

(a) Re_n (b) ω_n

Figure 4.7: (a) Neutral Reynolds numbers Re_n and (b) neutral frequency ω_n for Prandtl number $\mathrm{Pr} = 4$ as a function of the grid resolution $(N_r \times N_z)^{-1}$. - The solid black line (—) represents the solution on a uniform grid, and the dotted red line ($\cdots$) on a non-uniform grid with stretching factors $\delta_r = \delta_z = 0.98$.

$N_r \times N_z$	$\mathrm{Pr} = 0.02$		$\mathrm{Pr} = 4$	
	Re_n	ω_n	Re_n	ω_n
25×25	1059	29.04	2170	0.0
30×30	1032	28.80	2136	0.0
40×40	1014	28.60	2104	0.0
50×50	1009	28.52	2089	0.0
60×60	1007	28.49	2082	0.0
70×70	1007	28.48	2077	0.0
80×80	1006	28.48	2075	0.0
90×90	1006	28.48	2073	0.0
100×100	1006	28.48	2072	0.0
p	-5.15	-5.09	-2.20	

Table 4.3: Neutral frequencies ω_n and neutral Reynolds number Re_n of the neutral mode with wave number $m = 2$, aspect ratio $\Gamma = 1$ and Prandtl number $\mathrm{Pr} = 0.02$ respectively $\mathrm{Pr} = 4$. Computations have been performed on a non-uniform grid with $N_r \cdot N_z$ grid cells and stretching factor $\delta_r = \delta_z = 0.98$. p is the calculated order of convergence (4.3), compare Ferziger & Perić (2002).

4.2 Validation of the present code

Since there do not exist prior investigations of the stability boundaries of the problem studied in the present work, we can only perform a convergence study.

4.2.1 Validation of the basic state

For the validation of the basic state we have decided to study the radial basic state velocity u_0 at the free surface and along a line parallel to the axis at a radial position of $r = 0.25$. Computations performed on uniform and non-uniform grids for parameters $\Gamma = 1$, $\mathrm{Gr} = \mathrm{Bi} = 0$ and $\mathrm{Pr} = 0.0316$ respectively $\mathrm{Pr} = 3.98$ at resolutions of $N_r \times N_z = 60 \times 60$ and $N_r \times N_z = 120 \times 120$ cells are shown in figures 4.8 and 4.9.

Figure 4.8 shows that the convergence of the radial basic state velocity u_0 as a function of the axial position z is captured very well on both unifom grids for low and high Prandtl numbers, yet can still be significantly increased by using a non-uniform grid. Note that the solution on a non-uniform grid with $N_r \times N_z = 60 \times 60$ cells is almost as good as on a uniform grid with $N_r \times N_z = 120 \times 120$ cells.

A comparison of the radial basic state velocity u_0 at the free surface gives similar results, cp. figure 4.9a,b. For a low Prandtl number ($\mathrm{Pr} = 0.0316$) all non-uniform grids and the uniform grid with resolution $N_r \times N_z = 120 \times 120$ capture the solution very well, compare figure 4.9a, while a uniform grid with $N_r \times N_z = 60 \times 60$ cells is too coarse-mesh. For high Prandtl number ($\mathrm{Pr} = 3.98$) fig. 4.9b shows a peak in the solution structure close to the cold corner. A feature appearing also in the floating zone problem where it has been studied by Wanschura (1996)[3].

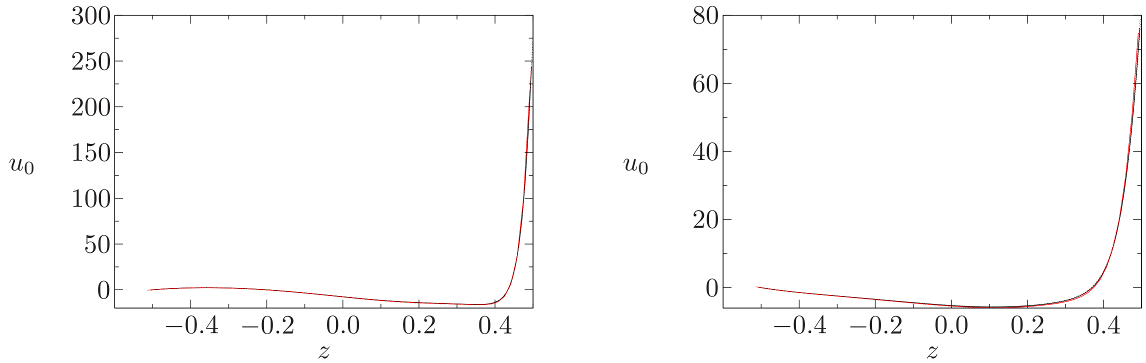

(a) $\mathrm{Pr} = 0.0316$

(b) $\mathrm{Pr} = 3.98$

Figure 4.8: Radial basic state velocity u_0 in axial direction at radial position $r = 0.25$ at neutral Reynolds number Re_n. (a) Results for low Prandtl number ($\mathrm{Pr} = 0.0316$) and (b) high Prandtl number ($\mathrm{Pr} = 3.98$) - Black and red lines depict a resolution of $N_r \times N_z = 120 \times 120$ respectively $N_r \times N_z = 60 \times 60$ cells. Solid and dotted lines indicate a uniform grid respectively non-uniform grid with stretching factor $\delta_r = \delta_z = 0.98$.

A solution is considered well converged (resolution-independent) if it does not change due to an increase in resolution. Theoretically solutions computed on a uniform grid should be identical to those on a non-uniform grid for $N_r \to \infty, N_z \to \infty$. Both solutions should converge towards the same limit solution. In practice the resolution remains finite, with it the numerical error ϵ_{num}, and hence the solutions will not be identical.

[3] Wanschura (1996) gives details on how the peak can be treated by means of regularization functions.

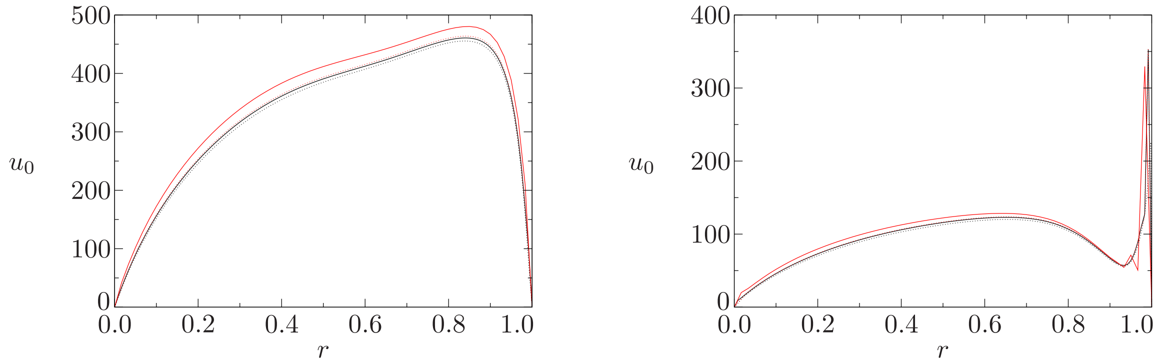

(a) $\mathrm{Pr} = 0.0316$ (b) $\mathrm{Pr} = 3.98$

Figure 4.9: Radial basic state velocity u_0 in radial direction at the free surface $z = 0.5$ at neutral Reynolds number Re_n. (a) For low Prandtl number $\mathrm{Pr} = 0.0316$, and (b) high Prandtl number $\mathrm{Pr} = 3.98$ respectively. - Black and red lines depict a resolution of $N_r \times N_z = 120 \times 120$ respectively $N_r \times N_z = 60 \times 60$ cells. Solid lines indicate a uniform grid, while dotted lines indicate a non-uniform grid with stretching factor of $\delta_r = \delta_z = 0.98$.

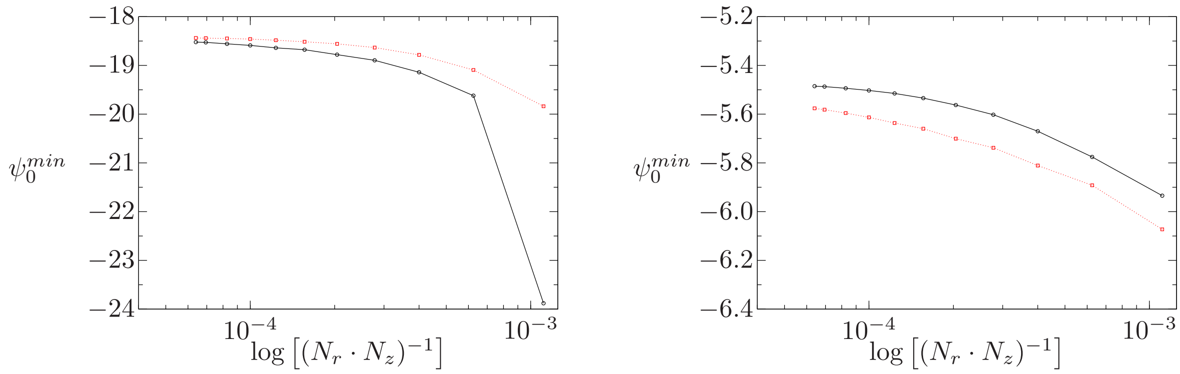

(a) $\mathrm{Pr} = 0.0316$ (b) $\mathrm{Pr} = 3.98$

Figure 4.10: Minimum of the basic state streamfunction ψ_0^{min} as a function of the grid resolution $(N_r \cdot N_z)^{-1}$. (a) For low Prandtl number ($\mathrm{Pr} = 0.0316$) and (b) high Prandtl number ($\mathrm{Pr} = 3.98$). - The solid black and dotted red lines represent the solution on a uniform grid respectively non-uniform grid with stretching factor $\delta_r = \delta_z = 0.98$.

In figures 4.10a,b the minimum of the basic state stream function ψ_0^{min} is shown as a function of the inverse of the grid resolution $(N_r \cdot N_z)^{-1}$ for a uniform (solid black line) and a non-uniform grid (dotted red line). For both Prandtl numbers ψ_0^{min} features a clear trend of convergence towards the same limit value of ψ_0^{min} for the uniform and the non-uniform grid in the limit $N_r \to \infty, N_z \to \infty$. Note that the ratios of the minimum stream function on the non-uniform and the uniform grid ($\tilde{\psi}_0^{nu,u} = \psi_0^{min,nu} / \psi_0^{min,u}$) for a resolution of $N_r \cdot N_z \gtrsim 125 \times 125$ cells are $\tilde{\psi}_0^{nu,u} \lesssim 1.005$ (for $\mathrm{Pr} = 0.0316$) and

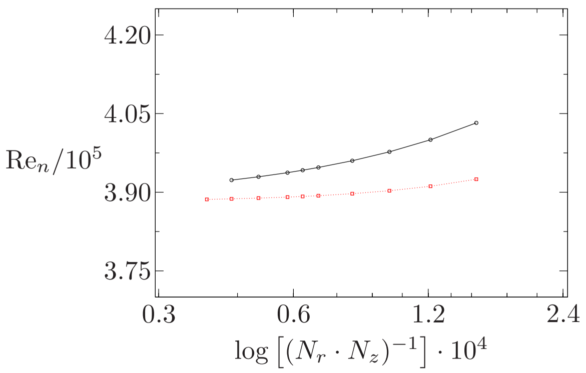

Figure 4.11: Neutral Reynolds number Re_n for Prandtl number $\mathrm{Pr} = 0.0316$ ($\omega_c = 0$ for $\mathrm{Pr} = 0.0316$) as a function of the grid resolution $(N_r \cdot N_z)^{-1}$. - The solid black line (—) represents the solution on a uniform grid, and the dotted red line ($\cdots$) on a non-uniform grid with stretching factors $\delta_r = \delta_z = 0.98$.

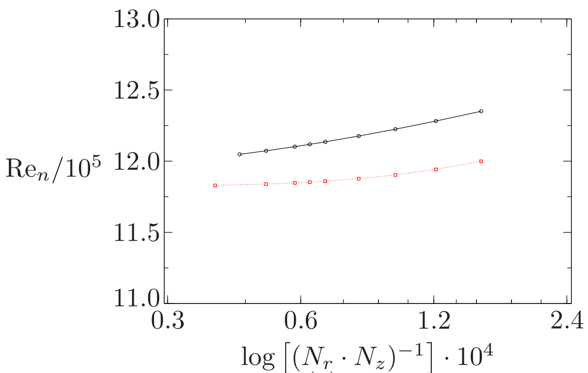

(a) Re_n

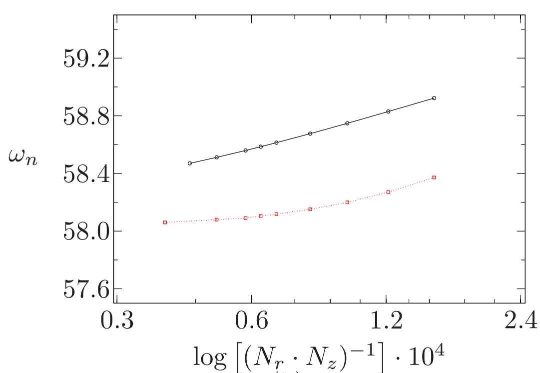

(b) ω_n

Figure 4.12: (a) Neutral Reynolds number Re_n and (b) neutral frequency ω_n for Prandtl number $\mathrm{Pr} = 3.98$ as a function of the grid resolution $(N_r \cdot N_z)^{-1}$. - The solid black line (—) represents the solution on a uniform grid, and the dotted red line ($\cdots$) on a non-uniform grid with stretching factors $\delta_r = \delta_z = 0.98$.

$\tilde{\psi}_0^{nu,u} \lesssim 1.017$ (for $\mathrm{Pr} = 3.98$). Hence convergence is satisfactory.

4.2.2 Validation of the stability analysis

Without reference data we must restrict ourselves to a validation of the convergence of the neutral Reynolds number Re_n and frequency ω_n. The results computed on a non-uniform grid for a series of resolutions from $N_r \times N_z = 30 \times 30$ to $N_r \times N_z = 160 \times 160$ and parameters $\Gamma = 1$, $\mathrm{Bd} = 0$, $m = 3$, and $\mathrm{Pr} = 0.0316$ respectively $\mathrm{Pr} = 3.98$ are shown in table 4.4 and figures 4.11 and 4.12a,b. In all cases the convergence is very good.

The high accuracy of the data is easily seen from figures 4.11 and 4.12a,b if the ratios

$N_r \times N_z$	Pr = 0.0316		Pr = 3.98	
	Re_n	ω_n	Re_n	ω_n
30×30	45988	0.00	127265	59.42
40×40	42088	0.00	126200	59.26
50×50	40584	0.00	123845	58.97
60×60	39854	0.00	122063	58.71
70×70	39468	0.00	120830	58.51
80×80	39248	0.00	119989	58.37
90×90	39114	0.00	119419	58.27
100×100	39029	0.00	119032	58.20
110×110	38972	0.00	118770	58.15
120×120	38934	0.00	118592	58.12
130×130	38907	0.00	118471	58.09
140×140	38888	0.00	118389	58.08
150×150	38874	0.00		
160×160	38863	0.00	118293	58.06
$\mathbf{\Phi}$	38817	0.00	118125	58.05
p	3.23		3.54	5.26
ϵ_h^d	-46.25		-168.604	-0.02

Table 4.4: Grid resolution dependence of the neutral Reynolds number Re_n and neutral frequency ω_n. The parameters are: $m = 3$, $\Gamma = 1$, $\mathrm{Pr} = 0.0316$ respectively $\mathrm{Pr} = 3.98$. The values are given for a fully stretched non-uniform grid ($\delta_r = \delta_z = 0.98$). $\mathbf{\Phi}$ was calculated using three grids with resolutions 90×90, 120×120 and 160×160. p is the calculated order of convergence, and ϵ_h^d the discretization error calculated according to Ferziger & Perić (2002).

of the neutral Reynolds numbers and frequencies on non-uniform and uniform grids are compared for $N_r \times N_z = 140 \times 140$ grid cells. The ratios are $\tilde{\mathrm{Re}}_n^{nu,u} = \mathrm{Re}_n^u/\mathrm{Re}_n^{nu} \lesssim 1.01$ (for $\mathrm{Pr} = 0.0316$) and $\tilde{\mathrm{Re}}_n^{nu,u} = \mathrm{Re}_n^u/\mathrm{Re}_n^{nu} \lesssim 1.02$ respectively $\omega^{nu,u} = \omega_n^u/\omega_n^{nu} \lesssim 1.007$ (for $\mathrm{Pr} = 3.98$).

We conclude that grid convergence of the neutral Reynolds numbers and frequencies is very satisfying.

4.3 Conclusions on the validation process

The code developed in the course of the present work is suitable for our purpose. Grid convergence is very satisfying and the results computed for the halz-zone model show very good agreement to prior work by other authors. Hence, the code can be expected to yield suitably converged results.

4.4 Some remarks on the magnitude of the thermocapillary Reynolds number

As mentioned in sec. 2.1.4 the temperature difference $\Delta\mathsf{T}$ in the definition of the thermocapillary Reynolds number

$$\mathrm{Re} = \frac{\gamma \Delta\mathsf{T} d}{\rho \nu^2} \tag{4.7}$$

is given in terms of the maximum heat flux $\Delta\mathsf{T}^{\mathrm{Q}} = Q_{max} d/k$ for the present problem and in terms of the temperature difference between the hot and the cold free-surface corner $\Delta\mathsf{T}^{\mathrm{HZ}} = \mathsf{T}_c - \mathsf{T}_0$ for the half-zone model. Hence due to the choice of ΔT the magnitude of the critical Reynolds numbers

$$\mathrm{Re}^{\mathrm{Q}} = \frac{\gamma \Delta\mathsf{T}^{\mathrm{Q}}}{\rho\nu}\frac{d}{\nu} \quad \text{and} \quad \mathrm{Re}^{\mathrm{HZ}} = \frac{\gamma \Delta\mathsf{T}^{\mathrm{HZ}}}{\rho\nu}\frac{d}{\nu} \quad , \tag{4.8}$$

will not necessarily be of the same order in both problems. Reformulation of (4.8) gives the relation

$$\mathrm{Re}^{\mathrm{HZ}} = \frac{\Delta\mathsf{T}^{\mathrm{HZ}}}{\Delta\mathsf{T}^{\mathrm{Q}}}\mathrm{Re}^{\mathrm{Q}} \quad , \tag{4.9}$$

which can be used to check whether choosing ΔT as temperature difference between the center and the rim of the pool[4] yields Reynolds numbers comparable to those computed in prior work for the half-zone model. Indeed typical neutral Reynolds numbers $\mathrm{Re}^{\mathrm{HZ}}$ are in the range of $O(10^3)$ to $O(10^4)$. An order of magnitude corresponding very well to order of magnitude of the neutral Reynolds numbers in the floating zone problem, compare Kuhlmann (1999); Wanschura (1996).

[4]This is equivalent to the difference between the hottest and the coldest value of temperature at the free surface.

5 Results

The presentation and discussion of the results is split in two parts. The results computed for the liquid-pool model of fusion welding are presented in sec. 5.1. A *standard configuration* is defined and a wide range of parameters studied. In sec. 5.2 we present some results on the annular pool problem and give a detailed comparison with prior experimental and numerical work by Kamotani *et al.* (1992).

5.1 Results on the liquid-pool model

5.1.1 The standard configuration

To explore the dependence of the critical Reynolds number on the parameters Γ and Bd respectively Gr we define a reference system. The reference configuration is defined by unit aspect ratio $\Gamma = 1$ and zero-gravity conditions $\mathrm{Bd} = 0$. Computations for this configuration have been performed for Prandtl numbers ranging from $\mathrm{Pr} = 10^{-3}$ to 10. The resulting basic states, stability boundaries, and physical instability mechanisms are discussed in the following.

Basic states at low and high Prandtl numbers

The parabolic heat-flux profile on the free surface creates a non-uniform temperature distribution which drives a free-surface flow away from the central hot region to the periphery via the thermocapillary effect. At the periphery of the pool the free-surface flow is forced downwards into the bulk by continuity, the basic flow pattern typically is a toroidal vortex. It will be called, henceforth, the *primary vortex*. In case of flow separation a *secondary* counter-rotating vortex may appear.

As a representative low-Prandtl-number case we consider $\mathrm{Pr} = 0.02$. The basic flow and temperature field are shown in figs. 5.1a,b at the critical Reynolds number $\mathrm{Re}_c = 34,709$. The basic vortex is essentially confined to the cold upper corner. The flow in the bottom half consists of a weak secondary vortex. At criticality transport of basic state temperature is dominantly conductive at this low value of Prandtl number. The apparently high Reynolds number results from the current scaling, cp. sec. 4.4. The relative importance of the convective to the conductive heat transport is given by the Peclet or Marangoni number

$$\mathrm{Ma} = \frac{U_{\mathrm{th}} d}{\kappa} = \mathrm{Pr}\,\mathrm{Re}. \tag{5.1}$$

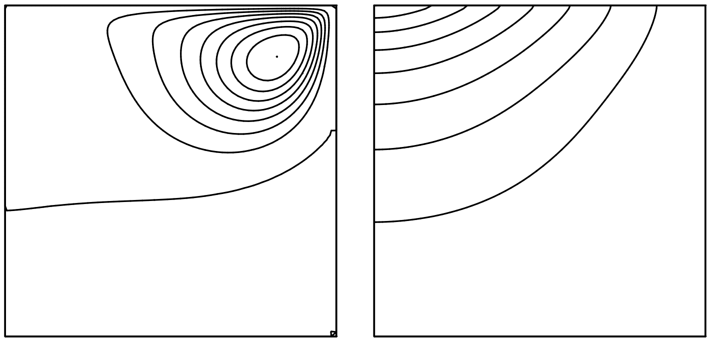

(a) ψ_0, $\mathrm{Pr} = 0.02$, $\mathrm{Re}_c = 34,709$

(b) θ_0, $\mathrm{Pr} = 0.02$, $\mathrm{Re}_c = 34,709$

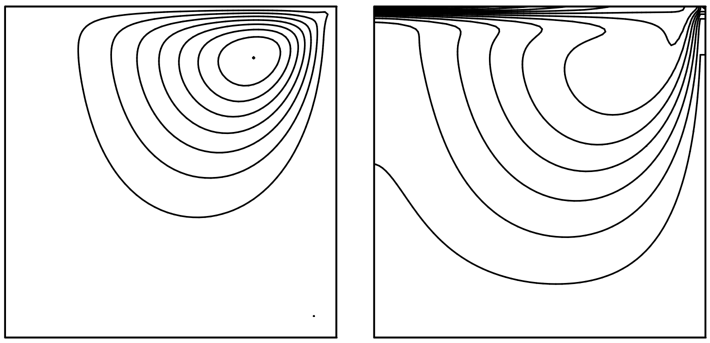

(c) ψ_0, $\mathrm{Pr} = 4$, $\mathrm{Re}_c = 110,362$

(d) θ_0, $\mathrm{Pr} = 4$, $\mathrm{Re}_c = 110,362$

Figure 5.1: Stream function ψ_0 and temperature isolines θ_0 of the basic state at the critical Reynolds number $\mathrm{Re} = \mathrm{Re}_c$ for unit aspect ratio $\Gamma = 1$, $\mathrm{Bd} = 0$, and $\mathrm{Pr} = 0.02$ ($\Delta\psi_0 = 2.046$, $\Delta\theta_0 = 0.0301$) (a,b) and $\mathrm{Pr} = 4$ ($\Delta\psi_0 = 0.588$, $\Delta\theta_0 = 0.0015$)(c,d). The flow is clockwise ($\psi_0 < 0$).

Hence, the critical Marangoni number[1] is only $\mathrm{Ma}_c = 694$.

As a representative high-Prandtl-number case we show the basic state at criticality in figs. 5.1c,d. The critical Reynolds number $\mathrm{Re}_c = 110,362$ is about three times as high as for $\mathrm{Pr} = 0.02$. The toroidal vortex does not differ much from the one for $\mathrm{Pr} = 0.02$. Since it extends deeper into the liquid pool, the streamlines are somewhat closer to circular and the separated flow region is absent. However, the critical Marangoni number $\mathrm{Ma}_c = \mathrm{Pr}\mathrm{Re}_c = 441,448$ is about three orders of magnitude larger than for $\mathrm{Pr} = 0.02$ indicating the dominating convective effect on the temperature field. This is clearly seen

[1]Note that the critical Marangoni number is still high due to the scaling of the temperature difference $\Delta\mathsf{T}$ by the heat flux $\Delta\mathsf{T} = Q_{max}d/k$. Compare sec. 2.1.4.

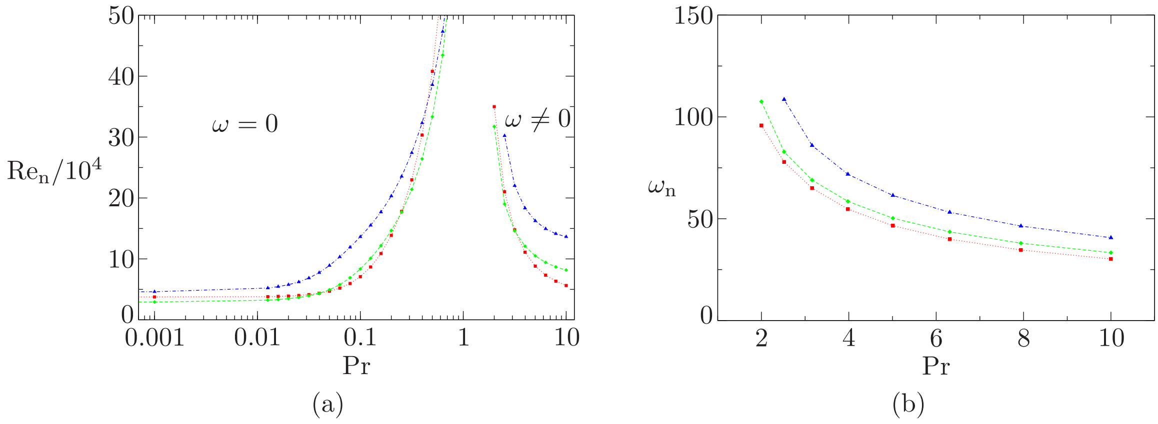

Figure 5.2: Prandtl number dependence of the (a) neutral Reynolds numbers $\mathrm{Re_n}$ (b) neutral frequencies ω_n for the standard configuration with parameters $\Gamma = 1$ and $\mathrm{Bd} = 0$. - The neutral wave number $m = m_\mathrm{n}$ are $m = 2$:$\cdots$, $m = 3$:- - - -, and $m = 4$:-·-·-.

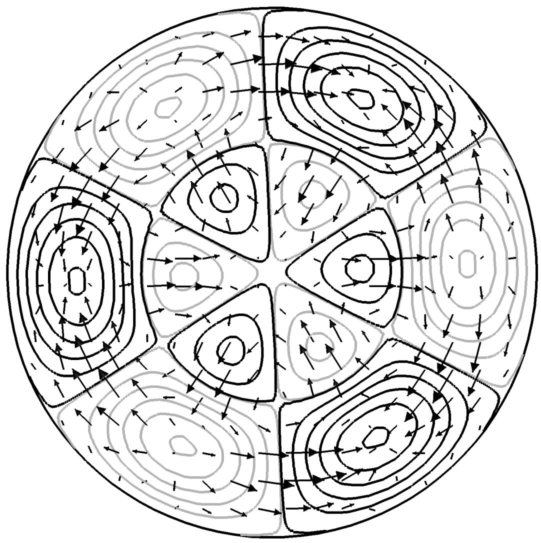

Figure 5.3: Perturbation flow (arrows) and perturbation temperature field (isolines) on the free surface at $z = 0.5$ for $\mathrm{Pr} = 0.02$. Negative values are indicated by gray lines. The parameters are $m_c = 3$ and $\mathrm{Re}_c = 34,709$.

in fig. 5.1d: The isotherms exhibit a strong convective crowding and thermal boundary layers are about to develop on the free surface and along the side wall.

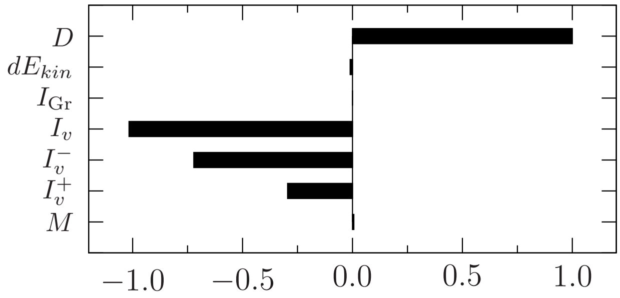

Figure 5.4: Terms of the kinetic energy balance (2.43) for $\Gamma = 1$, $\mathrm{Pr} = 0.02$, and $m = 3$ at the critical Reynolds number $\mathrm{Re}_c = 34,709$. The different terms are referred to in the text.

Stability boundaries

Neutral stability boundaries (the neutral Reynolds numbers Re_n) have been computed for wave numbers $m = 1$ to 7. The most dangerous ones, i.e. $m = 2$, 3, and 4, are shown in fig. 5.2a. Their lower envelope yields the critical stability boundary. From the critical curve it is seen that the asymptotic range for $\mathrm{Pr} \to 0$ has been reached, which has been confirmed by additional calculations for $\mathrm{Pr} = 10^{-10}$. The neutral frequencies ω_n for $\mathrm{Pr} \gtrsim 2$ are displayed in figure 5.2b.

The neutral Reynolds numbers are of the order of $O(\mathrm{Re}) \approx 10^5$. The magnitude results from the temperature scale $\Delta T = Q^{\max}/k$. It is directly defined by the boundary conditions. If we had used the de-facto temperature drop from the center of the pool to the rim the neutral Reynolds numbers would be of the order of $O(\mathrm{Re}) \approx 10^3$. However, the surface temperature drop is part of the solution and can only be determined a posteriori, cp. sec. 2.1.4.

From fig. 5.2 two ranges can be distinguished: For low Prandtl numbers ($\mathrm{Pr} \lesssim 1$) the basic state flow is unstable to a stationary non-axisymmetric perturbation mode, the critical wave number being either $m_c = 2$ or 3, depending on Prandtl number. For high Prandtl numbers ($\mathrm{Pr} \gtrsim 1$) the basic state is unstable to a time-dependent non-axisymmetric mode with critical wave number $m_c = 2$.

Low-Prandtl-number instability mechanism

For the stationary instability at $\mathrm{Pr} = 0.02$ the critical Reynolds number is $\mathrm{Re}_c = 34,709$ with a critical wave number $m_c = 3$. Figure 5.3 shows the critical perturbation velocity field $\boldsymbol{u}$ and the perturbation temperature T at the free surface at $z = 0.5$. Strong and weak temperature extrema arise near the axis and the rim of the pool, respectively. The radial surface flow between two neighboring strong and weak extrema is consistent with the thermocapillary effect, i.e. radial perturbation flow and surface forces caused by the perturbation temperature field are parallel ($\gamma > 0$). The azimuthal perturbation flow between adjacent strong temperature extrema, however, is opposite to the azimuthal thermocapillary stresses. Hence, the azimuthal motion cannot be created by the ther-

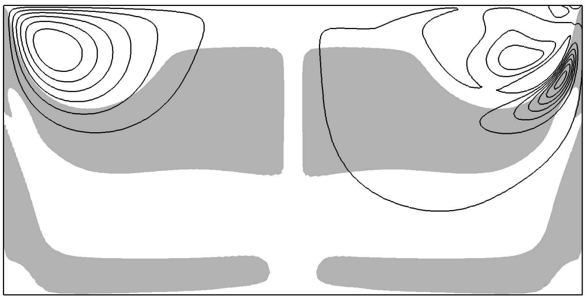

Figure 5.5: Vertical cut along the axis of the cylinder showing regions with $\Phi(\boldsymbol{r}) < 0$ as gray-shading for $\mathrm{Pr} = 0.02$, $m_c = 3$, and $\mathrm{Re} = \mathrm{Re}_c = 34,709$. Isolines indicate the basic-state stream function ψ_0 (left side) and the total local production i_v restricted to positive values (right side). The latter is shown at an azimuthal angle for which the maximum local production takes its absolute maximum.

mocapillary effect. In the low-Prandtl-number regime where heat diffusion is stronger than heat convection such a mechanism should be inertial. This hypothesis is supported by the kinetic energy balance (fig. 5.4) which shows that the kinetic energy production I_v is the dominating destabilizing process. The integral contribution of the Marangoni stresses M acts even stabilizing and it is, furthermore, vanishingly small compared to I_v.

For the inertial instability of the axisymmetric toroidal thermocapillary vortex flow in low-Prandtl-number liquid bridges Nienhüser (2002) have shown that vortex straining as well as centrifugal effects may contribute to an inertial destabilization of the basic flow (for the lid-driven cavity, see Albensoeder *et al.*, 2001). In the following we shall argue that the centrifugal mechanism is dominant for the present low-Prandtl-number instability for $\Gamma = 1$. To that end we utilize the generalized Rayleigh criterion of Bayly (1988). It states that the flow of an inviscid fluid is centrifugally unstable if a closed convex streamline exists along which the magnitude of the circulation decreases outwards. This criterion has been reformulated by Sipp & Jacquin (2000) as follows. A two-dimensional inviscid flow is centrifugally unstable if

$$\Phi(\boldsymbol{r}) := \frac{|\boldsymbol{u}_0|\Omega_0}{\mathcal{R}} < 0 \tag{5.2}$$

along a closed convex streamline. Here Ω_0 is the vorticity of the basic flow and $\mathcal{R}$ is the local radius of curvature of a streamline which can be calculated as (see Sipp & Jacquin, 2000)

$$\mathcal{R} = \frac{|\boldsymbol{u}_0|^3}{(\nabla\psi_0) \cdot (\boldsymbol{u}_0 \cdot \nabla\boldsymbol{u}_0)}. \tag{5.3}$$

Even though the criterion is valid for *inviscid* flows only, we have evaluated (5.2) for the present *viscous* basic flow. The result is shown in fig. 5.5.

The criterion (5.2) holds true in the gray-shaded areas. Most notably, the regions which would favor a centrifugal instability in an inviscid flow are aligned with the outer streamlines of the viscous toroidal vortex (left side of fig. 5.5). The region extends from the cold corner where the accelerated free-surface flow is deflected downward and along the sidewall until it separates and turns radially inward at about mid-height of the pool.

It is interesting to notice that the local production rate of kinetic energy i_v has a strong peak well within the regions in which (5.2) is satisfied (right side of fig. 5.5). Thus most of the kinetic energy of the perturbation is produced in a region that would be subject to a centrifugal-type instability if the flow were inviscid. The mechanism of self-induced vortex straining due to the bending of the vortex core that destabilizes ring vortices (Widnall & Tsai, 1977) seems to be of minor importance since the corresponding local peak of energy production near the center of the streamlines is relatively weak.

We conclude, that the low-Prandtl-number flow in a cylindrical thermocapillary pool of unit aspect ratio driven by a parabolic heat flux is unstable to a centrifugal instability. This behavior is very similar to the centrifugal instabilities in lid-driven cavities (Albensoeder *et al.*, 2001) and the Taylor–Görtler instability of the boundary layer flow along convex walls Drazin & Reid (1981).

The total local kinetic energy production rate i_v can be decomposed into $i_v = i_v^- + i_v^+$, where i_v^- and i_v^+ represent the total local production in the region where (5.2) holds and where (5.2) is not satisfied, respectively, I_v^- and I_v^+ being the corresponding integral rates. For the present case $|I_v^-| \gg |I_v^+|$ (fig. 5.4). This observation further supports the interpretation in terms of a centrifugal instability.

High-Prandtl-number instability mechanism

As a representative case for high Prandtl numbers we consider $\mathrm{Pr} = 4$. The critical wave number is $m_c = 2$ and the the critical Reynolds number is $\mathrm{Re}_c = 110,362$. The perturbation temperature on the free surface at $z = 0.5$ is shown in fig. 5.6a. It exhibits four extrema, two maxima and two minima. Since the perturbation flow is directed from the hot to the cold perturbation temperature spots, thermocapillary forces drive the perturbation flow. In fact, all other driving forces are insignificant since the total inertial energy production is vanishingly small compared to the Marangoni production $I_v \ll M$ (fig. 5.7).

The question arises of how the surface temperature extrema are created. Since the rate of diffusion of perturbation temperature (cp. equation (2.44)) is much smaller for high than for low Prandtl numbers, the surface spots could possibly be created by the vertical component of the perturbation flow which must arise due to conservation of mass (similar as in the classical Marangoni problem, see Pearson, 1958). Such a mechanism cannot hold, however, since the vertical basic state temperature gradient has the wrong sign: the free surface is hotter than the fluid below it (cf. fig. 5.1d).

The only remaining possibility is heat conduction from much stronger temperature extrema in the bulk.[2] As fig. 5.8a illustrates such extrema do exist in the bulk. The figure shows the perturbation temperature maxima in a vertical plane through the axis

[2]Theoretically the perturbation temperature θ spots at the free surface could also be created by means of convection $(\boldsymbol{u}_0 \cdot \nabla)\theta$ of the perturbation temperature field θ by the basic state flow $\boldsymbol{u}_0$. Further and more detailed analysis is necessary.

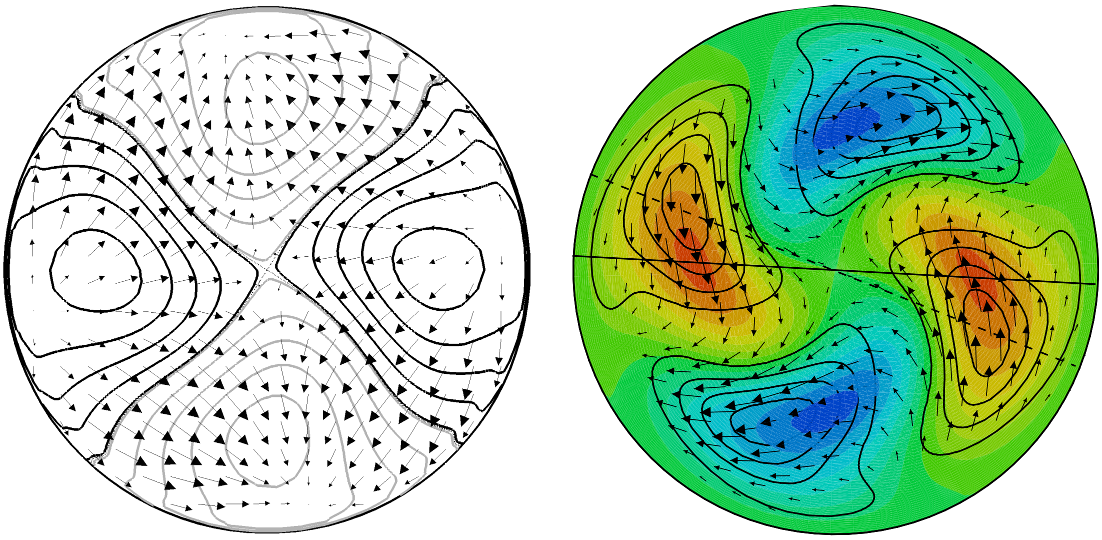

(a) (b)

Figure 5.6: (a)Perturbation flow (arrows) and perturbation temperature (isolines) on the free surface ($z = 0.5$) at critical conditions ($m_c = 2$, $\mathrm{Re}_c = 110,362$, $\omega_c = 54.54$) and for $\mathrm{Pr} = 4$ and $\Gamma = 1$. Negative values are indicated by gray lines. (b) Perturbation flow (arrows), perturbation temperature field (color), and local thermal energy production rate i_T (lines) at midplane ($z = 0$). The straight solid line indicates the cut in fig. 5.8a and the straight dashed line the cut in fig. 5.8b. The pattern rigidly rotates in clockwise direction.

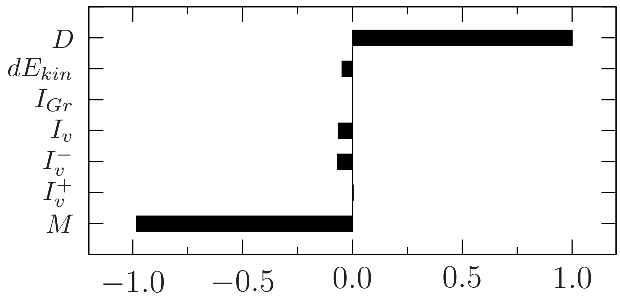

Figure 5.7: Magnitude of terms of the kinetic energy balance (2.43) for $\Gamma = 1$, $\mathrm{Pr} = 4$, and $m = 2$ at the critical Reynolds number $\mathrm{Re}_c = 110,362$.

for which the perturbation temperature takes its absolute maximum. The corresponding azimuthal angle is indicated by the solid line in fig. 5.6b.

The strong temperature extrema in the bulk are created by the thermal production. The extrema of the local thermal production rate i_T are located in close vicinity of those of the perturbation temperature (fig. 5.8b). The vertical plane through the axis of the cylinder in which the maximum energy production arises is indicated by a dashed line

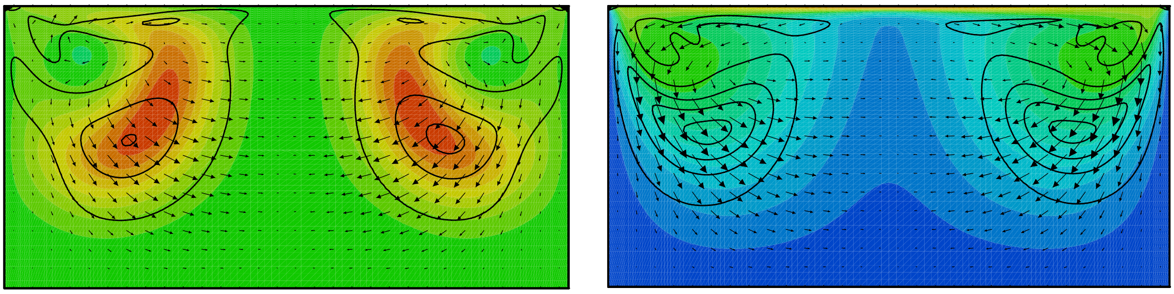

(a) (b)

Figure 5.8: (a) Perturbation velocity (arrows), perturbation temperature (color), and local thermal production i_T (lines) in a vertical plane at an azimuthal angle for which the temperature perturbation takes its absolute maximum (solid line in fig. 5.6b). (b) Perturbation flow (arrows), local thermal production i_T (lines), and basic temperature field (color) in a vertical cut at an azimuthal angle for which the maximum local thermal energy production takes its absolute maximum (dashed line in fig. 5.6b). The color scale is a range from blue to red, corresponding to a range cold to hot. The parameters are $\mathrm{Pr} = 4$, $\mathrm{Re} = \mathrm{Re}_c = 110,362$, and $m = m_c = 2$ in both cases (a,b).

in fig. 5.6b. The same mechanisms apply to the orthogonal vertical planes in which the flow direction and the temperature perturbations are reversed.

Figure 5.6b, which displays the fields in the midplane $z = 0$ as viewed from above, shows that the production extrema arise slightly ahead in clockwise direction of the temperature extrema. This is an indication for the clockwise rotation of the pattern and consistent with the negative phase velocity which, for $m > 0$ and together with (3.29) is determined by the positive critical angular frequency $\omega_c = 54.54$ for the case presented. Of course, the critical modes arise as pairs with $\omega = \pm\omega_c$.

The above mechanisms are essentially the same as for hydrothermal waves in plane thermocapillary layers (Smith & Davis, 1983) or in thermocapillary liquid bridges (Wanschura *et al.*, 1995*b*). We thus conclude the the instability at high Prandtl numbers is due to hydrothermal waves.

Prandtl-number dependence of the energy budget for $\Gamma = 1$

The dependence of the kinetic energy budget on Pr for the standard configuration is shown in figure 5.9. The full range of computed Prandtl numbers can be separated into a low- ($\mathrm{Pr} \lesssim 1$) and a high-Prandtl-number range ($\mathrm{Pr} \gtrsim 1$).

The low-Prandtl-number range can be further subdivided at $\mathrm{Pr} \approx 0.04$. For $\mathrm{Pr} \lesssim 0.04$ the kinetic energy budget is entirely dominated by the inertial production term I_v. For the intermediate Prandtl numbers $\mathrm{Pr} \gtrsim 0.04$ we find an increasing influence of the Marangoni term M, while the overall budget is still dominated by I_v. The absolute

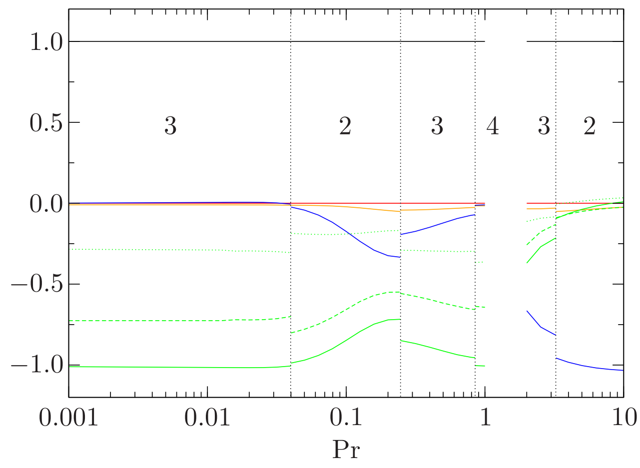

Figure 5.9: Components of the kinetic-energy balance (2.43) for unit aspect ratio $\Gamma = 1$ as functions of the Prandtl number in the range $10^{-3} \leq \mathrm{Pr} \leq 10$. The critical wave number m_c is provided by the black numbers. The components displayed are the dissipation D —, buoyant production I_{Gr} —, inertial production I_v —, its decomposition I_v^- ---- and I_v^+ ···, Marangoni production M —, and the total kinetic energy production rate $\partial_t E_{kin}$ —.

value of the contribution by the Marangoni term reaches a maximum for $\mathrm{Pr} \approx 0.246$ and decreases to a vanishingly small value for higher values of Prandtl number.

In the high-Prandtl-number range Marangoni production M increasingly strongly with the Prandtl number. While there is still a sizable amount of kinetic energy produced by inertial processes (I_v) in the range of $\mathrm{Pr} \approx 2$, its contribution decreases rapidly for higher Prandtl numbers.

5.1.2 Aspect-ratio dependence in the limit of asymptotically small Prandtl numbers

In the limit of small Prandtl numbers $\mathrm{Pr} \to 0$ temperature transport is conductive and the dynamics are solely inertial. The basic state temperature field merely serves to drive the basic flow. For practical reasons[3] we have studied the behavior for $\mathrm{Pr} = 10^{-10}$. This value is an excellent approximation of the zero-Prandtl-number limit if the Reynolds number satisfies $\mathrm{Re} \ll 10^{10}$ which is certainly the case for the parameters considered. In the following we focus on the aspect-ratio dependence of the two-dimensional flow and its stability.

Basic flow

To discuss the basic flow we consider the basic-state stream function ψ_0 at the critical Reynolds number for the aspect-ratio range $\Gamma \in [0.5, 6.1]$. The stream function is displayed in figure 5.10a-i for selected aspect ratios.

[3]Note that in the numerical implementation a Prandtl number $\mathrm{Pr} \to 0$ reduces the temperature equation to $\nabla^2\Theta = 0$, and the advection term $\mathrm{Pr}(\boldsymbol{U} \cdot \nabla)\Theta$ drops out.

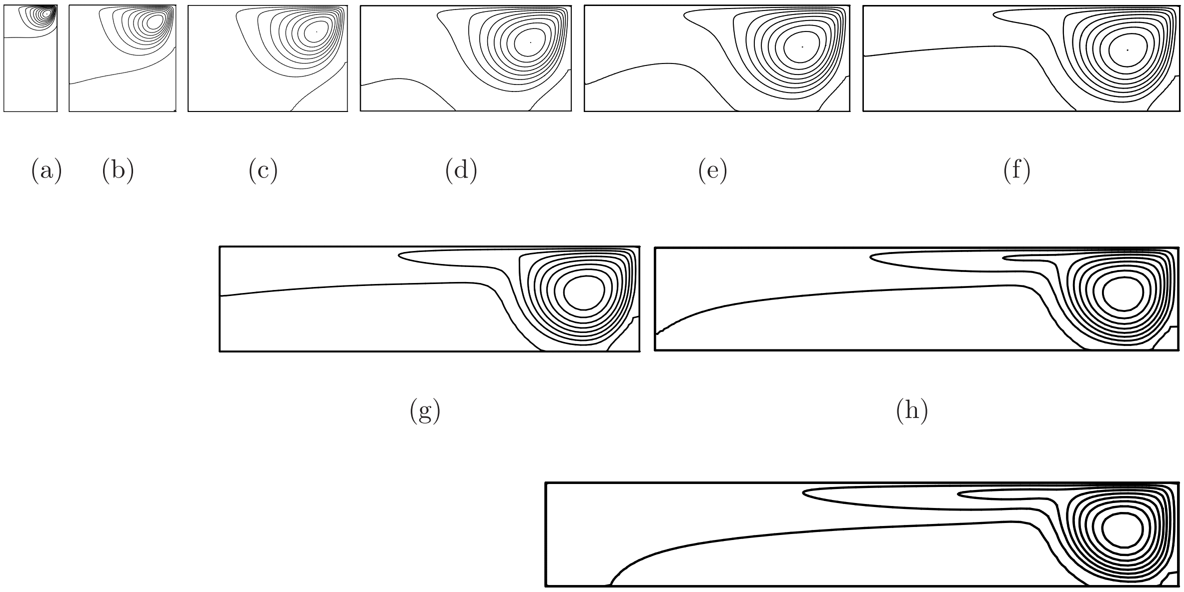

(a) (b) (c) (d) (e) (f) (g) (h) (i)

Figure 5.10: Basic state stream function ψ_0 of the critical mode for Prandtl number $\mathrm{Pr} = 10^{-10}$. Note that only the negative values of the basic state stream function are provided. The plots feature (a) $\Gamma = 0.5$, $m_c = 3$, $\mathrm{Re} = \mathrm{Re}_c = 114,705$, (b) $\Gamma = 1$, $m_c = 3$, $\mathrm{Re} = \mathrm{Re}_c = 29,084$, (c) $\Gamma = 1.5$, $m_c = 3$, $\mathrm{Re} = \mathrm{Re}_c = 20,206$, (d) $\Gamma = 2$, $m_c = 7$, $\mathrm{Re} = \mathrm{Re}_c = 33,389$, (e) $\Gamma = 2.5$, $m_c = 7$, $\mathrm{Re} = \mathrm{Re}_c = 35,375$, (f) $\Gamma = 3$, $m_c = 7$, $\mathrm{Re} = \mathrm{Re}_c = 65,958$, (g) $\Gamma = 4$, $m_c = 3$, $\mathrm{Re} = \mathrm{Re}_c = 120,635$, (h) $\Gamma = 5.1$, $m_c = 5$, $\mathrm{Re} = \mathrm{Re}_c = 142,872$, and (i) $\Gamma = 6.1$, $m_c = 7$, $\mathrm{Re} = \mathrm{Re}_c = 170,343$.

Since the driving radial gradient of the surface temperature vanishes at the axis and attains its maximum at the cold side wall, the flow is primarily driven near the outer cold wall. For deep cavities $\Gamma \ll 1$ the ring vortex has a diameter slightly less than $2R$. As a result the flow does not significantly penetrate in axial direction. At the small aspect ratio $\Gamma = 0.5$ the primary toroidal vortex has a vertical extension of about one third of the cavity height. The toroidal vortex in the upper portion of the cavity drives a slow counter-rotating secondary vortex[4]. In the limit $\Gamma \to 0$ a sequence of counter-rotating weak viscous vortices is expected from theoretical assumptions in the lower parts of the cavity[5]. The behavior of the sequence of viscous vortices is similar as for rectangular geometry (Rybicki & Floryan, 1987). In the limit $\Gamma \to 0$ one expects an asymptotic structure of the vortices and an exponential decay of their strengths.

[4]Note that the secondary vorticies are a few orders of magnitude weaker than the primary vortex. The isolines of ψ_0 of the secondary vorticies are therefore omitted in figure 5.10a-i. Only the $\psi_0 = 0$ isoline is plotted to mark the location of the counter-rotating vorticies.

[5]Note however that these vorticies could not be observed in the numerical results. This is most likely due to the limited resolution of the grid

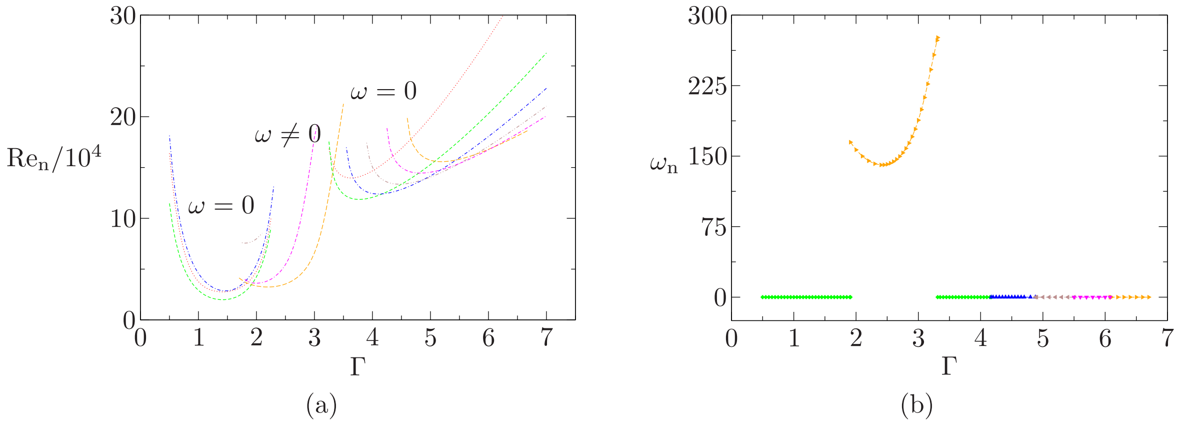

Figure 5.11: Aspect ratio dependence of the (a) neutral Reynolds numbers $\mathrm{Re_n}$ (b) frequencies ω_n in the limit asymtotically small Prandtl number for parameters $\mathrm{Bd} = 0$ and $\mathrm{Pr} = 10^{-10}$. - The neutral wave number $m = m_\mathrm{n}$ are $m = 1$:—, $m = 2$:· · ·, $m = 3$:- - - -, $m = 4$:·-·-·-, $m = 5$:·-··-·, $m = 6$:-·- -·, and $m = 7$:— — —.

Increasing the aspect ratio to $\Gamma = 1$ the size of the weak separated vortex in the lower part of the cavity shrinks and will even be further reduced, at $\Gamma = 1.5$, to a toroidal corner vortex confined to the outer corner at the bottom of the domain. As the aspect ratio grows further, the primary vortex collides with the bottom wall. As a result, an additional separated flow region arises at the bottom wall near the axis of the cylinder ($\Gamma = 2$). Now the diameter of the primary vortex is no longer determined by the radial extent over which the surface temperature varies, but rather by the height of the cylinder. For even larger aspect ratios the thermocapillary vortex is confined to the cold wall and there exists a wider radial range along the free surface over which the flow is driven. The situation now is similar to the case of a shallow rectangular thermocapillary cavity as considered by Ben Hadid & Roux (1990). Therefore, we can expect a sequence of thermocapillary vortices staggered radially. For the present Reynolds numbers, apparent only a single primary vortex exist (see e.g. fig. 5.10i for $\Gamma = 6.1$). The major interior part of the cavity is governed by a thermocapillary-driven entrance flow. Different from Ben Hadid & Roux (1990) and in addition to the cylindrical geometry, however, the driving force depends on the radial coordinate through the conducting temperature field. For the present parameters the large and weak secondary vortex at the bottom of the pool grows in size with Γ until the primary vortex reattaches to the bottom of the pool near the axis when the aspect ratio is in the range $5.1 \leq \Gamma \leq 6.1$. Note, however, that we always consider the flow at the critical Reynolds number $\mathrm{Re} = \mathrm{Re}_c$.

Aspect-ratio dependence of the stability boundary

Figure 5.11a shows the neutral stability curves (neutral Reynolds numbers $\mathrm{Re_n}$) for wave numbers $m = 3, 4, 5, 6$, and 7 over the aspect-ratio range $\Gamma \in [0.5, 7]$[6]. The corresponding neutral frequencies ω_n are displayed in figure 5.11b[7].

Three ranges can be distinguished: for low aspect ratio $\Gamma \lesssim 1.91$ we find a stationary critical mode with a wave number $m_c = 3$. The mechanism of this instability is the same as for aspect ratio $\Gamma = 1$ and low Prandtl numbers $\mathrm{Pr} \lesssim 1$ discussed in sec. 5.1.1, i.e., primarily centrifugal effects are destabilizing the basic flow. In the intermediate aspect-ratio range $1.91 \lesssim \Gamma \lesssim 3.31$ a qualitatively different type of instability occurs. The different nature is obvious, since the critical mode with wave number $m_c = 7$ is time-dependent. In yet another aspect-ratio range $\Gamma \gtrsim 3.31$ we find a further type of instability. The perturbation flow is again stationary. Furthermore, the critical mode in this large-aspect-ratio range the critical wave number increases with aspect ratio.

Instability mechanisms in the intermediate-aspect-ratio-range $1.91 \lesssim \Gamma \lesssim 3.31$

Figure 5.12a shows the perturbation flow $\boldsymbol{u}$ and the temperature field θ at the free surface ($z = 0.5$) for $\Gamma = 2$ and $\mathrm{Pr} = 10^{-10}$. The critical Reynolds number is $\mathrm{Re}_c = 33,389$ for $m_c = 7$. The perturbation temperature field exhibits 7 minima and maxima which are extended in radial direction. The critical mode is oscillatory and it rotates about the axis in clockwise direction with angular frequency $\omega_c = 156.70$. Since the azimuthal component of the surface flow is essentially directed from the cold to the hot surface temperature spots (compare fig. 5.12b) the perturbation flow cannot be driven by thermocapillary stresses (the same argument was used in section 5.1.1). This is confirmed by the small Marangoni number $\mathrm{Ma}_c = \mathrm{PrRe}_c = 3.34 \times 10^{-6}$. Figure 5.13 shows that this is indeed the case. The Marangoni production M is negligible. Most of the kinetic energy is produced by the inertial term I_v, in particular by I_v^-.

Evaluating the criterion (5.2) we obtain the grey-shaded area of figure 5.14. It is seen that the region which favors a centrifugal instability for inviscid flow is aligned with the outer streamlines of the toroidal basic flow vortex. Similar as in fig. 5.5 the region extends from the cold corner along the outer wall to the separation point of the basic flow from where it continues somewhat further radially inward. The total local inertial energy production rate i_v is significantly peaked in that region and near the separation point (compare fig. 5.15). Since most of the kinetic energy is produced in this region, conclude that the instability is centrifugal in nature.

Note that in a central region close to the axis the perturbation flow and temperature fields are very small. Since the perturbation mode is driven by an instability of the basic state vortex flow it seems but logical that the perturbation mode will be locally very weak near the axis where the basic state flow is weak too. - In other words we have a travelling wave on the basic state vortex fed by a centrifugal effect.

[6]Note that the individual data points in fig. 5.11 have been omitted due to the high resolution of the graph. - $\Delta\Gamma = 0.05$ for two consecutive data points.

[7]Note that the abscissa has been shifted in order to make the data points with $\omega_n = 0$ visible.

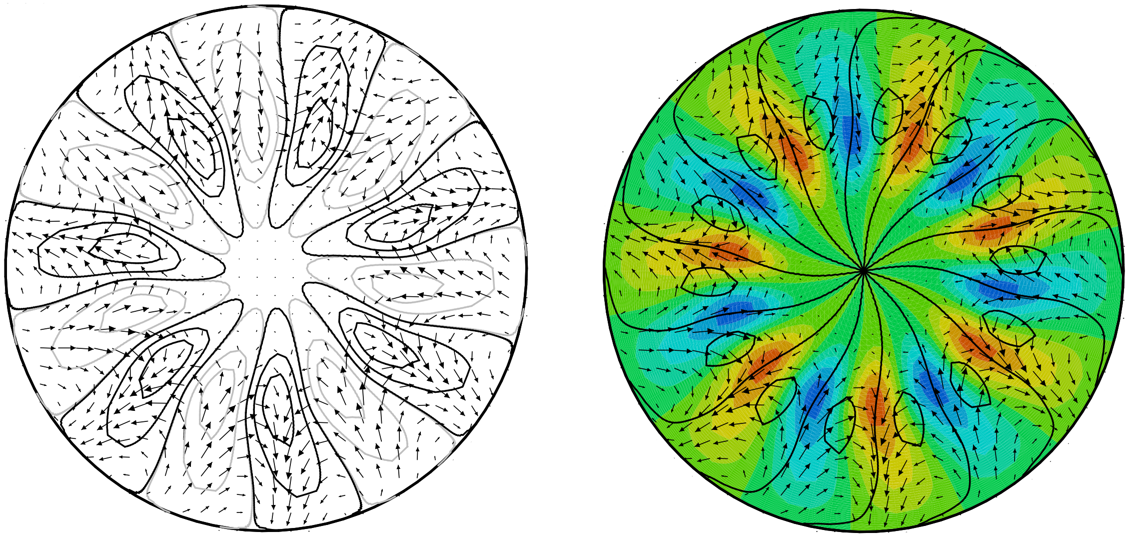

(a) (b)

Figure 5.12: Critical flow fields on the free surface $z = 0.5$ for $\Gamma = 2$, $\mathrm{Pr} = 10^{-10}$, and $m = 7$ at $\mathrm{Re}_c = 33,389$. (a) Perturbation flow (arrows) and perturbation temperature field (lines). Negative values are indicated by gray lines. (b) Azimuthal velocity (lines) and perturbation temperature (contours). Note that the $v = 0$ isolines pass through the center of the pool. The closed isolines represent the extrema of the azimuthal perturbation velocity, the sign of the extrema can be easily seen from the direction of the perturbation flow (arrows). The pattern rigidly propagates in clockwise direction.

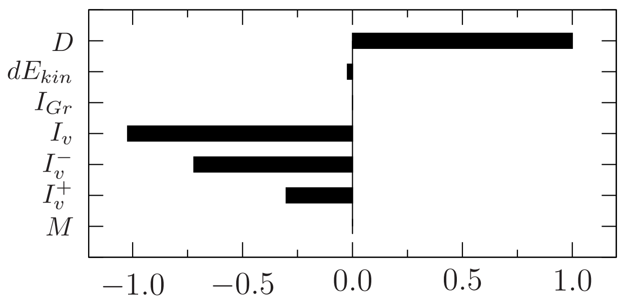

Figure 5.13: Terms of the kinetic energy balance (2.43) for parameters $\Gamma = 2$, $\mathrm{Pr} = 10^{-10}$ and $m = 7$ at critical Reynolds number $\mathrm{Re}_c = 33,389$.

Instability mechanisms in the high-aspect-ratio-range $\Gamma \gtrsim 3.31$

For aspect ratios $\Gamma \gtrsim 3.31$ a stationary critical mode arises. As a representative case we select $\Gamma = 4.5$ and Prandtl number 10^{-10}. The critical Reynolds number is $\mathrm{Re}_c = 128,487$ with $m_c = 4$. The perturbation flow $\boldsymbol{u}$ and temperature field θ at the free

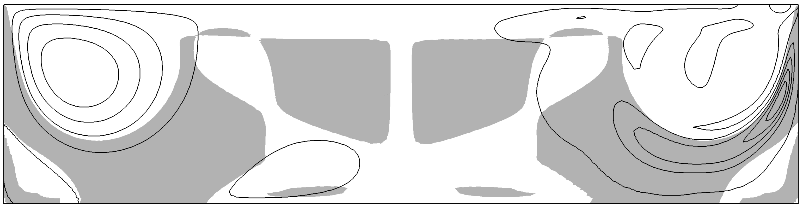

Figure 5.14: Vertical cut along the axis of the cylinder showing the isolines of the basic-state stream function ψ_0 (left side), the isolines of the total local kinetic-energy-production rate i_v (integrand of I_v) restricted to positive values (right side) and the regions for which $\Phi(\boldsymbol{r}) < 0$ holds (gray-shading). The cut is shown at an azimuthal angle for which the maximum local kinetic energy production rate takes its absolute maximum. The parameters are $\mathrm{Pr} = 10^{-10}$, $\Gamma = 2$, $m_c = 7$, and $\mathrm{Re}_c = 33,389$. Note that i_v has twice the azimuthal period of the critical mode.

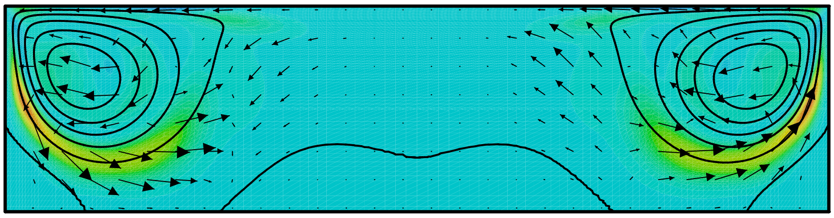

Figure 5.15: Vertical cut along the axis of the cylinder showing the perturbation flow (arrows, interpolated from the numerical data), the total local kinetic-energy-production rate i_v (integrand of I_v), and the basic-state stream function ψ_0 (lines). The cut is shown at an azimuthal angle for which the maximum local kinetic energy production rate takes its absolute maximum. The parameters are $\mathrm{Pr} = 10^{-10}$, $\Gamma = 2$, $m_c = 37$, and $\mathrm{Re}_c = 33,389$.

surface is shown in fig. 5.16. The perturbation temperature field exhibits 4 minima and 4 maxima. Apart from a small zone near the periphery the surface flow $\boldsymbol{u}$ is nearly perfectly aligned in radial direction. It is inward in the region of the cold spot and outward in the hot-spot region. The very weak azimuthal flow near $r = R$ is directed from the hot to the cold perturbation temperature spots.

It's quite clear that the mode cannot be excited by Marangoni stresses (see fig. 5.17). As for all asymptotically small Prandtl number cases the kinetic energy balance is dominated by I_v, in particular I_v^-.

Figure 5.18 displays the region in which the criterium (5.2) holds. Like in the foregoing centrifugal instability it arises in the same region of the basic state, in particular along the outer streamlines of the toroidal vortex which exists at the outer periphery of the cavity. Figure 5.18 displays a small area on the inner side of the vortex in which energy is produced and might be attributed to a centrifugal effect. An additional contribution to the kinetic energy growth comes from a region near the axis and in the upper half of the cavity. In this area the peak of i_v is located and $\Phi < 0$ (indicated by the grey shading). Note that since the basic state velocities are relatively small in this area the

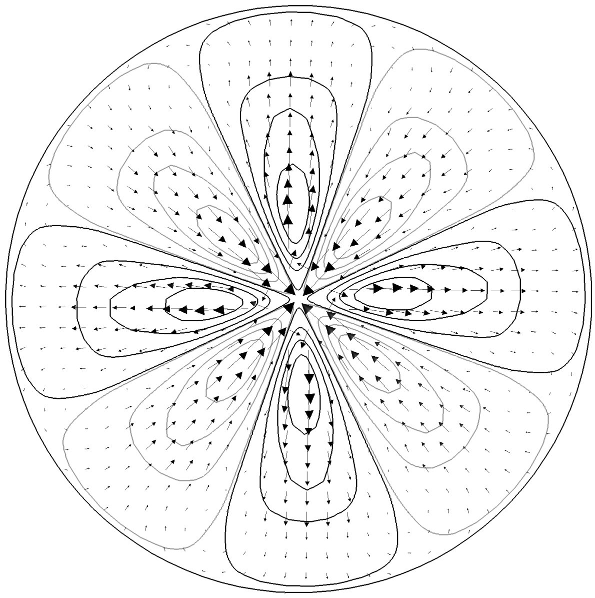

Figure 5.16: Perturbation flow (arrows) and perturbation temperature field (lines) on the free surface for $z = 0.5$ and $\mathrm{Pr} = 10^{-10}$. Negative values are indicated by gray lines. The parameters are $\Gamma = 4.5$, $m_c = 4$ and $\mathrm{Re}_c = 128,487$.

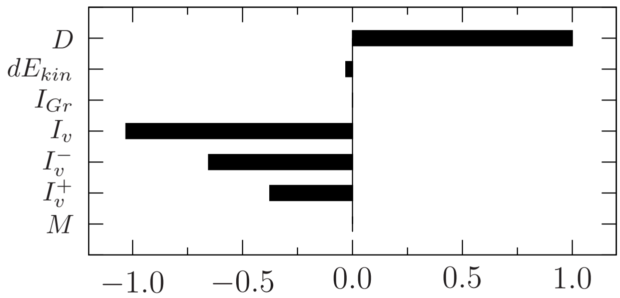

Figure 5.17: Terms of the kinetic energy balance (2.43) for parameters $\Gamma = 4.5$, $\mathrm{Pr} = 10^{-10}$ and $m = 4$ at critical Reynolds number $\mathrm{Re}_c = 128,487$.

contributions need to be explained by a process other than a centrifugal mechanism.

A more detailed picture is obtained by considering the individual terms i_{v1} to i_{v5}[8] In the vertical cut displayed in figure 5.19 most of the kinetic energy transfer[9] due to i_{v1} takes place close to the axis of the pool, with its minima located in a surface layer, and the maxima in a more extended subsurface layer. The converging basic state flow $\boldsymbol{u}_0$ decelerates as it approaches the axis in the surface layer. Here the local minima

[8]Note that the integrand of the total inertial energy transfer can be written as $i_v = \sum_{i=1}^{5} i_{vi}$. We are henceforth interested in the individual contributions.

[9]Figure 5.19 displays the total inertial kinetic energy transfer i_v. To give the reader an idea where the individual terms i_{vi} are most pronounced the approximate location of their maxima and minima are indicated.

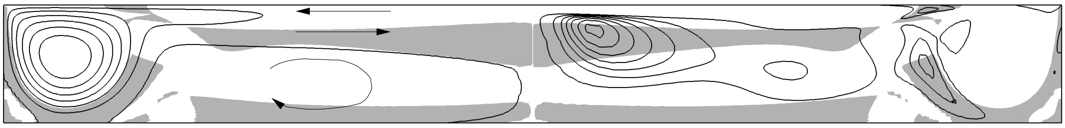

Figure 5.18: Vertical cut along the axis of the cylinder showing the isolines of the basic-state stream function ψ_0 (left side), the isolines of the total local kinetic-energy-production rate i_v (integrand of I_v) restricted to positive values (right side) and the regions for which $\Phi(\boldsymbol{r}) < 0$ holds (gray-shading). The cut is shown at an azimuthal angle for which the maximum local kinetic energy production rate takes its absolute maximum. The parameters are $\mathrm{Pr} = 10^{-10}$, $\Gamma = 4.5$, $m_c = 4$, and $\mathrm{Re}_c = 128,487$. The arrows indicate the direction of the basic state flow field.

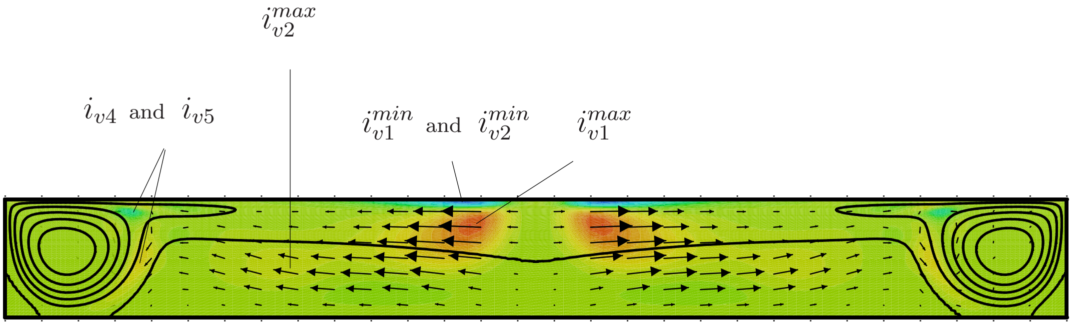

Figure 5.19: Vertical cut along the axis of the cylinder showing the perturbation flow (arrows), the total local kinetic-energy-production rate i_v (integrand of I_v) (color), and the basic-state stream function ψ_0 (lines). The cut is shown at an azimuthal angle for which the maximum local kinetic energy production rate takes its absolute maximum. The parameters are $\mathrm{Pr} = 10^{-10}$, $\Gamma = 4.5$, $m_c = 4$, and $\mathrm{Re}_c = 128,487$.

of i_{v1} is located. The diverging outward basic state flow accelerates in the subsurface layer, here the local maxima of i_{v1} can be found. In both locations the local inertial production term i_{v1} drives a outward directed perturbation flow $\boldsymbol{u}$. The local minima of i_{v2} is located in the deceleration region of the basic state vortex flow $\boldsymbol{u}_0$ in a surface layer close to the axis where we have already found the minima of i_{v1}. The local maxima of i_{v2} is found in the separated flow region at the bottom of the pool in a region shifted slightly from the centre of counter-rotating basic state vortex towards the axis, creating a radially outward directed perturbation flow $\boldsymbol{u}$. The influence of i_{v3} is to weak to yield a significant contribution to the driving of the perturbation flow. The inertial production by i_{v4} and i_{v5} is located in the outer streamlines of the upflow region of the primary vortex, cp figure 5.19. Their minima and maxima are interchanged and nearly cancel each other out so that the residual inertial production drives only a comparably weak local perturbation flow $\boldsymbol{u}$.

Note that due to periodicity of the perturbation mode ($m_c = 4$) the local maxima/minima of inertial production rates i_{vi} are interchanged with a periodicity of $\pi/4$, and the corresponding radial perturbation flow $\boldsymbol{u}$ is reversed with the same periodicity.

We therefore conclude that the instability is primarily a property of the turning flow[10] near the the axis: In a surface (subsurface) layer decelerating fluid is approaching the axis nearly radially. In a turning zone this converging surface (subsurface) flow diverges radially outward in a subsurface (surface) layer below (atop) of the converging surface (subsurface) flow.

It is interesting to note that a similar instability occurs in solutocapillary driven thin layers when small amounts of solute are added concentrically at the free surface which reduce the surface tension. The flow structure near the axis is qualitatively similar (Pshenichnikov & Yatsenko, 1974). The type of instability has been analyzed by Shtern & Hussain (1993) (compare Shtern & Hussain (1999)) who considered the stability of two-dimensional similarity solutions in a half space. This type of flow (solutal-driven) was originally discovered by Thomson (1855) and similar (solutal) experiments have been made by Pshenichnikov & Yatsenko (1974) (figures in Shtern & Hussain (1993)). For the instability of this type of flow he coined the term *diverging instability*. In the absence of any detailed energetic analysis of the diverging instability it is tempting to speculate that the present instability is of the same origin.[11] At least, the deceleration effect of the radial surface flow contributed a significant amount to the energy growth of the most unstable mode.

5.1.3 Aspect-ratio dependence of the flow and its stability for Pr $= 0.03$

So far we have considered the aspect-ratio dependence of the standard configuration in the limit of asymptotically small Prandtl numbers. We now turn to realistic Prandtl numbers of liquid metals and semi-conductors. As a typical Prandtl number we consider $\mathrm{Pr} = 0.03$ - the Prandtl number of liquid silicon close to its melting-temperature T_m. In the same range of Prandtl number we find: liquid gallium ($\mathrm{Pr} = 0.02$), mercury ($\mathrm{Pr} = 0.025$), and germanium ($\mathrm{Pr} = 0.006$). We start the discussion of the aspect-ratio dependence of the basic state flow and continue with the stability curve and the change it is subject to with respect to the stability curve for Prandtl number $\mathrm{Pr} = 10^{-10}$.

Basic state

The basic state near the critical onset for $\mathrm{Pr} = 0.03$ is very similar to that for $\mathrm{Pr} = 10^{-10}$. Differences arise mainly in the structure of the separated zone near the bottom. Compare the basic state stream function ψ_0 for aspect ratio $\Gamma = 2$ in figures 5.10d ($\mathrm{Pr} = 10^{-10}$) and 5.20a ($\mathrm{Pr} = 0.03$). In sec. 5.1.2 we saw that in the range of aspect ratios $\Gamma = 1.5$ to 2 the primary vortex collides with the bottom wall and a separated flow region forms at the bottom stretching from the axis outwards. For $\mathrm{Pr} = 0.03$ the primary vortex collides with the bottom in the same range of aspect ratio, yet the separated flow region is smaller in extent and confined to a region in the middle between the axis of the pool and the

[10] Respectively the acceleration and deceleration of the basic state flow $\boldsymbol{u}_0$ in a region close to the axis.
[11] Further analysis is necessary.

Figure 5.20: Basic state stream function ψ of the critical mode for parameters Prandtl number $\mathrm{Pr} = 0.03$, Bond number $\mathrm{Bd} = 0$. Note that only the negative values of the basic state stream function are provided. The plots feature (a) $\Gamma = 2$, $m_c = 3$, $\mathrm{Re} = \mathrm{Re}_c = 28,449$, (b) $\Gamma = 6.1$, $m_c = 6$, $\mathrm{Re} = \mathrm{Re}_c = 45,124$.

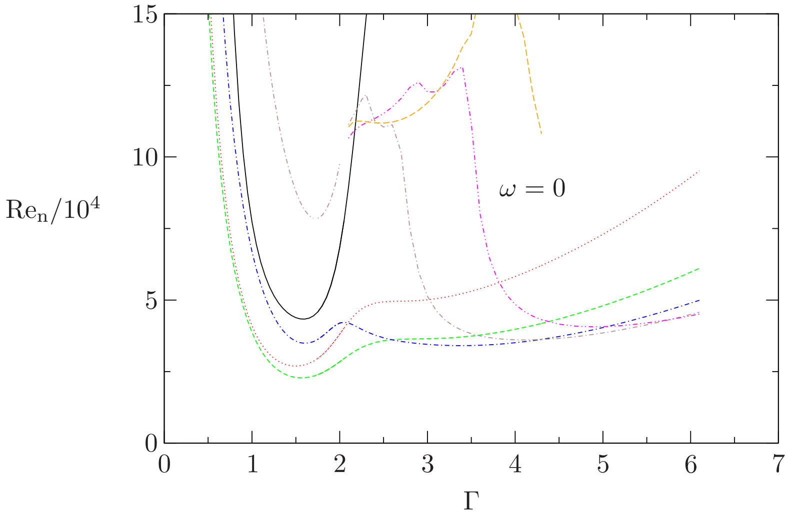

Figure 5.21: Aspect ratio dependence of neutral Reynolds numbers $\mathrm{Re_n}$ in the small-Prandtl-number-range for $\mathrm{Pr} = 0.03$. - The wave numbers are $m = 1$:—, $m = 2$:· · ·, $m = 3$:- - - -, $m = 4$:·-·-·-, $m = 5$:-··-··-, $m = 6$:-·-·-·, and $m = 7$:— — —.

primary vortex. For higher values of aspect ratio ($\Gamma = 6.1$) the differences are even more obvious, compare figures 5.10i ($\mathrm{Pr} = 10^{-10}$) and 5.20b ($\mathrm{Pr} = 0.03$). The separated flow extending from the primary vortex inwards almost towards the axis for $\mathrm{Pr} = 10^{-10}$ is confined to comparably small region close to the primary vortex for $\mathrm{Pr} = 0.03$. At the same time the outer streamlines of the primary vortex penetrate deeper into the pool and slightly further towards the axis. Note that the differences in the basic state flow field are connected to the increased (weak) convective effect of the temperature field, which are due to the increase in Prandtl number showing up in the temperature equation (2.5b) and hence resulting in a higher coupling of momentum and temperature equation by means of the thermocapillary free surface boundary condition (2.24).

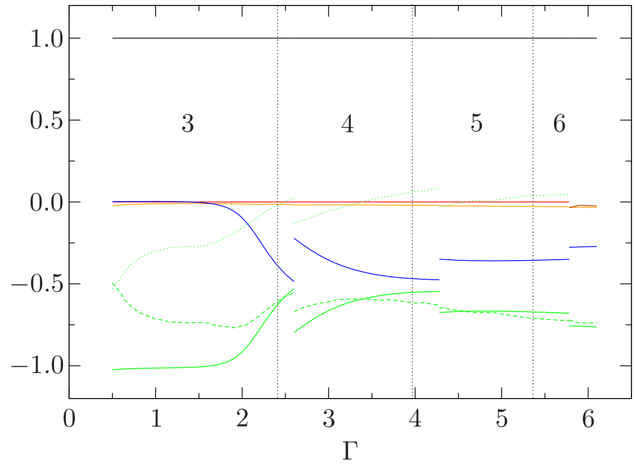

Figure 5.22: Components of the kinetic energy balance according to (2.43) for Prandtl number Pr $= 0.03$. The critical wave number m_c is given by the black numbers in the diagram. The components are dissipation D —, Grashof term I_{Gr} —, inertial energy production I_v —, and its decomposition I_v^- - - - - and I_v^+ · · ·, Marangoni terms M —, and $\partial_t E_{kin}$ —.

Aspect-ratio dependence of the stability boundary

The aspect ratio dependence of the neutral stability curves is shown in figure 5.21 for Prandtl number Pr $= 0.03$ and aspect ratios $\Gamma = 0.5$ to 6.1. In the limit of asymptotically small Prandtl number (Pr $= 10^{-10}$) three distinct regions could be identified: an oscillatory aspect-ratio-range and two stationary ranges. For Pr $= 0.03$ the critical mode is always stationary, neither an oscillatory nor a stationary high-aspect-ratio-range can be found.

Figure 5.21 shows that the critical Reynolds number decreases for small aspect ratio $\Gamma \lesssim 1.55$. For these small aspect ratios (deep cavities) the basic vortex does not depend much on the depth d.

When the aspect ratio approaches $\Gamma \approx 1.55$ Marangoni forces start to yield a destabilizing contribution while the inertial mechanisms become less effective such that the critical Reynolds number increases and the basic state flow is slightly stabilized. This trend continues as the aspect ration is further increased. The critical wave number also increases with Γ.

Figure 5.22 shows that the Marangoni driving which is important for intermediate aspect ratios becomes less important for aspect ratios beyond $\Gamma \approx 4$. Hence, inertial mechanisms are most dominant for deep ($\Gamma \lesssim 1.55$) and shallow ($\Gamma \gtrsim 4$) pools. Moreover, the production takes place essentially in the region where (5.2) holds. This is indicated by the fact that the total inertial production is approximately equal to the magnitude of I_v^- while I_v^+ turns slightly positive (stabilizing). We conclude that the instability mechanism is dominantly centrifugal with a significant destabilizing contribution due to Marangoni forces in the range $\Gamma \gtrsim 1.55$ to 6.1.

To completet the picture the perturbation flow $\boldsymbol{u}$ and temperature θ at the free surface displayed in fig. 5.23 for aspect ratios $\Gamma = 0.5$ to 6.1 and $z = 0.5$ need to be

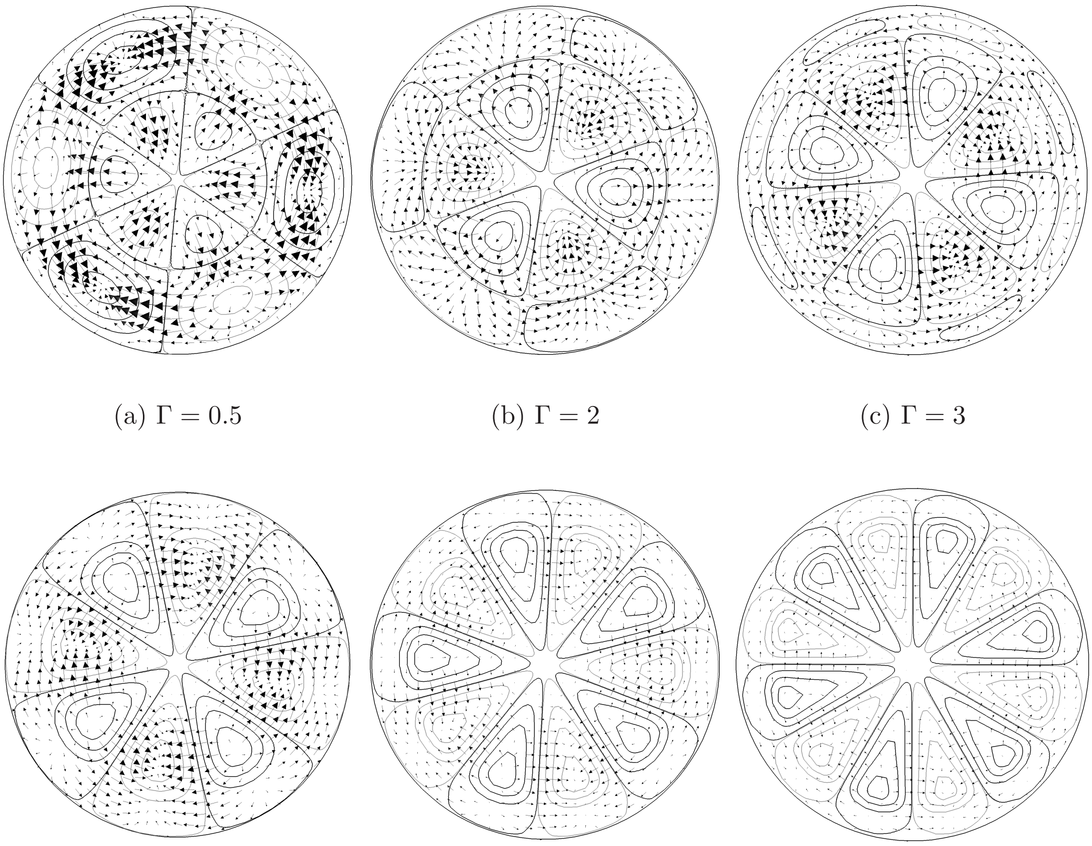

(a) $\Gamma = 0.5$ (b) $\Gamma = 2$ (c) $\Gamma = 3$

(d) $\Gamma = 4$ (e) $\Gamma = 5.1$ (f) $\Gamma = 6.1$

Figure 5.23: Perturbation flow (arrows, interpolated from the numerical data) and perturbation temperature field (lines) on the free surface for $z = 0.5$ and $\mathrm{Pr} = 0.03$. Negative values are indicated by gray lines. The parameters are (a) $\Gamma = 0.5$, $m_c = 3$ and $\mathrm{Re}_c = 155,210$, (b) $\Gamma = 2$, $m_c = 3$ and $\mathrm{Re}_c = 28,449$, (c) $\Gamma = 3$, $m_c = 4$ and $\mathrm{Re}_c = 34,514$, (d) $\Gamma = 4$, $m_c = 4$ and $\mathrm{Re}_c = 35,097$, (e) $\Gamma = 5.1$, $m_c = 5$ and $\mathrm{Re}_c = 38,994$, (f) $\Gamma = 6.1$, $m_c = 6$ and $\mathrm{Re}_c = 45,125$.

explained. For $\Gamma = 0.5$ the free-surface-perturbation flow looks similar to the one discussed in sec. 5.1.1. Noteworthy, the flow between the strong peripheral cold and hot spots is opposing the Marangoni forces. Upon an increase of Γ the inner free-surface-perturbation-temperature extrema increase in size and strength relative to the outer extrema, until the latter completely vanish between $\Gamma = 3$ and 4. The surface flow from the remaining (previously inner and weak) perturbation temperature spots behaves like a Marangoni flow, connecting the temperature extrema by a flow from the hot to the cold extrema. The free surface flow weakens with a further increase of aspect ratio.

The internal structure of the basic state flow field u_0 in a vertical plane is shown in fig. 5.20. One can observe that the minimum of the basic state stream function ψ_0^{min}

of the primary vortex is shifted downwards with increasing aspect ratio. In-between $\Gamma = 3$ and $\Gamma = 4$ the downward movement of ψ_0^{min} halts[12]. Note that it is exactly this range in which the weak outer temperature extrema disappear and the free surface perturbation flow shows a pattern attributed to a Marangoni flow. This behaviour can be explained if one considers that the centrifugal instability is an instability of the primary basic state vortex. The perturbation flow is due to this instability and hence coupled to and fed by the primary basic state vortex. Hence if the primary vortex shifts downwards so does the perturbation flow. Now if the perturbation flow fed by the instability of the primary basic state vortex shifts downwards its contribution to the free surface flow becomes weaker and the free-surface-pertubation flow due to Marangoni forces becomes more important[13]. Basic state temperature transport is dominated by conductive temperature transport convective effects are weak. The basic temperature field θ_0 serves only to drive the basic flow $\boldsymbol{u}_0$.

5.1.4 Aspect ratio dependence of the flow and its stability for high Prandtl number Pr $= 4$

Another relevant range of Prandtl numbers is $\mathrm{Pr} > 1$ which applies to transparent liquid used in model experiments, like ethanol ($\mathrm{Pr} \approx 17$), silicone oil ($\mathrm{Pr} \gtrsim 10$), or molten sodium nitrate ($\mathrm{Pr} \approx 7$).

Aspect-ratio dependence of the basic state for high Prandtl numbers

The basic stream function ψ_0 and temperature fields θ_0 for $\mathrm{Pr} = 4$ and aspect ratios in the range of $\Gamma = 0.5$ to 6.1 are shown in figs. 5.24 and 5.25. The strong convective effect on the temperature field is obvious, and can be understood along the lines of the discussion of the high Prandtl number basic state presented in sec. 5.1.1.

The basic state flow field for high Prandtl numbers is characterized by the following features: The influence of the primary clockwise rotating vortex on the basic state temperature field is more pronounced in the high Prandtl number case[14]. The outer secondary vortex is small and its relative size decreases even further with increasing aspect ratio. Furthermore, no inner secondary vortex can be found. The primary vortex is deformed yet in contrast to low Prandtl number basic states ($\mathrm{Pr} \lesssim 1$) this deformation is featured by all the streamlines of the primary basic state vortex (compare fig. 5.24) and not only by the outer streamlines (compare figs. 5.10 and 5.20). Selected plots of the basic state temperature field θ_0 are presented in figure 5.25. The basic state temperature field is convected by the basic flow and in turn the basic flow field modified via the Marangoni effect.

[12] ψ_0^{min} has reached its lowest position $z = z_{min}$.

[13] One could also argue that the Marangoni flow at the free surface becomes more visible, since it is less disturbed by the perturbation flow driven by the centrifugal instability mechanism.

[14] In accordance with equation (2.22b) the temperature transport in a stationary basic state flow can be described by $\mathrm{Pr}(\boldsymbol{u}_0 \cdot \nabla\theta_0) = \nabla^2\theta_0$. Hence convective transport dominates the flow for $\mathrm{Pr} \to \infty$, while conductive transport plays only a minor role.

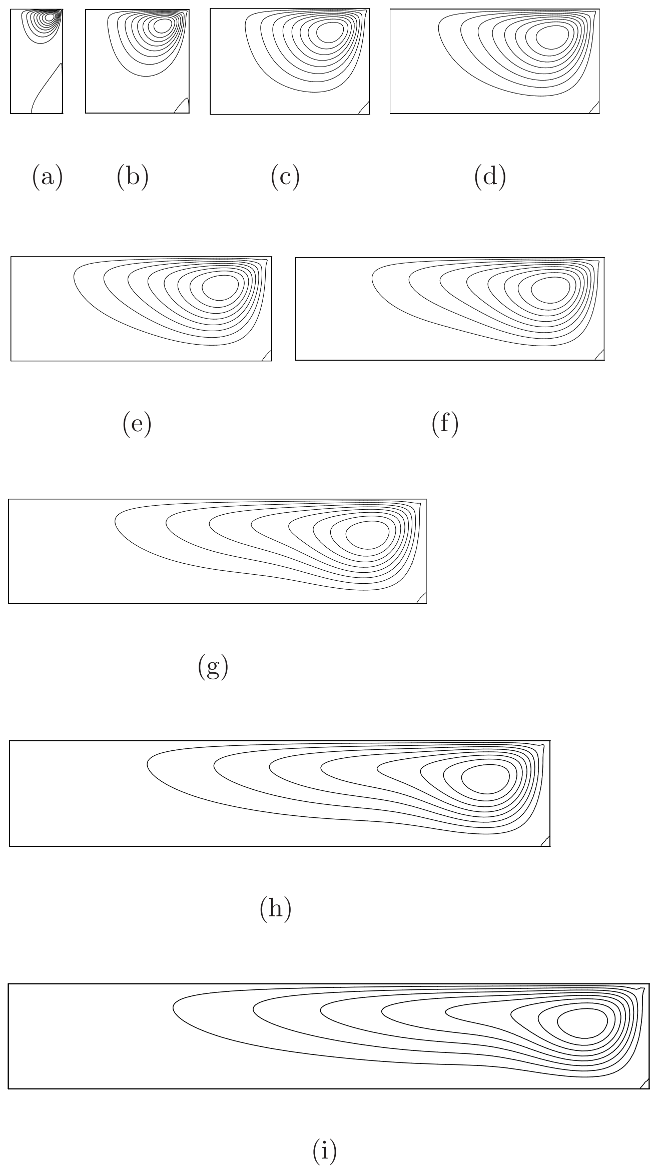

Figure 5.24: Basic state stream function ψ_0 of the critical mode for parameters: Prandtl number $\mathrm{Pr} = 4$ and Bond number $\mathrm{Bd} = 0$. Note that only the negative values of the basic state stream function are provided. The plots feature (a) $\Gamma = 0.5$, $m_c = 2$, $\mathrm{Re} = \mathrm{Re}_c = 471,760$, (b) $\Gamma = 1$, $m_c = 2$, $\mathrm{Re} = \mathrm{Re}_c = 110,363$, (c) $\Gamma = 1.5$, $m_c = 3$, $\mathrm{Re} = \mathrm{Re}_c = 54,033$, (d) $\Gamma = 2$, $m_c = 3$, $\mathrm{Re} = \mathrm{Re}_c = 46,486$, (e) $\Gamma = 2.5$, $m_c = 4$, $\mathrm{Re} = \mathrm{Re}_c = 50,808$, (f) $\Gamma = 3$, $m_c = 4$, $\mathrm{Re} = \mathrm{Re}_c = 59,882$, (g) $\Gamma = 4$, $m_c = 5$, $\mathrm{Re} = \mathrm{Re}_c = 83,481$, (h) $\Gamma = 5.1$, $m_c = 5$, $\mathrm{Re} = \mathrm{Re}_c = 104,180$, and (i) $\Gamma = 6.1$, $m_c = 6$, $\mathrm{Re} = \mathrm{Re}_c = 129,494$.

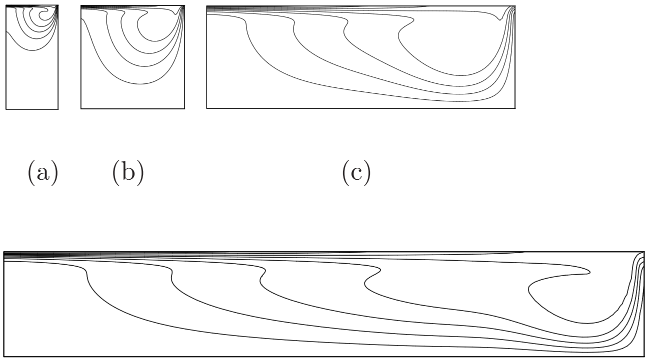

(a) (b) (c)

(d)

Figure 5.25: Basic state temperature field θ_0 of the critical mode for parameters Prandtl number Pr $= 4$. The plots feature (a) $\Gamma = 0.5$, $m_c = 2$, $\mathrm{Re} = \mathrm{Re}_c = 471,760$, (b) $\Gamma = 1$, $m_c = 2$, $\mathrm{Re} = \mathrm{Re}_c = 110,363$, (c) $\Gamma = 3$, $m_c = 4$, $\mathrm{Re} = \mathrm{Re}_c = 59,882$, and (d) $\Gamma = 6.1$, $m_c = 6$, $\mathrm{Re} = \mathrm{Re}_c = 129,494$.

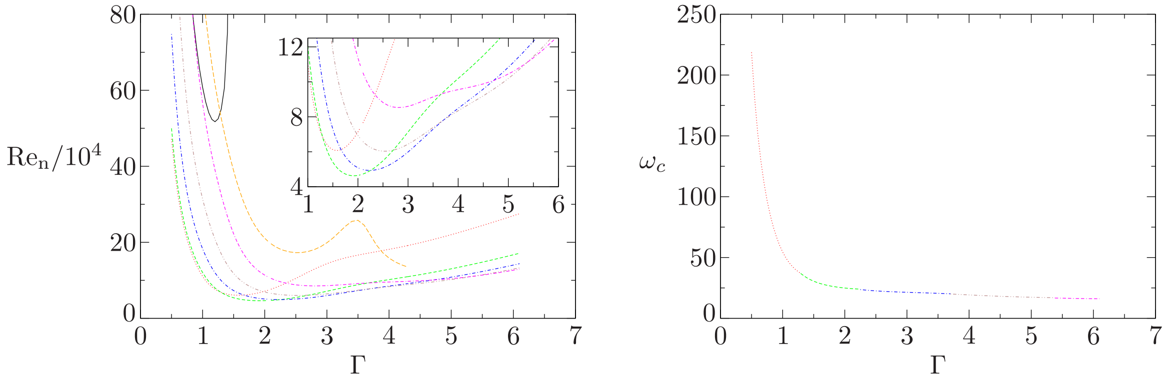

(a) (b)

Figure 5.26: Aspect ratio dependence of the (a) neutral Reynolds numbers $\mathrm{Re_n}$ (b) neutral frequencies ω_n in the high-Prandtl-number-range for Pr $= 4$. - The neutral wave number $m = m_\mathrm{n}$ are $m = 1$:—, $m = 2$:· · ·, $m = 3$:- - - -, $m = 4$:-·-·-, $m = 5$:-·-·-, $m = 6$:-·-·-, and $m = 7$:− − −.

Aspect ratio dependence of the stability boundary

Figure 5.26a displays the neutral Reynolds number curves for aspect ratios from $\Gamma = 0.5$ to 6.1 and for the moderately high Prandtl number Pr $= 4$. In order to better visualize the intersections of the neutral curves the vertical Reynolds-number axis is stretched in the inset. The critical mode is oscillatory for all aspect ratios and wave numbers. The critical frequencies $\omega_c(\Gamma)$ are displayed in figure 5.26b.

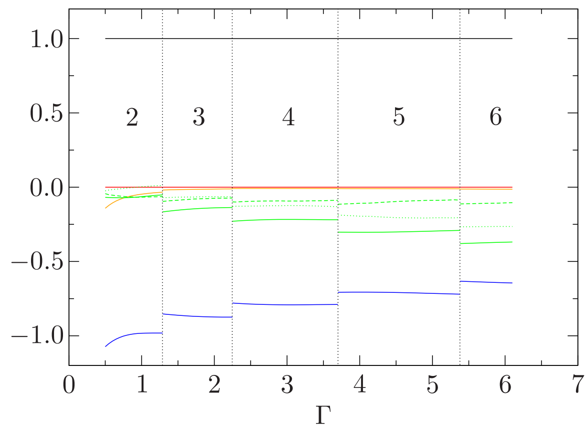

Figure 5.27: Components of the kinetic energy balance according to (2.43) for Prandtl number Pr = 4. The critical wave number m_c is given by the black numbers in the graph. The components are dissipation D —, Grashof term I_{Gr} —, inertial energy production I_v —, and its decomposition I_v^- - - - - and I_v^+ · · ·, Marangoni terms M —, and $\partial_t E_{kin}$ —.

As discussed in section 5.1.1 the instability is basically caused by a hydrothermal-wave mechanism. Note however that the impact of the inertial terms increases with aspect ratio. The aspect-ratio dependence of the kinetic energy balance (2.43) is shown in fig. 5.27. For all computed aspect ratios Marangoni forces yield the dominant contribution to the destabilization of the basic flow. Inertial terms also act destabilizing, yet to much smaller extent. The relative contributions of the inertial to the Marangoni production terms remain almost constant for a given critical wave number m_c. As the aspect ratio increases, and with it the critical wave number, the balance is shifted in favor of the inertial terms. If this tendency is extrapolated the instability might possibly be dominated by inertial production for sufficiently high aspect ratios.

5.1.5 The effect of gravity

To study the effect of gravitational acceleration on the linear stability of the flow we use the dynamic Bond number Bd defined in (2.26) to measure the importance of buoyancy. We shall consider the effect of the dynamic Bond number on the flow and stability for a liquid pool with unit aspect ratio ($\Gamma = 1$) and an asymptotically small ($\mathrm{Pr} = 10^{-10}$) and a high Prandtl number ($\mathrm{Pr} = 10$).

Basic thermocapillary-buoyant flow

Figure 5.28 shows a sequence of stream-function isolines for increasing dynamic Bond numbers. Buoyancy forces directed downward in the vicinity of the cold sidewall cause an increase in size of the primary clockwise rotating vortex. The separation from the cold sidewall is delayed and even completely suppressed for sufficiently high Bd. For $\mathrm{Pr} \ll 1$ there is hardly any coupling of the temperature field to the flow. Hence, the temperature field is almost conducting as in fig. 5.1c for $\mathrm{Bd} = 0$.

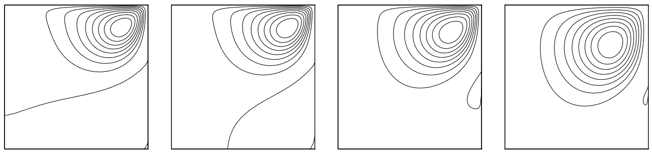

(a) (b) (c) (d)

Figure 5.28: Basic state stream function ψ of the critical mode for parameters Prandtl number $\mathrm{Pr} = 10^{-10}$, aspect ratio $\Gamma = 1$. Note that only the negative values of the basic state stream function are provided. The plots feature (a) $\mathrm{Bd} = 0.1$, $m_c = 3$, $\mathrm{Re} = \mathrm{Re}_c = 29,011$, (b) $\mathrm{Bd} = 1$, $m_c = 3$, $\mathrm{Re} = \mathrm{Re}_c = 28,435$, (c) $\mathrm{Bd} = 6.31$, $m_c = 3$, $\mathrm{Re} = \mathrm{Re}_c = 27,905$, and (d) $\mathrm{Bd} = 794$, $m_c = 2$, $\mathrm{Re} = \mathrm{Re}_c = 1,505$.

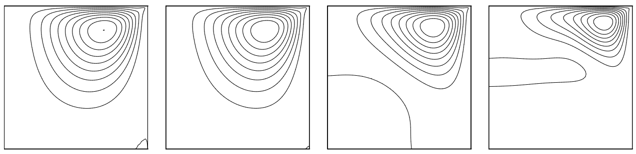

(a) (b) (c) (d)

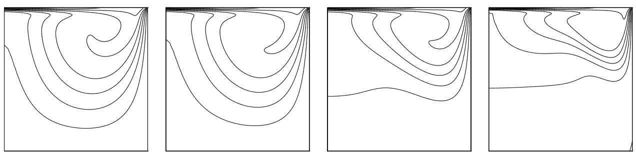

(e) (f) (g) (h)

Figure 5.29: Basic state stream function ψ and temperature field θ_0 of the critical mode for parameters Prandtl number $\mathrm{Pr} = 10$, aspect ratio $\Gamma = 1$. Note that only the negative values of the basic state stream function are provided. Plots (a)-(d) show the basic state streamfunction and (e)-(h) the basic state temperature field. The parameters are (a), (e) $\mathrm{Bd} = 0.1$, $m_c = 2$, $\mathrm{Re} = \mathrm{Re}_c = 56,872$, (b), (f) $\mathrm{Bd} = 1$, $m_c = 2$, $\mathrm{Re} = \mathrm{Re}_c = 59,722$, (c), (g) $\mathrm{Bd} = 6.31$, $m_c = 2$, $\mathrm{Re} = \mathrm{Re}_c = 87,640$, and (d), (h) $\mathrm{Bd} = 12.58$, $m_c = 1$, $\mathrm{Re} = \mathrm{Re}_c = 280,951$.

For the moderately high Prandtl number $\mathrm{Pr} = 10$ the effect of buoyancy is more intricate. Generally, increasing buoyancy promotes the formation of thermal stratification. This tendency is clearly visible and has also been observed in an annular geometry by Schwabe (2002) and according to Kuhlmann (2008) also in rectangular cavities. Owing

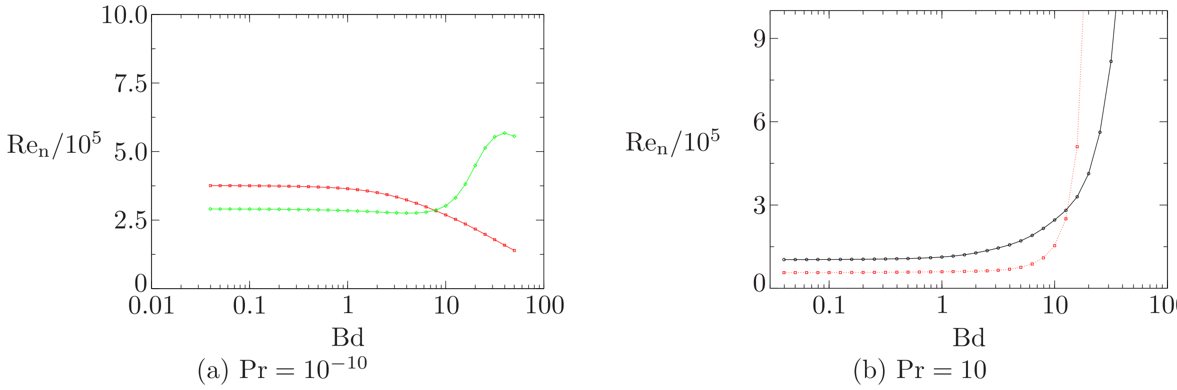

Figure 5.30: Dynamic Bond number dependence of the neutral Reynolds number $\mathrm{Re_n}$ of the most important neutral modes for parameters: aspect ratio $\Gamma = 1$ and Prandtl numbers (a) $\mathrm{Pr} = 10^{-10}$ and (b) $\mathrm{Pr} = 10$. - - ●: $m = 1$, ■: $m = 2$, and ♦: $m = 3$.

to the low thermal diffusivity hot surface fluid turns downward near the cold sidewall, but cannot penetrate deep into the pool owing to upward buoyancy forces. The radial return flow continues to rise towards the top. This leads to a flattening of the vortex which is more pronounced near the cold sidewall resulting in a rounded triangular shape of the stream lines. Within the nearly stagnant lower part of the pool a weak counter-rotating ring vortex can arise as the remains of the larger separation zone in the lower half of the pool.

Impact of buoyancy on the linear stability boundary

Figures 5.30a (5.31a) and 5.30b (5.31b) show the dynamic Bond number (Grashof number) dependence of the most important neutral modes for aspect ratio $\Gamma = 1$ and Prandtl number $\mathrm{Pr} = 10^{-10}$ and $\mathrm{Pr} = 10$, respectively. The neutral frequencies ω_n for $\mathrm{Pr} = 10$ are displayed in fig. 5.32. Note that the basic flow is stabilized by buoyancy forces for high Prandtl number $\mathrm{Pr} = 10$, while it is destabilized in the limit of asymtotically small Prandtl number $\mathrm{Pr} = 10^{-10}$. The corresponding kinetic energy balances (2.43) are shown in figures 5.33a and 5.33b. Since $\mathrm{Bd} = \mathrm{Gr}/\mathrm{Re}$ we get a clearer picture of the stability boundary if we discuss its Grashof number dependence instead of its Bond number dependence.

For asymptotically small Prandtl number ($\mathrm{Pr} = 10^{-10}$, fig. 5.31a) and $\mathrm{Gr} \lesssim 2.2 \times 10^5$ the flow is unstable to a stationary perturbation mode with wave number $m_c = 3$. This range can be again subdivided in two ranges for $\mathrm{Gr} \lesssim 10^5$ and $\mathrm{Gr} \gtrsim 10^5$. For $\mathrm{Gr} \lesssim 10^5$ the flow is destabilized as Gr increases, while it is stabilized for $\mathrm{Gr} \gtrsim 10^5$. With the selection of a stationary critical mode ($m_c = 2$) for $\mathrm{Gr} \gtrsim 2.2 \times 10^5$ buoyancy forces increasingly destabilize the flow, and the stability curve approaches a limiting value $\mathrm{Gr}_c \approx 1.25 \times 10^6$ for $\mathrm{Re} \to 0$. In this limiting case the basic flow is driven by buoy-

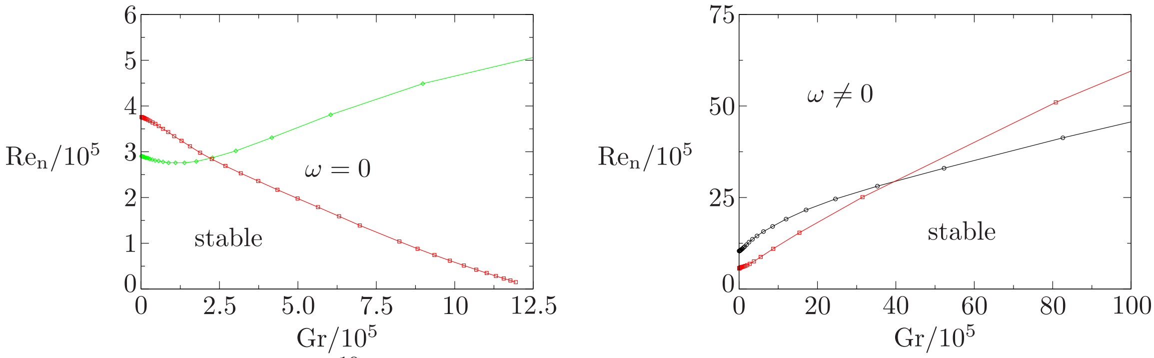

(a) Pr = 10^{-10} (b) Pr = 10

Figure 5.31: Grashof number dependence of the neutral Reynolds number $\mathrm{Re_n}$ of the most important neutral modes for parameters: aspect ratio $\Gamma = 1$ and Prandtl numbers (a) $\mathrm{Pr} = 10^{-10}$ and (b) $\mathrm{Pr} = 10$. - - ●: $m = 1$, ■: $m = 2$, and ♦: $m = 3$.

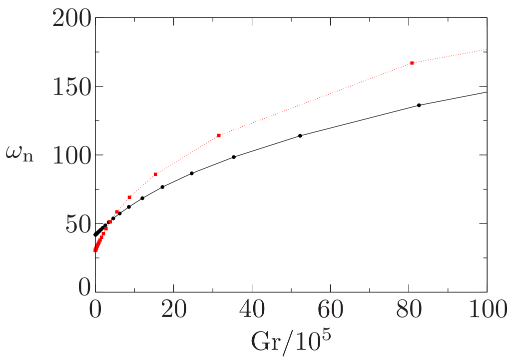

Figure 5.32: Grashof number dependence of the neutral frequency ω_n of the most important neutral modes for parameters: aspect ratio $\Gamma = 1$ and Prandtl number $\mathrm{Pr} = 10$. - - ●: $m = 1$ and ■: $m = 2$.

ancy forces only. The value has been linearly interpolated from the trend of the critical stability curve in figure 5.31a. Figure 5.33a shows that I_v^- is the most important term contributing to the instability of the flow, hence the instability is inertial.

For high Prandtl number ($\mathrm{Pr} = 10$, fig. 5.31b) the Grashof number range can be separated into a range unstable to a $m_c = 2$ oscillatory perturbation mode and a range for $\mathrm{Gr} \gtrsim 4 \times 10^6$ with a linear instability to a $m_c = 1$ oscillatory perturbation mode. In both ranges the axisymmetric flow is clearly stabilized by an increase in Gr, according to Kuhlmann (2008) the stabilization is due to increasing thermal stratification. The importance of the contribution of the buoyancy term to the stability of the basic state flow is displayed in the corresponding kinetic energy balance given in figure 5.33b.

For $\mathrm{Gr} \lesssim 4 \times 10^6$ the relative contribution of the Marangoni forces to the overall kinetic energy balance decreases simultaneously with the stabilization of the basic flow while

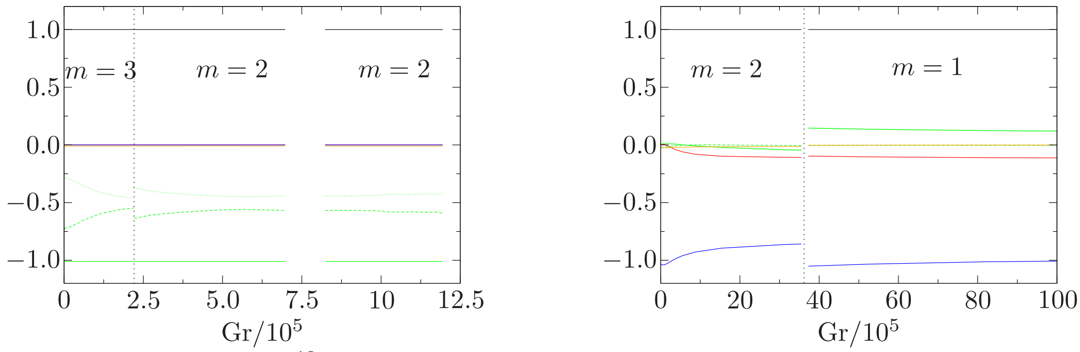

(a) $\mathrm{Pr} = 10^{-10}$ (b) $\mathrm{Pr} = 10$

Figure 5.33: Components of the kinetic energy balance according to (2.43) versus the Grashof number Gr for Prandtl number $\mathrm{Pr} = 10^{-10}$ and $\mathrm{Pr} = 10$. The critical wave number m_c is given by the black numbers in the diagram. The components are dissipation D —, Grashof term I_{Gr} —, inertial energy production I_v —, and its decomposition I_v^- - - - -and I_v^+ · · ·, Marangoni terms M —, and $\partial_t E_{kin}$ —.

the contribution of the buoyancy forces increases. With the selection of the $m_c = 1$-mode for $\mathrm{Gr} \gtrsim 4 \times 10^6$ the trend towards a further stabilization of the basic flow with increasing Grashof number continues. Yet at the same time we find a significant change in the kinetic energy balance, while the trend found for the destabilizing contributions of thbuoyancycy and Marangoni forces continues, the contribution of the inertial terms changes sign. Hence the inertial production terms act stabilizing for $\mathrm{Gr} \gtrsim 4 \times 10^6$. This sudden change in sign of the inertial production terms is compensated for by a shift of the relative contribution of the Marangoni forces.

Note that an increase in the relative stabilizing/destabilizing contribution of the buoyancy term, does not account for a stabilization/destabilization of the basic state flow. It describes a change in the relative contributions of various forces to the kinetic energy budget.

5.2 Results on the annular pool problem

Prior to the computation of the solutions to the annular pool problem some modifications of the geometry and the boundary conditions presented for the liquid-pool model in sections 2 and 3 are necessary. A detailed account on these modifications is presented in appendix A[15].

In sec. 5.2.1 some remarks on the comparability of the computed results to experimental data provided by Kamotani *et al.* (1992) are addressed, and the necessary information for a comparison is given. A discussion of the basic state flow follows in sec. 5.2.2. In sec. 5.2.3 the critical stability boundaries for the annular pool flow are presented and compared to prior experimental data. Finally, a sound explanation of the underlying physical instability mechanism is given in sec. 5.2.4.

5.2.1 Comparison with the conditions of previous investigations

Experiments for the annular system heated from the inside have been carried out by several investigators. For a comparison we shall focus on the experimental results of Kamotani *et al.* (1992). In the ground-based experiments, which are described in detail in Kamotani *et al.* (1992) and Kamotani *et al.* (2000), using Dow Corning silicone oil of 2 cSt with $\mathrm{Pr} = 27$ at 25°C the free surface was found to be almost flat in the full experimental range. Moreover, according to the numerical computations cited in Kamotani *et al.* (2000) the total heat loss from the free surface by radiation and forced convection has been less than 5% of the total heat transfer rate, and can hence be neglected[16]. The Teflon bottom provides a good thermal insulation and the outer wall from copper and cooled at a constant ambient temperature of $\mathsf{T}_0 = 25°\mathrm{C}$ guarantees a good approximation of the constant temperature conditions. The inner wall was a temperature controlled heating rod. Hence, the boundary conditions presented in appendix A should be a good approximation of the experimental conditions.

A certain problem is posed by the Boussinesq approximation, since the experimental temperature variations have been as large as $\Delta\mathsf{T} \approx 50°\mathrm{C}$ which causes corresponding variations of the material parameters[17]. To determine constant approximations to the material parameters we interpolated tabulated data (Obermeier-GmbH, 2007; Wacker-Silikonöle-AK, 2001) by taking their values at the average temperature $\bar{\mathsf{T}} = \mathsf{T}_0 + \Delta\mathsf{T}/2$. Another error source is of course the experimental uncertainty of the temperature measurement for which Kamotani *et al.* (1992) specify a relative error of 5%. An error of 5% is an upper bound for our numerical computations as well (see section 4). In order to estimate the variability of the results we use the Gaussian error σ_f of a dependent function f which depends on a set of variables $\boldsymbol{x}$ which is defined as

[15] The passionate reader is well advised to read it now!

[16] According to Sim & Zebib (2002) the free surface heat loss must not be neglected. Still it is neglected in the context of the present work since its scope is on the comparison and validation of the results presented by Kamotani *et al.* (1992)

[17] Note that the Boussinesq approximation we assume that $\Delta\mathsf{T} \ll \mathsf{T}_0$. Compare also sec. 2.1.1

Table 5.1: Summary of the experimental setup.

	Kamotani *et al.* (1992) (exp.)
geometry	cylindrical $\eta = R_i/R$, $\mathrm{Ar} = \Gamma^{-1}$
free surface	almost adiabatic & flat
side walls	heating rod, copper wall
bottom	Teflon
fluid	2 cSt silicone oil at 25°C

the root of the sum of the squared individual errors σ_{x_j}

$$\sigma_f = \sqrt{\sum_{j=1}^{M} \left(\frac{\partial f(\boldsymbol{x})}{\partial x_j} \sigma_{x_j} \right)^2} \quad . \tag{5.4}$$

For instance with $f = \mathrm{Re}_c$ and $\boldsymbol{x}^{\mathrm{T}} = (\Delta \mathsf{T}_c, \gamma, d, \nu, \rho)$ we compute the possible variation of the critical Reynolds number Re_c for the onset of three-dimensional flow. In the absence of any information on the error of the input data we assume $\sigma_{x_j} = 0.05 x_j$, i.e. a relative error of 5 %[18].

To extract the dynamic Bond number Bd from the experimental data we have calculated the static Bond number $\mathrm{Bo} = \rho g d^2/\sigma_0$ with the help of the geometrical information given in Kamotani *et al.* (1992) and our knowledge of the material data. We obtain the dynamic Bond number from

$$\mathrm{Bd} = \frac{\sigma_0 \beta}{\gamma} \mathrm{Bo} \quad . \tag{5.5}$$

For future reference we note that the aspect ratio $\mathrm{Ar} = d/R = \Gamma^{-1}$ which has been used by, e.g. Kamotani *et al.* (1992), is the inverse of the aspect ratio Γ defined in the present investigation. For an overview, we provide a brief summary of the different approaches/setups in tables 5.1 and 5.2.

Numerical computations for the non-perturbed steady axisymmetric flow have been performed by Kamotani et al., compare Kamotani *et al.* (1992) for a detailed reference. Their computations are performed on a non-uniform grid with a resolution of 46×41 points ($N_r \times N_z$) with a code based on a SIMPLER algorithm of Patankar (1980). In terms of the numerical model they assume a flat non-deformable, adiabatic free surface, solid walls at constant temperature T_0, a heater temperature $\mathsf{T}_1 = \mathsf{T}_0 + \Delta \mathsf{T}$, and a fluid with a temperature dependent kinematic viscosity ν. Besides that they give no information. A short summary of their numerical conditions can be found in table 5.2.

[18] The computational error of the critial Reynolds number Re_c is difficult to estimate. In sec. 4 we found that the critical Reynolds number computed for the half-zone model by means of the present numerical code deviates from prior results by about 4.1 %. Assuming a computational error of the same order $\approx 5\%$ for the annular pool model seems reasonable, in particular since the critical Reynolds numbers are of the same order of magnitude.

Table 5.2: Summary of the different numerical approaches/setups.

	this work	Kamotani *et al.* (1992) (num.)
geometry	cylindrical $\eta = R_i/R$, $\Gamma = R/d$	cylindrical $\eta = R_i/R$, $\mathrm{Ar} = \Gamma^{-1}$
free surface	adiabatic & flat	adiabatic & flat
side walls	constant temperature	constant temperature
bottom	adiabatic	has not been specified
fluid	Boussinesq fluid	variable viscosity model

Note that the overall agreement with the results of Kamotani *et al.* (1992) (their figure 2) is very good. Some deviations can be found in temperature field θ_0 for aspect ratio $\Gamma = 0.5$. While the thermal boundary layer in figure 2 of Kamotani *et al.* (1992) is quite thin in the lower half of the cylinder despite of the slow motion there, it is much thicker in the present case (figure 5.34d). These deviations might possibly be explained by the differences of the numerical model. Kamotani *et al.* (1992) used a variable viscosity model. Therefore, the viscosity is likely to be smaller near the heating rod and thus giving rise to somewhat thinner boundary layers.

5.2.2 Axisymmetric basic state flow

The temperature difference $\Delta\mathsf{T}$ between the heater and the outer wall causes a non-uniform distribution of temperature at the free surface (fig. 5.34b,d) and, in turn, a non-uniform distribution of surface tension. The thermocapillary effect drives a radial fluid motion from the heater to the outer wall. At the wall a return flow below the free surface is formed. A toroidal vortex develops. Examples are provided in fig. 5.34. The rotation of the vortex is clockwise, i.e. the basic state streamfunction has a minimum $\psi_0 < 0$ at the vortex center. The corresponding isotherms exhibit boundary layers on the surface of the heater and on the top free surface due to the high Marangoni number $\mathrm{Ma} = \mathrm{RePr}$ which is 37,800 and 783,000 for fig. 5.34a,b and 5.34c,d, respectively.

5.2.3 Stability boundaries under normal gravity

The basic two-dimensional flow exists for all Reynolds numbers. However, it may become unstable at a critical Reynolds number Re_c. In a first step we consider the flow stability for $\mathrm{Pr} = 27$ and a heater radius ratio $\eta = 0.079$. These parameters correspond to the ones used in the experiments of Kamotani *et al.* (1992). The dynamic Bond number is obtained using (5.5).

Within the aspect ratio range $\Gamma \in [0.513, 1.613]$, corresponding to $\mathrm{Ar} \in [0.62, 1.95]$ we find that modes with wave numbers $m = 2$, 3, or 4 can be critical. The neutral stability curves are given in fig. 5.35. A list of the critical parameters is given in table 5.3.

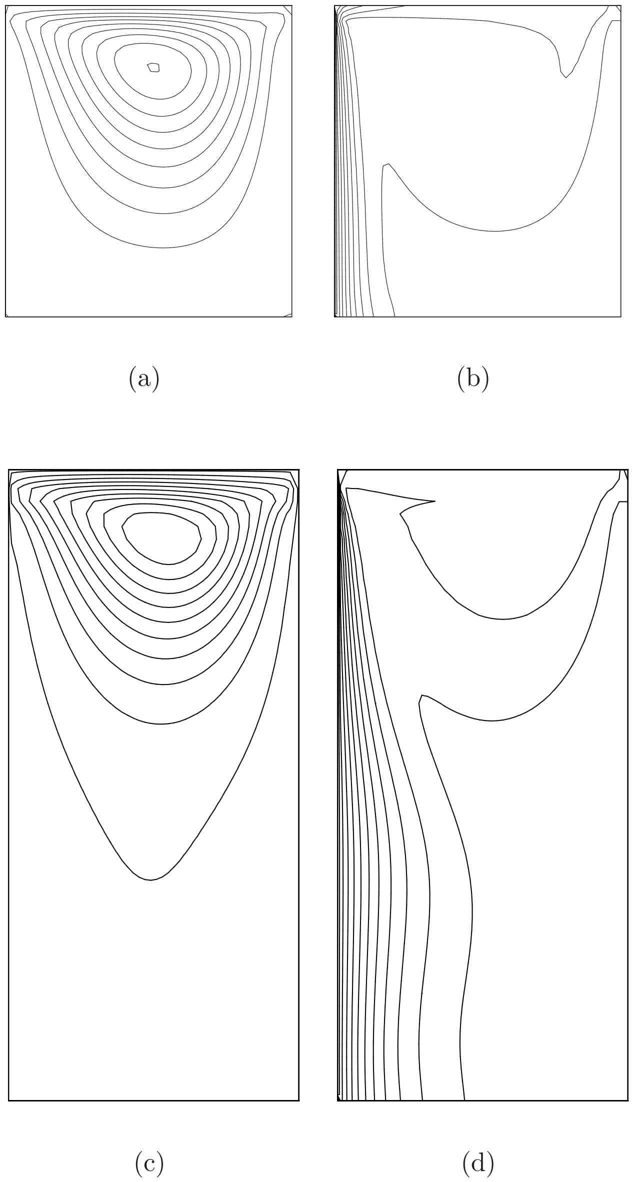

Figure 5.34: Axisymmetric streamfunction ψ_0 (a,c) and temperature field θ_0 (b,d) for $\mathrm{Pr} = 27$, $\mathrm{Gr} = 1000$, and $\eta = 0.08$. Results are shown for $\Gamma = 1$ and $\mathrm{Re} = 1,400$ (a,b) and for $\Gamma = 0.5$ and $\mathrm{Re} = 29,000$ (c,d).

In order to compare our stability results with those of Kamotani *et al.* (1992) we calculated the critical Reynolds numbers $\mathrm{Re}_c^{\mathrm{exp}}$ from the measured temperature differences $\Delta\mathsf{T}_c^{\mathrm{exp}}$ using the material data provided. The critical Reynolds numbers Re_c are shown in table 5.4 along with the experimental data.

The deviation $\Delta = \mathrm{Re}_c^{\mathrm{num}} - \mathrm{Re}_c^{\mathrm{exp}}$, and the Gaussian error σ_{Re_c} calculated by equation

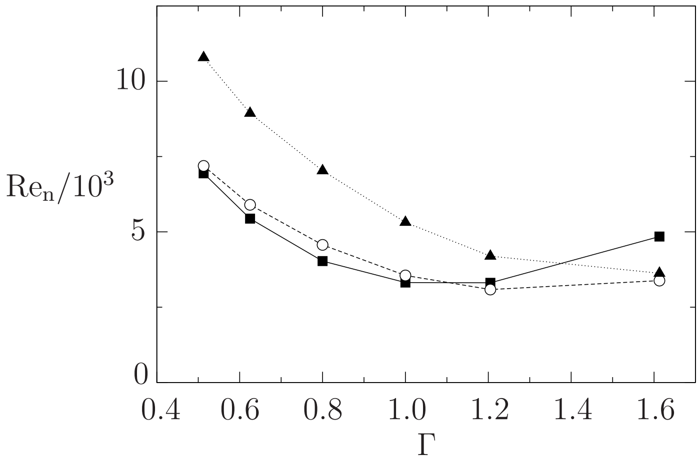

Figure 5.35: Neutral Reynolds numbers $\mathrm{Re_n}$ of the most dangerous neutral modes as a function of the aspect ratio Γ. Parameters are $\eta = 0.079$ and $\mathrm{Pr} = 27$. For Bd, see table 5.3. The wave numbers are $m = 2$ (■, full line), $m = 3$ (○, dashed line), and $m = 4$ (▲, dotted line).

Table 5.3: Geometrical, setup and critical parameters for Prandtl number $\mathrm{Pr} = 27$ and heater radius ratio $\eta = 0.079$.

Γ	Ar	Bo	Bd	Re_c	ω_c	m_c
1.613	0.62	2.6239	0.9424	3,790	21.35	3
1.205	0.83	2.5982	0.9455	3,440	27.63	3
1.000	1.00	2.5914	0.9461	3,512	37.23	2
0.800	1.25	2.5836	0.9468	4,356	53.42	2
0.625	1.60	2.5765	0.9473	6,067	87.11	2
0.513	1.95	2.5776	0.9477	7,874	129.83	2

(5.4) are also given. Figure 5.36 displays both results together with the corresponding error margins.

In view of the shortcomings and uncertainties the agreement is satisfactory. We can thus conclude that the instability mechanism that can be deduced from the numerical calculations (section 5.2.4) indeed represents the mechanisms at work in the experimental realization.

Even though the radius ratio of the heater is rather small, it effects the critical onset. To that end we computed the critical Reynolds number for a constant aspect ratio $\Gamma = 0.513$ for various radius ratios η. The results are shown in fig. 5.37 for the most dangerous modes. The aspect ration has been selected in order to compare our results to the measurements of Kamotani *et al.* (1992) for $\mathrm{Ar} = 1.95$. A list of critical parameters is given in table 5.5.

It is seen that the neutral stability boundaries for $m = 2$ and $m = 3$ are very close.

Table 5.4: Aspect ratio dependence of the numerical (present) and experimental (Kamotani *et al.*, 1992) critical Reynolds number for silicone oil of Pr = 27 and a heater radius ratio $\eta = 0.079$ under normal gravity conditions. Also given is the deviation Δ and the Gaussian uncertainty computed by (5.4).

Γ	present $\mathrm{Re}_c^{\mathrm{num}}$	Kamotani *et al.* (1992) $\mathrm{Re}_c^{\mathrm{exp}}$	Δ	σ_{Re_c}
1.613	3,790	2,856	934	±410
1.205	3,440	2,941	499	±429
1.000	3,512	3,334	178	±488
0.800	4,356	3,871	486	±569
0.625	6,067	4,753	1,314	±701
0.513	7,874	5,568	2,306	±824

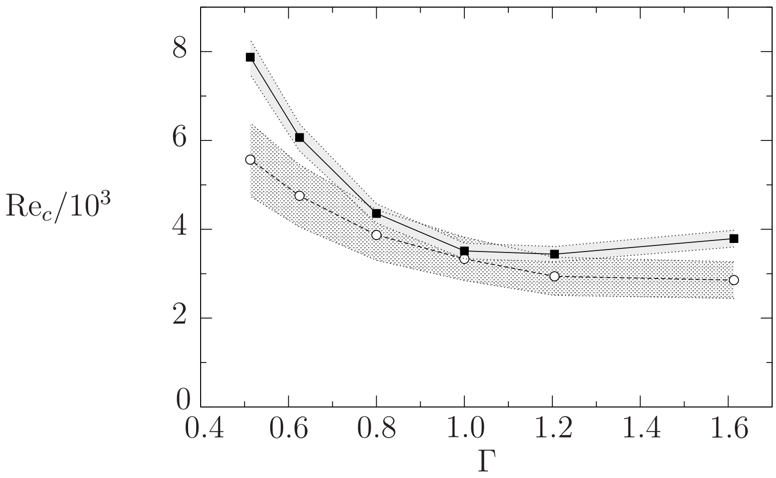

Figure 5.36: Critical Reynolds number Re_c as a function of the aspect ratio Γ. The parameters are $\eta = 0.079$ and Pr = 27. For Bd, see table 5.3. Shown are experimental results of Kamotani *et al.* (1992) (○, dashed line) and the present numerical stability boundary data (■, solid line). The experimental uncertainty due to the surface-temperature measurement and the possible numerical variation σ_{Re_c} are indicated as dark and light grey shading, respectively, and by dotted lines.

The numerical stability analysis predicts $m = 2$ to be the critical wave number in the range of radius ratios investigated.

A comparison of the numerical data with the experiments of Kamotani *et al.* (1992) is provided in fig. 5.38 showing the predicted and measured critical Reynolds numbers Re_c as function of the heater radius ratio, as well as the uncertainties resulting from the measurement, numerical inaccuracies, and the uncertainty of the material parame-

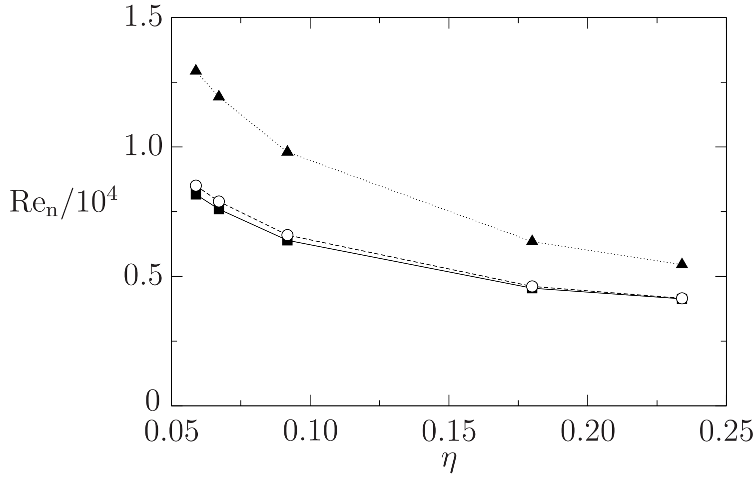

Figure 5.37: Neutral Reynolds numbers as a functions of the heater radius ratio η. The parameters are $\Gamma = 0.513$ and $\mathrm{Pr} = 27$. For Bd, see table 5.5. The wave numbers are $m = 2$ (■, full line), $m = 3$ (○, dashed line), and $m = 4$ (▲, dotted line).

Table 5.5: Critical data for $\mathrm{Pr} = 27$ and $\Gamma = 0.513$.

η	Bo	Bd	Re_c	ω_c	m_c
0.0588	3.9005	1.4340	9,602	135.53	2
0.0671	3.9007	1.4341	9,026	135.58	2
0.0918	3.8907	1.4350	7,863	136.06	2
0.1800	3.8684	1.4375	6,271	141.54	2
0.2340	3.8512	1.4395	6,043	148.57	2

ters. In view of the uncertainties and the approximations made, the agreement is quite satisfactory.

Table 5.6 gives the numerical data for the critical temperature differences as a function of the radius ratio, the difference of the results $\Delta = \mathrm{Re}_c^{\mathrm{num}} - \mathrm{Re}_c^{\mathrm{exp}}$, and the Gaussian error. The influence of buoyancy on the onset of the non-axisymmetric flow state has been studied for a representative case with aspect ratio $\Gamma = 1$, heater radius ratio $\eta = 0.1$, Prandtl number $\mathrm{Pr} = 27$. The dynamic Bond number has been varied in the range $\mathrm{Bd} \in [0, 3.87]$. Critical Reynolds numbers for the three most dangerous modes with wave numbers $m = 2$, 3, and 4 are presented in fig. 5.39. Mode $m = 2$ turns out to be the critical one in the range considered. The critical Reynolds number increases monotonically with the dynamic Bond number. Therefore, buoyancy acts stabilizing in the range of dynamic Bond numbers $\mathrm{Bd} \leq 3.87$.

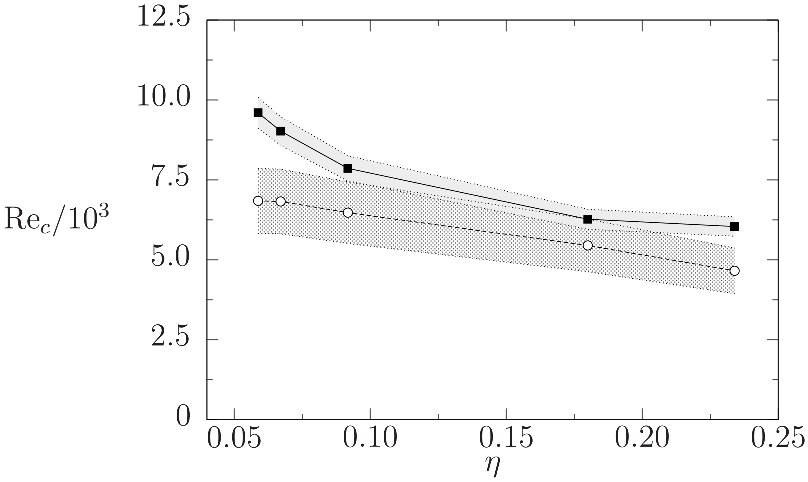

Figure 5.38: Critical Reynolds number Re_c as function of the radius ratio η for $\Gamma = 0.513$ and $\mathrm{Pr} = 27$. For Bd, see table 5.5. Shown are experimental results of Kamotani *et al.* (1992) ($\circ$, dashed line) and the present numerical stability boundary data ($\blacksquare$, solid line). The experimental uncertainty due to the surface-temperature measurement and the possible numerical variation σ_{Re_c} are indicated as dark and light grey shading, respectively, and by dotted lines.

Table 5.6: Numerical (present) and experimental (Kamotani *et al.*, 1992) critical Reynolds numbers for $\mathrm{Pr} = 27$ and $\Gamma = 0.513$.

η	present $\mathrm{Re}_c^{\mathrm{num}}$	Kamotani *et al.* (1992) $\mathrm{Re}_c^{\mathrm{exp}}$	Δ	σ_{Re_c}
0.0588	9,602	6,846	2,755	±1,013
0.0671	9,026	6,826	2,200	±1,011
0.0918	7,863	6,477	1,386	±964
0.1800	6,271	5,451	819	±824
0.2340	6,043	4,659	1,384	±715

5.2.4 Instability mechanism

It is instructive to first analyze the instability mechanism for $\mathrm{Bd} = 0$, i.e. for zero gravity conditions. These conditions also apply to the STDCE-2 experiment (Pline *et al.*, 1996; Kamotani *et al.*, 2000). As a representative case we consider $\Gamma = 1$, $\eta = 0.1$, and $\mathrm{Pr} = 27$. The critical wave number is $m = 2$ with a critical Reynolds number of $\mathrm{Re}_c = 2,762$. The critical mode is a time-dependent azimuthally traveling wave with critical circular frequency $\omega_c = 32.68$.

The critical temperature and velocity field θ and $\boldsymbol{u}$, respectively, at the free surface

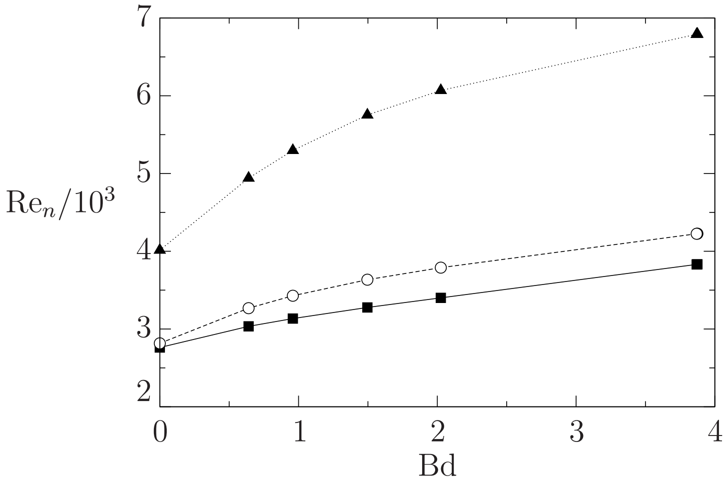

Figure 5.39: Neutral Reynolds numbers as functions of the dynamic Bond number Bd for $\mathrm{Pr} = 27$, $\Gamma = 1$, and $\eta = 0.1$. The wave numbers are $m = 2$ (■, full line), $m = 3$ (○, dashed line), and $m = 4$ (▲, dotted line).

are shown in fig. 5.40a.

Eight surface temperature extrema exist. Four small and strong ones are located close to the heater, while the other larger but weaker ones occupy the remainder of the free surface. The perturbation flow at the free surface is directed mainly from the weak hot to the weak cold perturbation temperature spots. As fig. 5.41 proves, the flow is nearly entirely driven by Marangoni stresses.

Apart from the azimuthal surface flow there is also a considerable radial perturbation flow driven by Marangoni stresses from the large hot surface spots to the small but intense cold surface spots.

As can be seen from fig. 5.42ls part of the stream descending radially outwards from the small surface spots close to the axis turns radial inward in the bulk such that the perturbation flow is almost perpendicular to the isolines of the basic state temperature field. By convecting the basic-downward and radially inward (in the plane shown) perturbation flow creates the perturbation temperature field. It arises in form of a elongated cigar-shaped temperature perturbation aligned parallel and in close vicinity of the heated inner cylinder (blue in fig. 5.42ls). The effect is significant despite of the relatively weak perturbation flow, but the thermal boundary layer on the heater is quite strong. At an angle of $\pm\pi/2$ with respect to the plane plotted in figure 5.42 the perturbation flow $\boldsymbol{u}$ is directed outwards, hence, perturbation temperature maxima occur there. Perturbation temperature of opposite sign is created in the same azimuthal plane by convecting the basic-state temperature with opposite gradient which is associated with the convective deformation of the isotherm due to the basic vortex (red in fig. 5.42ls). In fact, the temperature perturbation is produced in the volume of the annulus, the maximum of i_T being located in the plane $z \approx -0.03$ near the midplane of the pool. The location of the maximum thermal production is shifted by $\Delta\varphi = 15°$ in clockwise direction with respect to the perturbation temperature extrema. The relevant cuts are given in figures 5.42

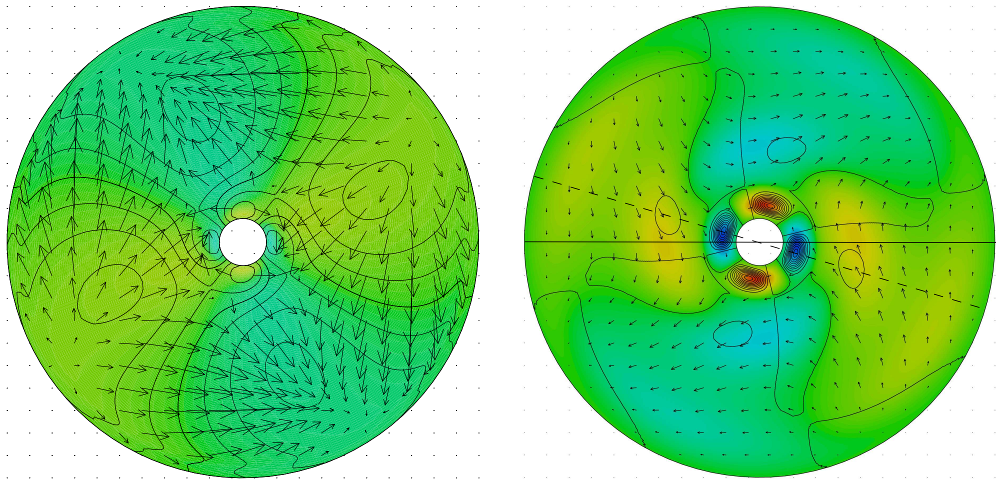

(a) (b)

Figure 5.40: Critical mode with $m = 2$ for $\Gamma = 1$, $\eta = 0.1$, $\mathrm{Bd} = 0$, and $\mathrm{Pr} = 27$ at $\mathrm{Re}_c = 2,762$ at the free surface $z = 0.5$ (a) and near the midplane $z = -0.03$ (b). The mode rotates clockwise with $\omega_c = 32.68$. Shown is the perturbation flow $\boldsymbol{u}$ (arrows) and the perturbation temperature θ (color). Both fields are scales identically. In addition, θ is also indicated by isoline in (a) while isolines in (b) show the local thermal energy production i_T at $z = -0.03$ where i_T has local maxima in the bulk. The straight and the dashed line indicate the angles at which the cuts of figs. 5.42ls,rs are taken.

and their location is indicated in figure 5.40b. The internal perturbation temperature extrema are created by advection of the basic state temperature field θ_0 by means of the perturbation flow $\boldsymbol{u}$ (fig. 5.42ls).

The temperature perturbation spots at the free surface themselves are created by the advection $\boldsymbol{u}_0 \cdot \nabla\theta$ of the perturbation temperature field θ by means of the basic flow field $\boldsymbol{u}_0$. This can be recognized from fig. 5.43.

The isosurfaces of the perturbation temperature extrema of large volume are stretched along the basic-state streamlines: axially upward near heating cylinder and radially outward along the free surface. From fig. 5.43 one can also see that the temperature perturbation θ in the bulk occurs slightly clockwise ahead of the perturbation at the free surface. This shift is explained by the clockwise rotation of the perturbation mode. The surface spots lag behind the bulk spots due to the finite time required for the basic flow $\boldsymbol{u}_0$ to advect the bulk perturbation temperature to the free surface. Consistent with the pattern rotation the local thermal energy production i_T reaches its maximum slightly clockwise ahead of the perturbation temperature extrema (cf. fig. 5.40b).

The critical mode is an azimuthally propagating wave. It is characterized by strong temperature extrema in the bulk and weaker temperature extrema at the free surface, lagging behind the bulk extrema. The perturbation flow necessary for the thermal

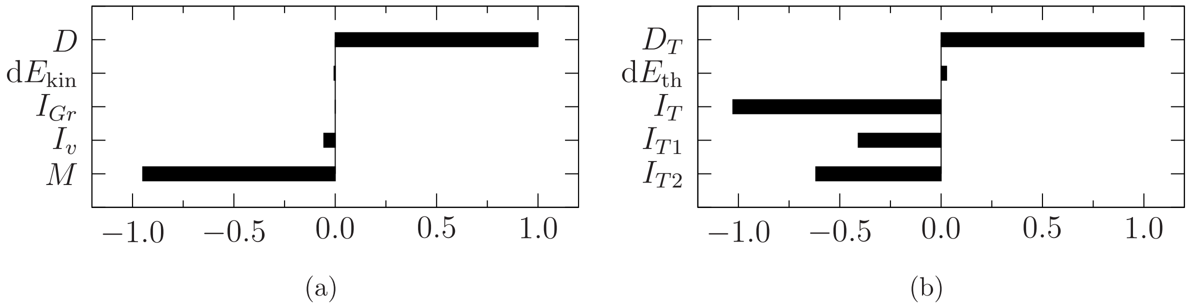

Figure 5.41: Terms of the kinetic (a) and the thermal energy balance (b) for $\mathrm{Bd} = 0$, $\eta = 0.1$, $\Gamma = 1$, $\mathrm{Pr} = 27$, and $m = 2$ at $\mathrm{Re}_c = 2,762$.

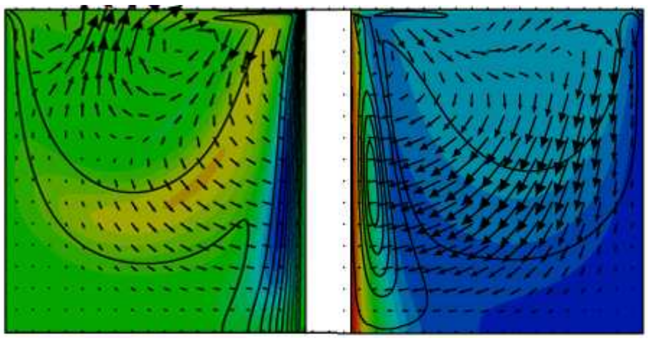

Figure 5.42: Flow and temperature fields ($m = 2$) for $\mathrm{Bd} = 0$, $\eta = 0.1$, $\mathrm{Pr} = 27$, and $\mathrm{Re} = \mathrm{Re}_c = 2,762$ in a vertical cut at which the critical temperature perturbation takes its absolute maximum. All fields are mirror-symmetric with respect to $r = 0$ for $m = 2$. (left side - ls) Critical velocity field $\boldsymbol{u}$ (arrows), critical temperature field θ (color), and basic-state temperature field θ_0 (lines). (right side - rs) Local thermal production rate $i_T > 0$ (lines) and basic state temperature field θ_0 for the same parameters as in (left side). The vertical cut is shifted by $\Delta\varphi = 15°$ in clockwise direction to an azimuthal angle where the local thermal production i_T (color) takes its maximum.

production in the bulk is generated by the surface temperature extrema. These key features of the instability are identical to those of high-Prandtl-number hydrothermal waves. They have been originally been discovered by Smith (1986) but also exist in other thermocapillary systems such as liquid bridges Wanschura *et al.* (1995*b*).

In the earth-bound experiments of Kamotani *et al.* (1992) the dynamic Bond number was of the order of $\mathrm{Bd} = O(1)$ to $O(1.5)$. From fig. 5.39 we notice that the critical Reynolds number differs only by 15% to 20% relative to zero-gravity conditions. This suggests that the instability mechanism in the laboratory experiments have been essentially the same as under weightlessness conditions. But even for $\mathrm{Bd} = 4$ the difference is only about 40% and therefore we expect only a slight modification of the instability

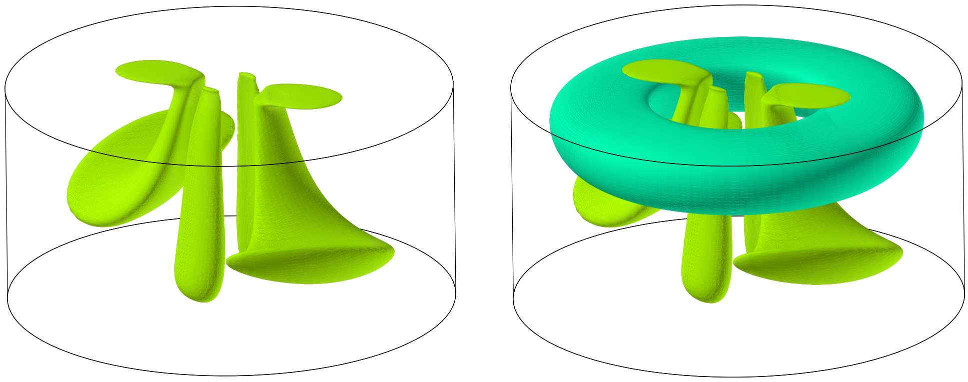

(a)

(b)

Figure 5.43: Isosurfaces of the perturbation temperature field θ alone (a) and together with an Isosurface of the basic-state stream function ψ_0 for $\mathrm{Bd} = 0$, $\eta = 0.1$, $\mathrm{Pr} = 27$, $\mathrm{Re} = \mathrm{Re}_c = 2,762$, and $m = 2$.

mechanism.

6 Concluding remarks

In the present work the thermocapillary flows in (i) a cylindrical liquid pool heated by a parabolic heat flux from above and (ii) an annular pool heated by a cylindrical heater along its axis have been studied. Of particular interest were the necessary conditions for the onset of non-axisymmetric fluid motion, and the underlying physical mechanism driving the transition process.

A physical model including the governing equations for the axisymmetric basic state, the linear stability problem and sound boundary conditions has been developed and presented in sec. 2. The concept of neutral and critical stability has been introduced and the equations for the energy analysis have been derivated and adapted to the specific geometry of the problems.

The numerical implementation of the equations and the corresponding boundary conditions stated in sec. 2 was treated in sec. 3. The discretization process by means of finite volumes on an optionally uniform or non-uniform staggered grid has been explained and all methods necessary for the computation of the neutral and critical stability curves discussed.

Considerable effort was put into the validation of the numerical code developed for the present work. To that end the boundary conditions of the problem were modified to compute solutions to the floating zone problem, a problem well documented and cited in literature. The results given in sec. 4 show very good agreement to previous works. As a second test the convergence behaviour (resolution dependence) of the computed solutions was studied. Again the results were very satisfying.

6.1 Concluding remarks on the results of the liquid-pool model

The results computed for the liquid-pool model, a cylindrical volume of fluid with a non-deformable free surface on top, heated by a parabolic heat flux on its free surface, have been presented in sec. 5.1. The configuration has been studied for various Prandtl numbers Pr, aspect ratios Γ and dynamic Bond numbers Bd.

For parameters aspect ratio $\Gamma = 1$ and a Prandtl numbers from $\mathrm{Pr} = 10^{-10}$ to 10, we found a distinct separation into a small- ($\mathrm{Pr} \lesssim 1$) and a high-Prandtl-number-range ($\mathrm{Pr} \gtrsim 1$). In the low-Prandtl-number-range the perturbation flow is stationary in nature and the basic flow is unstable to a combination of centrifugal effects and vortex straining[1]. In the range $0.04 \lesssim \mathrm{Pr} \lesssim 1$ there is also a noticeable contribution by Marangoni

[1]

forces, compare sec. 5.1.1. The perturbation mode in the high-Prandtl-number-range is oscillatory in nature, the kinetic energy budget dominated by the Marangoni terms, and the physical instability mechanism turns out to be a hydrothermal-wave-mechanism (HTW-mechanism), cp. Smith (1986) and sec. 5.1.1.

The aspect ratio dependence was presented in three sections each for a well selected significant Prandtl number. Sec. 5.1.2 studies the aspect ratio dependence in the limit of asymtotically small Prandtl number ($\mathrm{Pr} = 10^{-10}$), sec. 5.1.3 in the low Prandtl number range ($\mathrm{Pr} = 0.03$) and sec. 5.1.4 for high Prandtl number ($\mathrm{Pr} = 4$).

The results presented in sec. 5.1.2 ($\mathrm{Pr} = 10^{-10}$) feature three distinct regions: (i) a low aspect-ratio-range $0.5 \leq \Gamma \lesssim 1.91$ with a stationary perturbation mode and physics like in sec. 5.1.1 (ii) an intermediate aspect-ratio-range $1.91 \lesssim \Gamma \lesssim 3.31$ showing an oscillatory perturbation mode. The instability mechanism is centrifugal and features similarities to the mechanism discussed in sec. 5.1.1, finally (iii) a high aspect-ratio-region $\Gamma \gtrsim 3.31$ with a basic flow unstable to a stationary perturbation mode. The instability mechanism differs from the earlier discussed centrifugal mechanism, in which most of the local kinetic energy transfer from the basic flow to the perturbation mode took place in the downflow region along the outer streamlines of the primary vortex of the basic flow where criteria (5.2) was satisfied. In the high-aspect-ratio-range there is still some local kinetic energy production in the upflow region of the primary vortex yet most of the kinetic energy is produced in a region close to the axis of the pool. We concluded that the mechanism which features similarities with a divergent instability is primarily a property of the turning flow near the axis of the pool. Further comparison is needed to sufficiently clarify this issue.

In sec. 5.1.3 ($\mathrm{Pr} = 0.03$) we found that the critical mode is always stationary for low Prandtl number. Of the three branches (two stationary, one oscillatory) found for $\mathrm{Pr} = 10^{-10}$ only one stationary branch remains for small Prandtl number. The critical curve features an increase of the critical wave number m_c with aspect ratio. From the kinetic energy budget we found that for $\mathrm{Pr} = 0.03$ the contribution of the Marangoni forces (inertial effects) increases (decreases) with aspect ratio for $\Gamma \lesssim 4.3$. For $\Gamma \gtrsim 4.3$ the contribution of the Marangoni forces decreases while at the same time inertia effects get more important for the instability of the basic state flow. Note however that the perturbation flow at the free surface is increasingly dominated by Marangoni effects for increasing aspect ratio. A possible explanation would be the downward shift of the vortex center, and hence of the region of inertial kinetic energy production, with increasing aspect ratio. I.e. we find a situation where the perturbation flow at the free surface is dominated by inertial effects for low aspect ratio and by the Marangoni effect for large aspect ratio.

The aspect-ratio-dependence of the critical stability boundary for high Prandtl number ($\mathrm{Pr} = 4$) was presented in sec. 5.1.4, and the instability mechanism identified as a hydrothermal wave mechanism, compare sec. 5.1.1 and Smith (1986). In terms of the kinetic energy balance we found that the relative significance of the inertial kinetic energy production with respect to the Marangoni terms increases with aspect ratio. If this tendency continues for even higher values of Γ we might find a situation very similar to the one found for $\mathrm{Pr} = 0.03$ and sufficiently high values of Γ. I.e. while the prior instability mechanism is surely a hydrothermal wave mechanism in the computed range, the instability might be dominated by centrifugal effects for larger aspect ratios.

Finally the effect of gravitational acceleration on the stability of the overall flow was studied in sec. 5.1.5. To that end the stability curves for Prandtl numbers $\mathrm{Pr} = 10^{-10}$ and $\mathrm{Pr} = 10$ in the dynamic Bond number range from $\mathrm{Bd} = 0.0398$ to 50.1 have been computed. We found that buoyancy effects destabilize the flow for asymptotically small Prandtl number $\mathrm{Pr} = 10^{-10}$ and stabilize it for high Prandtl number $\mathrm{Pr} = 10$.

6.2 Concluding remarks on the results of the annular pool

Some experimental and numerical results presented by Kamotani *et al.* (1992) have been studied and recomputed with the authors numerical code. In detail the dependency of the critical temperature difference for the onset of a non-axisymmetric flow on the aspect ratio of the test section as well as the radius ratio of the heater has been studied for a Boussinesq fluid with Prandtl number $\mathrm{Pr} = 27$. All results of Kamotani et al. could be verified to a reasonable degree. If one considers the simplicity of the used numerical approach the agreement of the results is really very good.

The dependence of the neutral and the critical Reynolds number on the dynamic Bond number has been studied. A shift of the critical stability limit to higher values of Reynolds number with increasing dynamic Bond number has been found. Hence the authors conclude that buoyancy yields a stabilizing effect on the flow field.

The structure of the pair of oscillating perturbation modes has been intensively studied. The mechanism responsible for the instability has been identified as a hydrothermal wave, Smith (1986).

6.3 Concluding with a few general remarks

The present work succeeded in the effort to increase the understanding of the underlying physical mechanisms which render an axisymmetric flow unstable to a three dimensional perturbation mode. Surprisingly enough the basic flow structures and also the instability mechanism found in both problems feature strong similarities to those found in prior studies of thermocapillary liquid bridges (half-zone model) (Nienhüser, 2002; Wanschura *et al.*, 1995*b*). A similarity stressed also in prior publications on the pattern formation process in buoyant-thermocapillary liquid pools heated by a parabolic heat flux from above (Schoisswohl & Kuhlmann, 2006, 2007).

A Modifications for the annular pool

In order to compute the results presented in sec. 5.2 some modifications of the theoretical approach (sec. 2) and the numerical implementation (sec. 3) are necessary.

A.1 Modifications in the Theoretical Approach

Sofar we have studied a cylindrical pool filled with a Boussinesq fluid. Now with the cylindrical heater submerged into the pool along its axis we get what we could basically call an open cylindrical annulus with inner radius R_i and outer radius R in an axial gravity field. Together with the height d of the container its geometry is defined by the radius ratio $\eta = R_i/R$ and an unchanged aspect ratio $\Gamma = R/d$. The outer and inner cylindrical sidewalls are kept at constant temperature T_0 and $\mathsf{T}_0 + \Delta\mathsf{T}$, respectively. The setup is sketched in figure A.1.

Owing to the temperature variation across the gap the fluid motion is driven by thermocapillary and buoyancy forces. We assume the temperature difference $\Delta\mathsf{T}$ to be small such that the capillary number $\mathrm{Ca} = \gamma\Delta\mathsf{T}/\sigma_0 \ll 1$ is small, where γ is the surface tension coefficient and σ_0 the mean surface tension. In this limit dynamic surface deformations are absent and we can approximate the fluid motion using the equations of the Boussinesq approximation in cylindrical coordinates (r, φ, z) in non-dimensional (2.22a)-(2.22c) presented in sec. 2

$$\frac{\partial \boldsymbol{U}}{\partial t} + (\boldsymbol{U}\cdot\nabla)\boldsymbol{U} = -\nabla P + \nabla^2\boldsymbol{U} - \mathrm{Gr}\Theta\boldsymbol{e}_z \tag{A.1a}$$

$$\frac{\partial \Theta}{\partial t} + (\boldsymbol{U}\cdot\nabla)\Theta = \frac{1}{\mathrm{Pr}}\nabla^2\Theta \tag{A.1b}$$

$$\nabla\cdot\boldsymbol{U} = 0 \quad , \tag{A.1c}$$

where $\boldsymbol{U} = (U, V, W)^{\mathrm{T}}$ is the vector radial, azimuthal and axial velocity components, P is the pressure, and $\Theta = (\mathsf{T} - \mathsf{T}_0)/\Delta\mathsf{T}$ denotes the temperature field. The scales are d, d^2/ν, ν/d, $\rho\nu^2/d^2$, and $\Delta\mathsf{T}$ for length, time, velocity, pressure, and temperature.

To complete the mathematical formulation we assume no-slip conditions on the solid walls and adiabatic top and bottom boundaries. Hence, we require

$$\boldsymbol{U}(r = \eta\Gamma, z) = \boldsymbol{U}(r = \Gamma, z) = \boldsymbol{U}(r, z = -1/2) = 0 \quad , \tag{A.2}$$

$$\Theta(r = \eta\Gamma, z) - 1 = \Theta(r = \Gamma, z) = \left.\frac{\partial\Theta}{\partial z}\right|_{z=\pm 1/2} = 0 \quad . \tag{A.3}$$

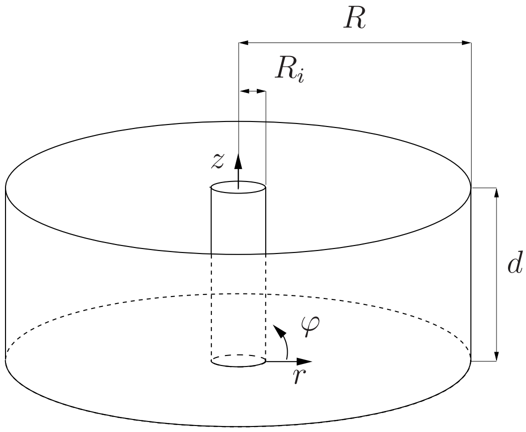

Figure A.1: Geometry and coordinate system.

On the free surface at $z = 1/2$ we require no deformation $W(r, z = 1/2) = 0$ and neglect the viscosity of the ambient gas in the stress balance which leads to (see, e.g. Kuhlmann, 1999)

$$\frac{\partial \boldsymbol{U}_\parallel}{\partial z} + \mathrm{Re}\nabla_\parallel \Theta = 0 \quad , \tag{A.4}$$

where $\boldsymbol{U}_\parallel = U\boldsymbol{e}_r + V\boldsymbol{e}_\varphi$ is the surface velocity and $\nabla_\parallel = \boldsymbol{e}_r\partial_r + \boldsymbol{e}_\varphi r^{-1}\partial_\varphi$ the horizontal Nabla operator.

The problem is governed by three independent dimensionless parameters. The thermocapillary Reynolds, Prandtl, and Grashof numbers are defined as

$$\mathrm{Re} = \frac{\gamma \Delta \mathsf{T} d}{\rho \nu^2} \quad , \quad \mathrm{Pr} = \frac{\nu}{\kappa} \quad \text{and} \quad \mathrm{Gr} = \frac{\beta \Delta \mathsf{T} g d^3}{\nu^2} \quad , \tag{A.5}$$

where κ is the thermal diffusivity, ν the kinematic viscosity, and β the thermal expansion coefficient of the liquid at constant pressure. It is useful to define, in addition, the (dependent) dynamic Bond number

$$\mathrm{Bd} = \frac{\mathrm{Gr}}{\mathrm{Re}} = \frac{\beta \rho g d^2}{\gamma} \quad . \tag{A.6}$$

A.2 Modifications in the Numerical Implementation

In terms of numerical implementation the computational mesh needs to be adapted to the new geometrical constraints. Sofar the innermost column of computational cell was situated at the axis with an inner radial coordinate of $r_1 = 0$, compare sec. 3.1.2. Its new position is $r_1 = \eta\Gamma$ and the new radial coordinates are hence given by

$$r_j = \begin{cases} -\Delta r_1 + \eta\Gamma & \text{for} \quad j = 0 \\ \eta\Gamma & \text{for} \quad j = 1 \\ r_{j-1} + \Delta r_{j-1} & \text{for} \quad j = 2, ..., N_r + 1 \\ r_{N_r+1} + \Delta r_{N_r} & \text{for} \quad j = N_r + 2 \end{cases},$$

with cell sizes Δr_j defined in sec. 3.1.2.

B Derivation of the energy analysis

In this section we present a derivation of the rate of change of kinetic and thermal energy in the cylindrical volume V for cylindrical coordinates and the boundary conditions of the present problem defined in sec. 2.

B.1 Reynolds-Orr equation

Assuming that the flow state $\boldsymbol{X}$ can be decomposed into a combination of a axisymmetric basic state $\boldsymbol{x}_0$ and a perturbation mode $\boldsymbol{x}$ equation (2.22a) takes the form

$$\partial_t(\boldsymbol{u}_0+\boldsymbol{u})+\left[(\boldsymbol{u}_0+\boldsymbol{u})\cdot\nabla\right](\boldsymbol{u}_0+\boldsymbol{u}) = -\nabla(p_0+p)+\Delta(\boldsymbol{u}_0+\boldsymbol{u})+Gr(\theta_0+\theta)\boldsymbol{e}_z \quad . \tag{B.1}$$

In the next step equation (2.22a) is rewritten solely for the basic state $\boldsymbol{x}_0$ and in this new form substracted from equation (B.1). A linearisation with respect to higher order terms in the perturbation gives

$$\partial_t\boldsymbol{u}+\boldsymbol{u}\cdot\nabla\boldsymbol{u}_0+\boldsymbol{u}_0\cdot\nabla\boldsymbol{u} = -\nabla p+\Delta\boldsymbol{u}+Gr\theta\boldsymbol{e}_z \quad . \tag{B.2}$$

A multiplication by the perturbation velocity vector $\boldsymbol{u}$ from the left-hand side, followed by an integration by volume and a reformulation in tensor notation yields

$$\frac{1}{2}\langle\partial_t u_i^2\rangle+\langle u_i(u_{0,j}\partial_j)u_i\rangle+\langle u_i(u_j\partial_j)u_{0,i}\rangle = -\langle u_i\partial_i p\rangle+\langle u_i\partial_j\partial_j u_i\rangle+\langle \mathrm{Gr}\theta u_i\delta_{i3}\rangle \quad . \tag{B.3}$$

Here $\langle ...\rangle$ is equivalent to $\int ... \, dV$, the integration by volume. In what follows we use the boundary conditions and continuity ($\nabla\cdot\boldsymbol{u}=0$) to cast equation (B.3) into a simpler form.

The first term in equation (B.3)

$$\frac{1}{2}\langle\partial_t u_i^2\rangle = \frac{\partial E_{kin}}{\partial t} \quad . \tag{B.4}$$

is equivalent to the temporal change of kinetic energy. Since we study a stationary system this term should vanish.

Using partial integration the first nonlinear term is reformulated to

$$\begin{aligned}
\langle u_i(u_{0,j}\partial_j)u_i\rangle &= \langle u_i u_{0,j} e_j u_i\rangle_S - \langle\partial_j(u_i u_{0,j})u_i\rangle && \text{(B.5a)}\\
&= \langle u_i \underbrace{u_{0,j} e_j}_{=0} u_i\rangle_S - \langle u_i(\underbrace{\partial_j u_{0,j}}_{=0})u_i\rangle - \langle u_{0,j}(\partial_j u_i)u_i\rangle \quad . && \text{(B.5b)}
\end{aligned}$$

Here e_j is the unity normal vector at the free surface. Due to the assumption of a non-deformable free surface the axial velocity component w_0 of $\boldsymbol{u}_0$ vanishes at the free surface. Obviously the same is true for its projection $e_j u_{0,j}$. Since our flow is divergence free $\partial_j u_{0,j}$ drops out as well and equation (B.5) is reduced to

$$\langle u_i (u_{0,j}\partial_j) u_i \rangle = -\langle u_{0,j}(\partial_j u_i) u_i \rangle \quad . \tag{B.6}$$

A condition only satisfied if

$$\langle u_i (u_{0,j}\partial_j) u_i \rangle = 0 \quad , \tag{B.7}$$

and hence the first nonlinear term in (B.3) drops out altogether.

Reformulation of the second nonlinear term for cylinder coordinates gives

$$\begin{aligned} \langle u_i (u_j \partial_j) u_{0,i} \rangle &= \left\langle (\boldsymbol{e}_r u + \boldsymbol{e}_\varphi v + \boldsymbol{e}_z w) \cdot \left[\left(u\partial_r + \tfrac{v}{r}\partial_\varphi + w\partial_z \right) (\boldsymbol{e}_r u_0 + \boldsymbol{e}_z w_0) \right] \right\rangle \\ &= \langle u^2 \partial_r u_0 \rangle + \langle uw \partial_z u_0 \rangle + \left\langle \tfrac{v^2 u_0}{r} \right\rangle + \langle uw \partial_r w_0 \rangle + \langle w^2 \partial_z w_0 \rangle \quad . \end{aligned} \tag{B.8}$$

Note that the derivations of the unity coordinate vectors in cylindrical coordinates are $\partial_\varphi \boldsymbol{e}_r = \boldsymbol{e}_\varphi$ and $\partial_\varphi \boldsymbol{e}_\varphi = -\boldsymbol{e}_r$.

Let us now consider the terms on the right hand side of equation (B.3). For the pressure term partial integration shows that

$$\langle u_i (\partial_i p) \rangle = \langle \underbrace{u_i e_i}_{=0} p \rangle_S - \langle \underbrace{\partial_i u_i}_{=0} p \rangle = 0 \quad . \tag{B.9}$$

Here the line of argumentation is the same as in equation (B.5b).

Partial integration of the dissipative term shows that it is equivalent to a combination of a surface and a volume term

$$\langle u_i \partial_j \partial_j u_i \rangle = \langle u_i e_j \partial_j u_i \rangle_S - \langle (\partial_j u_i)(\partial_j u_i) \rangle \quad . \tag{B.10}$$

The surface term can be rewritten to

$$\langle u_i e_j \partial_j u_i \rangle_S = \int_S dS \boldsymbol{u} \cdot [(\boldsymbol{n} \cdot \nabla) \boldsymbol{u}] \overset{\boldsymbol{n} \equiv \boldsymbol{e}_z}{=} \int_S dS (u \partial_z u + v \partial_z v) \quad , \tag{B.11}$$

with $\boldsymbol{n}$ being the unity normal vector at the free surface. Reformulation of the volume term in equation (B.10) by means of a vector identity taken from Bronstein & Mühlig (2001) yields

$$\langle (\partial_j u_i)(\partial_j u_i) \rangle = \langle (\nabla \boldsymbol{u})(\nabla \boldsymbol{u}) \rangle = \langle (\nabla \times \boldsymbol{u})^2 \rangle + \langle \nabla \cdot [(\boldsymbol{u} \cdot \nabla) \boldsymbol{u}] \rangle \quad . \tag{B.12}$$

In cylindrical coordinates $(\nabla \times \boldsymbol{u})^2$ takes the form

$$(\nabla \times \boldsymbol{u})^2 = \left(\frac{1}{r}\frac{\partial w}{\partial \varphi} - \frac{\partial v}{\partial z} \right)^2 + \left(\frac{\partial u}{\partial z} - \frac{\partial w}{\partial r} \right)^2 + \left(\frac{1}{r}\frac{\partial (rv)}{\partial r} - \frac{1}{r}\frac{\partial u}{\partial \varphi} \right)^2 \quad . \tag{B.13}$$

The second term in equation (B.12) can be restated as a surface term

$$\langle \nabla \cdot [(\boldsymbol{u} \cdot \nabla)\boldsymbol{u}] \rangle = \langle \boldsymbol{n} \cdot (\boldsymbol{u} \cdot \nabla)\boldsymbol{u} \rangle_S \quad , \tag{B.14}$$

which vanishes for a flat free surface ($\boldsymbol{n} = \boldsymbol{e}_z$)

$$\int_S dS\boldsymbol{n} \cdot [(\boldsymbol{u} \cdot \nabla)\boldsymbol{u}] \overset{\boldsymbol{n}=\boldsymbol{e}_z}{=} \int_S dS(u\partial_r w + \frac{v}{r}\partial_\varphi w + w\partial_z w) = 0 \quad . \tag{B.15}$$

Finally the buoyancy term in equation (B.3) is rewritten to

$$\langle \mathrm{Gr}\theta u_i \delta_{i3} \rangle = \langle \mathrm{Gr}\theta w \rangle \quad . \tag{B.16}$$

Collecting all the terms the Reynolds-Orr equation takes its final shape

$$\begin{aligned} \partial_t E_{kin} \quad &+ \underbrace{\langle u^2 \partial_r u_0 \rangle}_{I_{v1}} + \underbrace{\langle uw \partial_z u_0 \rangle}_{I_{v2}} + \underbrace{\left\langle \frac{v^2 u_0}{r} \right\rangle}_{I_{v3}} + \underbrace{\langle uw \partial_r w_0 \rangle}_{I_{v4}} + \underbrace{\langle w^2 \partial_z w_0 \rangle}_{I_{v5}} \\ &- \underbrace{\int_S dS(u\partial_z u)}_{M_r} - \underbrace{\int_S dS(v\partial_z v)}_{M_\varphi} + \underbrace{\langle (\nabla \times \boldsymbol{u})^2 \rangle}_{D} - \underbrace{\langle Gr\theta w \rangle}_{I_{Gr}} = 0 \quad . \end{aligned} \tag{B.17}$$

Here D is the rate of viscous dissipation, I_{v1} to I_{v5} describe the advection of basic state momentum $\boldsymbol{u}_0$ by the perturbation mode $\boldsymbol{u}$, thus adding to the perturbation flow itself. The quantities M_r and M_φ represent the work done by the Marangoni forces on the free surface in radial and azimuthal direction. Contribution of buoyancy are taken into account by I_{Gr}.

B.2 Thermal equivalent of the Reynolds-Orr equation

In order to study the transfer of thermal energy from the basic state $\boldsymbol{x}_0$ to the perturbation mode $\boldsymbol{x}$ and vice versa, we need an equation similar to the Reynolds-Orr equation yet for thermal instead of kinetic energy. Let's look at the temperature equation (2.22b) for a start. Following the lines of sec. B.1 we (a) rewrite equation (2.22b) for an overall flow decomposed into an axisymmetric basic state $\boldsymbol{x}_0$ and a perturbation mode x, (b) substract the temperature equation (2.22b) rewritten solely for the basic state, and (c) linearise with respect to higher order terms in the perturbation. That way we get the equation

$$\partial_t \theta + (\boldsymbol{u}_0 \cdot \nabla)\theta + (\boldsymbol{u} \cdot \nabla)\theta_0 = \frac{1}{Pr}\Delta\theta \quad , \tag{B.18}$$

an equation similar to (B.2). A multiplication by the perturbation temperature θ from the left-hand side, followed by an integration by volume and a reformulation in tensor notation yields

$$\langle \theta \partial_t \theta \rangle + \langle \theta (u_{0,i} \partial_i)\theta \rangle + \langle \theta (u_i \partial_i)\theta_0 \rangle - \langle \frac{\theta}{Pr} \partial_i \partial_i \theta \rangle = 0 \quad . \tag{B.19}$$

Let's study equation (B.19) in detail: the first term

$$\langle \theta \partial_t \theta \rangle = \partial_t E_{th} \quad . \tag{B.20}$$

is time-dependent, dynamic and equivalent to the temporal change of thermal energy of the system. It should vanish, since the system is stationary.

Following the train of thought illustrated for equations (B.5)-(B.8) the first convective term drops out, while the second can be rewritten to

$$\begin{aligned} \langle \theta (u_i \partial_i) \theta_0 \rangle &= \langle \theta \left(u \partial_r + \tfrac{v}{r} \partial_\varphi + w \partial_z \right) \theta_0 \rangle \\ &= \langle \theta u \partial_r \theta_0 + \theta w \partial_z \theta_0 \rangle \quad . \end{aligned} \tag{B.21}$$

Partial integration of the diffusion term yields

$$\frac{1}{Pr} \langle \theta \partial_i \partial_i \theta \rangle = \frac{1}{Pr} \langle \theta e_i \partial_i \theta \rangle_S - \frac{1}{Pr} \langle (\partial_i \theta)(\partial_i \theta) \rangle \quad . \tag{B.22}$$

For cylindrical coordinates and a normal vector $\boldsymbol{n} = \boldsymbol{e}_z$ at the free surface the first term on the right hand side can be reformulated to

$$\frac{1}{Pr} \langle \theta e_i \partial_i \theta \rangle_S = \frac{1}{Pr} \int_S dS \, \theta (\boldsymbol{n} \cdot \nabla) \theta \tag{B.23a}$$

$$\overset{\boldsymbol{n} = \boldsymbol{e}_z}{=} \frac{1}{Pr} \int_S dS \frac{1}{2} \partial_z (\theta^2) \quad . \tag{B.23b}$$

While the second term on the right hand side is obviously equal to

$$\frac{1}{Pr} \langle (\nabla \theta)^2 \rangle \quad . \tag{B.24}$$

Collecting all the terms we get the thermal equivalent of the Reynolds-Orr equation

$$\partial_t E_{th} + \underbrace{\langle \theta u \partial_r \theta_0 \rangle}_{I_{T1}} + \underbrace{\langle \theta w \partial_z \theta_0 \rangle}_{I_{T2}} - \underbrace{\frac{1}{Pr} \int_S dS \frac{1}{2} \partial_z (\theta^2)}_{H} + \underbrace{\frac{1}{Pr} \langle (\nabla \theta)^2 \rangle}_{D_T} = 0 \quad . \tag{B.25}$$

Here D_T is the rate of heat diffusion, I_{T1} and I_{T2} represent the thermal energy produced by the advection of basic state temperature θ_0 by the perturbation flow $\boldsymbol{u}$ thus adding up to the perturbation temperature field θ.

Bibliography

Abderrazak, K., Bannour, S., Mhiri, H., Lepalec, G. & Autric, M. 2008 Numerical and experimental study of molten pool formation during continuous laser welding of AZ91 magnesium alloy. *Comput. Mat. Sci.* .

Albensoeder, S. 2004 *Lineare und nichtlineare Stabilität inkompressibler Strömungen im zweiseitig angetriebenen Rechteckbehälter*. Göttingen: Cuvillier Verlag.

Albensoeder, S., Kuhlmann, H. C. & Rath, H. J. 2001 Three-dimensional centrifugal-flow instabilities in the lid-driven cavity problem. *Phys. Fluids* **13**, 121–135.

Bayly, B. J. 1988 Three-dimensional centrifugal-type instabilities in inviscid two-dimensional flows. *Phys. Fluids* **31**, 56–64.

Ben Hadid, H. & Roux, B. 1990 Thermocapillary convection in long horizontal layers of low-Prandtl-number melts subject to a horizontal temperature gradient. *J. Fluid Mech.* **221**, 77–103.

Boussinesq, J. 1903 *Theorie analytique de la chaleur*, , vol. 2. Paris: Gauthier-Villars.

Bronstein, Semendjajew, Musiol & Mühlig 2001 *Taschenbuch der Mathematik, 5. Aufl.*. Thun und Frankfurt am Main: Verlag Harri Deutsch.

Chen, Q. S. & Hu, W. R. 1997 Numerical investigation on a simulation model of floating zone convection. *Intl J. Heat Mass Transfer* **40**, 757–763.

DebRoy, T. & David, S. A. 1995 Physical processes in fusion welding. *Rev. Mod. Phys.* **67**, 85–112.

Do-Quang, M. 2004 Melt convection in welding and crystal growth. PhD thesis, KTH Stockholm.

Domesi, S. 2005 personal communication.

Drazin, P. G. & Reid, W. H. 1981 *Hydrodynamic Stability*. Cambridge: Cambridge University Press.

Ferziger, J. H. & Perić, M. 2002 *Computational Methods for Fluid Dynamics*. Berlin: Springer.

Golub, H. G. & van Loan, H. G. 1989 *Matrix Computations*. Johns Hopkins University Press.

H. Du, L. Hu, J. Liu & X.Hu 2004 A study on the metal flow in full penetration laser beam welding for titanium alloy. *J. Comput. Mater. Sci.* **29**, 419–427.

Hyer, J. R., Jankowski, D. F. & Neitzel, G. P. 1991 Thermocapillary convection in a model float zone. AIAA *J. Thermophys. Heat Transfer* **5**, 577–582.

J. H. Mathews, K. D. Fink 2004 *NUMERICAL METHODS USING MATLAB*. PEARSON, Prentice Hall.

Kamotani, Y., Lee, J. H. & Ostrach, S. 1992 An experimental study of oscillatory thermocapillary convection in cylindrical containers. *Phys. Fluids* A **4**, 955–962.

Kamotani, Y., Masud, J. & Pline, A. 1996 Oscillatory convection due to combined buoyancy and thermocapillarity. *AIAA J. Thermophys. Heat Transfer* **10**, 102–108.

Kamotani, Y. & Ostrach, S. 1994 Analysis of velocity data taken in surface tension driven convection experiment in microgravity. *Phys. Fluids* **6**, 3601–3609.

Kamotani, Y. & Ostrach, S. 1998 Theoretical analysis of thermocapillary flow in cylindrical columns of high Prandtl number fluids. *ASME J. Heat Transfer* **120**, 758–764.

Kamotani, Y., Ostrach, S. & Masud, J. 1999 Oscillatory thermocapillary flows in open cylindrical containers induced by CO_2 laser heating. *Intl J. Heat Mass Transfer* **42**, 555–564.

Kamotani, Y., Ostrach, S. & Masud, J. 2000 Microgravity experiments and analysis of oscillatory thermocapillary flows in cylindrical containers. *J. Fluid Mech.* **410**, 211–233.

Kuhlmann, H. C. 1996 *Thermokapillare Konvektion in Modellsystemen der Kristallzucht,* Habilitationsschrift. Universität Bremen.

Kuhlmann, H. C. 1999 *Thermocapillary Convection in Models of Crystal Growth*, *Springer Tracts in Modern Physics*, vol. 152. Berlin, Heidelberg: Springer.

Kuhlmann, H. C. 2008 personal communication.

Kuhlmann, H. C. & Rath, H. J. 1993 Hydrodynamic instabilities in cylindrical thermocapillary liquid bridges. *J. Fluid Mech.* **247**, 247–274.

Landau, L. D. & Lifschitz, E. M. 1991 *Hydrodynamik*, *Lehrbuch der Theoretischen Physik*, vol. VI. Akademie Verlag.

Lappa, M. 2005 Review: Thermal convection and related instabilities in models of crystal growth from the melt on earth and in microgravity: Past history and current status. *Cryst. Res. Technol.* **40**, 531–549.

Lappa, M. & Savino, R. 2002 3d analysis of Crystal/Melt interface shape and Marangoni flow instability in solidifying liquid bridges. *J. Comput. Phys.* **180**, 751–774.

Lappa, M., Savino, R. & Monti, R. 2000 Influence of buoyancy forces on Marangoni flow instabilities in liquid bridges. *Int. J. Num. Meth. Heat Fluid Flow* **10**, 721–749.

Lappa, M., Savino, R. & Monti, R. 2001*a* Three-dimensional numerical simulation of Marangoni instabilities in liquid bridges: Influence of geometric aspect ratio. *Int. J. Num. Meth. Fluids* **36**, 53–90.

Lappa, M., Savino, R. & Monti, R. 2001*b* Three-dimensional numerical simulation of Marangoni instabilities in non-cylindrical liquid bridges in microgravity. *Intl J. Heat Mass Transfer* **44**, 1983–2003.

Leypoldt, J. 1999 Dreidimensionale numerische Simulation thermokapillarer Strömungen in zylindrischen flüssigkeitsbrücken. PhD thesis, Universität Bremen.

Li, B. & Kwok, D. Y. 2003 Discrete boltzmann equation for microfluidics. *Phys. Rev. Lett.* **90**, 124502–1–124502–4.

Li, K., Xun, B., Imaishi, N., Yoda, S. & Hu, W. R. 2008*a* Thermocapillary flows in liquid bridges of molten tin with small aspect ratios. *Int. J. Heat Fluid Flow* **29**, 1190–1196.

Li, Y.-R., Imaishi, N., Azami, T. & Hibiya, T. 2004*a* Three-dimensional oscillatory flow in a thin annular pool of silicon melt. *J. Crystal Growth* **260**, 28–42.

Li, Y.-R., Liu, Y.-J., Peng, L. & Wang, Y. 2006 Three-dimensional oscillatory thermocapillary flow in encapsulated liquid bridge. *Phys. Fluids* **18**, 074108–1–074108–6.

Li, Y.-R., Peng, L., Wu, S.-Y., Zeng, D.-L. & Imaishi, N. 2004*b* Thermocapillary convection in a differentially heated annular pool for moderate Prandtl number fluid. *Int. J. Thermal Sci.* **43**, 587–593.

Li, Y.-R., Quan, X.-J., Peng, L., Imaishi, N., Wu, S.-Y. & Zeng, D.-L. 2005 Three-dimensional thermocapillary-buoyancy flow in a shallow molten silicon pool with Cz configuration. *Intl J. Heat Mass Transfer* **48**, 1952–1960.

Li, Y.-R., Xiao, L., Wu, Sh.-Y. & Imaishi, N. 2008*b* Effect of pool rotation on flow pattern transition of silicon melt thermocapillary flow in a slowly rotating shallow annular pool. *Intl J. Heat Mass Transfer* **51**, 1810–1817.

LIMMANEEVICHITR, C. & KOU, S. 2000*a* Experiments to simulate effect Marangoni convection on weld pool shape. *Welding J. (Res. Suppl.)* **79**, 231–237.

LIMMANEEVICHITR, C. & KOU, S. 2000*b* Visualization of Marangoni convection in simulated weld pools containing a surface-active agent. *Welding J. (Res. Suppl.)* **79**, 324–330.

LÜDTGE, R. 1869 Ueber die Ausbreitung von Flüssigkeiten auf einander. *Ann. Phys. Chem.* **137**, 362.

MARANGONI, C. 1871 Ueber die Ausbreitung der Tropfen einer Flüssigkeit auf der Oberfläche einer anderen. *Ann. Phys. Chem.* **143**, 337–354.

MIHALJAN, J. M. 1962 A rigorous exposition of the Boussinesq approximation applicable to a thin layer of fluid. *Astrophys. J.* **136**, 1126–1133.

MILLS, K. C., KEENE, B. J., BROOKS, R. F. & SHIRALI, A. 1998 Marangoni effects in welding. *Phil. Trans. Roy. Soc. London* A **356**, 911–925.

NEITZEL, G. P., CHANG, K.-T., JANKOWSKI, D. F. & MITTELMANN, H. D. 1993 Linear-stability theory of thermocapillary convection in a model of the float-zone crystal-growth process. *Phys. Fluids* A **5**, 108–114.

NEUMANN, G. 1990 Three-dimensional numerical simulation of buoyancy driven convection in vertical cylinders heated from below. *J. Fluid Mech.* **214**, 559.

NIENHÜSER, C. 2002 Lineare stabilität achsensymmetrischer thermokapillarer konvektion in flüssigkeitsbrücken mit statisch und dynamisch deformierbarer grenzfläche. PhD thesis, Universität Bremen.

NIENHÜSER, C. & KUHLMANN, H. C. 2002 Stability of thermocapillary flows in non-cylindrical liquid bridges. *J. Fluid Mech.* **458**, 35–73.

OBERBECK, A. 1879 Ueber die wärmeleitung der flüssigkeiten bei berücksichtigung der strömungen infolge von temperaturdifferenzen. *Ann. Phys. Chem.* **7**, 271–292.

OBERMEIER-GMBH 2007 Kurt obermeier gmbh & co. kg. deutschland. personal communication. .

PATANKAR, S. V. 1980 *Numerical Heat Transfer and Fluid Flow*. Hemisphere.

PEARSON, J. R. A. 1958 On convection cells induced by surface tension. *J. Fluid Mech.* **4**, 489–500.

PLINE, A., ZURAWSKI, R., JACOBSON, T., KAMOTANI, Y. & OSTRACH, S. 1996 Hardware and performance summary of the Surface Tension Driven Convection Experiment-2 aboard the USML-2 Spacelab Mission. In *47th International Astronautical Congress*. Beijing, China, iAF-96 – J.5.01.

Pshenichnikov, A. F. & Yatsenko, S. S. 1974 Convective diffusion from localized source of surfactant. *Hydrodynamics* **5**, 175–181, (in Russian).

R. J. LeVeque, D. Mihalas, E. A. Dorfi & Müller, E. 1998 *Computational Methods for Astrophysical Fluid Flow*, *Saas-Fee Advanced Course*, vol. 27. Berlin Heidelberg: Springer.

Rybicki, A. & Floryan, J. M. 1987 Thermocapillary effects in liquid bridges. I. Thermocapillary convection. *Phys. Fluids* **30**, 1956–1972.

Schoisswohl, U. & Kuhlmann, H. 2006 Flow instabilities in thermocapillary liquid pools. *Proc. Appl. Math. Mech.* **6**, 589–590.

Schoisswohl, U. & Kuhlmann, H. C. 2007 Instabilities and pattern formation in thermocapillary liquid pools. *Fluid Dyn. Mat. Proc.* **3**, 317–327.

Schwabe, D. 2002 Buoyant-thermocapillary and pure thermocapillary convective instabilities in czochralski systems. *J. Crystal Growth* **237–239**, 1849–1853.

Scriven, L. E. & Sternling, C. V. 1960 The Marangoni effects. *Nature* **187**, 186–188.

Shi, W. & Imaishi, N. 2006 Hydrothermal waves in differentially heated shallow annular pools of silicone oil. *J. Crystal Growth* **290**, 280–291.

Shiratori, S. 2007 Stability of thermocapillary flow in liquid bridges of low-prandtl-number fluids. PhD thesis, Tokyo Metropolitan Institute of Technology.

Shtern, V. & Hussain, F. 1993 Azimuthal instability of divergent flows. *J. Fluid Mech.* **256**, 535–560.

Shtern, V. & Hussain, F. 1999 Collapse, symmetry breaking, and hysteresis in swirling flows. *Annu. Rev. Fluid Mech.* **31**, 537–566.

Sim, B.-Ch. & Zebib, A. 2002 Effect of free surface heat loss and rotation on transition to oscillatory thermocapillary convection. *Phys. Fluids* **14**, 225–231.

Sim, B.-Ch. & Zebib, A. 2004 Thermocapillary convection in cylindrical liquid bridges and annuli. *Comptes Rendus Mecanique* **332**, 473–486.

Sipp, D. & Jacquin, L. 2000 Three-dimensional centrifugal-type instabilities of two-dimensional flows in rotating systems. *Phys. Fluids* **12**, 1740–1748.

Smith, M. K. 1986 Instability mechanisms in dynamic thermocapillary liquid layers. *Phys. Fluids* **29**, 3182–3186.

Smith, M. K. & Davis, S. H. 1983 Instabilities of dynamic thermocapillary liquid layers. Part 1. Convective instabilities. *J. Fluid Mech.* **132**, 119–144.

Tang, Z. M. & Hu, W. R. 1992 Numerical simulation of thermocapillary oscillatory convection in liquid bridge of half floating zone. *Microgravity Q.* **2**, 123.

Thomson, J. 1855 On certain curious motions observable at the surfaces of wine and other alcoholic liquors. *London, Edinburgh, and Dublin Phil. Mag. J. Sci.* **10**, 330–333.

Tipler, Paul A. 1994 *Physik*. Spektrum Akademischer Verlag GmbH. Heidelberg, Berlin.

Versteeg, H. K. & Malalasekera, W. 1995 *Computational Fluid Dynamics - The Finite Volume Method*. England, UK: PEARSON Prentice Hall.

Wacker-Silikonöle-AK 2001 Produktbeschreibung. wacker chemie gmbh, münchen, deutschland .

Wagner, C., Friedrich, R. & Narayanan, R. 1994 Comments on the numerical investigation of Rayleigh and Marangoni convection in a vertical circular cylinder. *Phys. Fluids* **6**, 1425–1433.

Wanschura, M. 1996 Lineare instabilitäten kapillarer und natürlicher konvektion in zylindrischen flüssigkeitsbrücken. PhD thesis, ZARM – Universität Bremen.

Wanschura, M., Kuhlmann, H. C. & Rath, H. J. 1996 Three-dimensional instability of axisymmetric buoyant convection in cylinders heated from below. *J. Fluid Mech.* **326**, 399–415.

Wanschura, M., Kuhlmann, H. C., Shevtsova, V. S. & Rath, H. J. 1995*a* Thermo- and solutocapillary convection in a cylindrical liquid bridge: Stability of axisymmetric flow. *Adv. Space Res.* **16** (7), 75–78.

Wanschura, M., Shevtsova, V. S., Kuhlmann, H. C. & Rath, H. J. 1995*b* Convective instability mechanisms in thermocapillary liquid bridges. *Phys. Fluids* **7**, 912–925.

Widnall, S. E. & Tsai, Ch.-Y. 1977 The instability of the thin vortex ring of constant vorticity. *Proc. Roy. Soc. London* **287**, 273–305.

Xu, J.-J. & Davis, S. H. 1984 Convective thermocapillary instabilities in liquid bridges. *Phys. Fluids* **27**, 1102.

List of Publications

Papers in Refereed Journals

1. U. Schoisswohl and H. C. Kuhlmann, Instabilities and pattern formation in thermocapillary liquid pools, Fluid Dynamics and Materials Processing **3**, 317–328 (2006).
2. U. Schoisswohl and H. C. Kuhlmann, Instabilities and pattern formation in thermocapillary buoyant liquid pools of varying aspect ratio, (in preparation).
3. U. Schoisswohl and H. C. Kuhlmann, Instabilities and pattern formation in annular thermocapillary buoyant liquid pools. - A numerical study of Kamotani's Surface Tension Driven Convection Experiment (STDCE), (in preparation).

Refereed Conference Proceedings in Journals

1. U. Schoisswohl, H. Kuhlmann, Flow instabilities in thermocapillary liquid pools Proceedings of Applied Mathematics and Mechanics **6**, 589–590 (2006).
2. U. Schoisswohl and H. C. Kuhlmann, Instability mechanisms in buoyant-thermocapillary liquid pools. Proceedings of Applied Mathematics and Mechanics (2007), accepted for publication.

Non-Refereed Conference Contributions

1. U. Schoisswohl and H. C. Kuhlmann, Instabilities and pattern formation in thermocapillary liquid pools, Bulletin of the American Physical Society **51** (9), 120 (2006).
2. U. Schoisswohl and H. C. Kuhlmann, Instabilities and pattern formation in thermocapillary liquid pools, Proceedings of the 3rd International Conference of the International Marangoni Association (2006).

Curriculum Vitae

Persönliche Daten

Name	Ulrich Schoisswohl
Geburtsdatum	Nov. 14, 1979
Geburtsort	Wels (Österreich)
Nationalität	Österreicher
Familienstand	ledig
Adresse	Bennogasse 30/2/3, A-1080 Wien, Austria

phone (office): +43 (0)1 58801 32247
phone (home): +43 (0)699 18237009
e-mail: ulrich.schoisswohl@tuwien.ac.at

Ausbildung

seit 10/04	**Doktoratsstudium der technischen Wissenschaften** am Institut für Strömungsmechanik und Wärmeübertragung, Technischen Universität Wien (Austria)
07/04	**Mag.rer.nat.**, Diplomarbeit in Astrophysik und Computational Physics an der ehemaligen Fakultät für Natur- und Formalwissenschaften der Universität Wien (Austria)
10/01–07/04	**Studium der Physik** an der Universität Wien
10/99–07/04	**Studium der Astronomie und Astrophysik** an der Universität Wien
09/90–06/98	BG and BRG Brucknerstrasse in Wels (Austria)
09/86–06/90	Volksschule VS8 in Wels (Austria)

Ausseruniversitäre Ausbildungen

01/06–06/07	Ausbildung zum **eingetragenen Mediator** bei komarek konfliktmediation Wien, (Austria)

Zivildienst

10/98–09/99	Rotes Kreuz in Wels (Austria)